Fall 12-20-2017

Design, Manufacture, and Structural Dynamic Analysis of a Biomimetic Insect-Sized Wing for Micro Air Vehicles

Jose Enrique Rubio
University of New Orleans, jerubio@uno.edu

Design, Manufacture, and Structural Dynamic Analysis of a Biomimetic Insect-Sized Wing for Micro Air Vehicles

A Dissertation

Submitted to the Graduate Faculty of the
University of New Orleans
in partial fulfillment of the
requirements for the degree of

Doctor of Philosophy
in
Engineering and Applied Sciences
Mechanical Engineering

by

José Enrique Rubio Reyes

B.Sc. University of New Orleans, 2012
M.Sc. University of New Orleans, 2014

December, 2017

Dedicated to my parents for their love, support, and encouragement

ACKNOWLEDGMENTS

I wish to extend my appreciation to my major professor Dr. Uttam Chakravarty for giving me the opportunity to be part of his research team. Without the motivation and mentorship of Dr. Chakravarty finishing this study would not have been possible. I am also thankful to Dr. Paul Schilling for his continuous advice from my undergraduate career until the completion of this dissertation. The guidance and recommendations from Dr. Schilling have been fundamental for my personal, academic, and professional development throughout these years at the University of New Orleans. I would also like to express my sincere thanks to Dr. Juliette Ioup, Dr. Leszek Malkiski, and Dr. Martin Guillot and for serving as committee members for my dissertation. Their insightful counsel was essential to improve the quality of this manuscript.

I would like to extend my gratitude to my colleagues Manohar Chidurala, Pratik Sarker, M. Shafiqur Rahman, Amer Hussain, M. Khairul Pulok, and Mine Kaya for their support and for sustaining valuable discussions regarding the content of this manuscript. Also, I extensively value the help provided by Rahtmatollah Eskandari for the conduction of the photolithography process and by William Miller for his assistance on the scanning of the specimen.

Seda Aslan—there are no words to thank you for always listening, encouraging, and supporting me.

I feel indebted to my family for their endless support and encouragement throughout the journey that started when I left home to pursue my undergraduate degree. Thanks for always being there for me and for believing in me.

I would like to acknowledge the Louisiana Board of Regents for providing the funding for this investigation under the contract number LEQSF (2013-16)-RD-A-17.

TABLE OF CONTENTS

NOMENCLATURE

Abbreviations

2-D	–	two-dimensional
3-D	–	three-dimensional
CAD	–	computer-aided design
CFD	–	computational fluid dynamics
DIC	–	digital image correlation
DFT	–	discrete Fourier transform
FFT	–	fast Fourier transform
FRF	–	frequency response function
FE	–	finite element
FSI	–	fluid-structure interaction
MAV	–	micro air vehicle
MEMS	–	microelectromechanical systems
Micro-CT	–	micro-computed tomography
UV	–	ultraviolet light

Nomenclature

A	–	surface area
C_D	–	coefficient of drag
C_L	–	coefficient of lift
c	–	chord length

D – total derivative

E – modulus of elasticity

F_D – drag force

F_L – lift force

$F(s)$ – Fourier transform of the continuous function *f(x)*

f – frequency

g – gravity or buoyancy force

$H(s)$ – frequency response function or transfer function

h – thickness of shell

I – area moment of inertia

L – characteristic length of the immersed body

l – length of flat plate

N – number of discrete data

n – normal direction to a referenced surface

P – pressure

q – distributed load

R – resultant aerodynamic force

Re – Reynolds number

S_V – von Mises stress

S – reference area of the immersed body

t – time

U – deformation magnitude

U_x – deformation component in *x*-direction

U_y – deformation component in *y*-direction

U_z – deformation component in *z*-direction

V – velocity

V_∞ – freestream velocity

$\vec{V}$ – velocity vector

v_x – velocity component in *x*-direction

v_y – velocity component in *y*-direction

v_z – velocity component in *z*-direction

w – out of plane or transverse deflection

$X(k)$ – discrete Fourier transform of the discrete function *x(n)*

x – Cartesian coordinate

y – Cartesian coordinate

z – Cartesian coordinate

Greek symbols

α – angle of attack

δ – boundary layer thickness

η – Blasius non-dimensional variable

θ – angle relative to the surface of immersed body

λ_{ij} – Kronecker's delta function

μ – dynamic or absolute viscosity

ν – kinematic viscosity

ρ – density

τ – shear stress

τ_{ij} – stress tensor

υ – Poisson's ratio

ω – frequency of oscillation

Symbols

$\vec{\nabla}$ – gradient vector

$\vec{\nabla}^4$ – biharmonic operator

∂ – partial derivative or differential element

LIST OF FIGURES

LIST OF TABLES

ABSTRACT

The exceptional flying characteristics of airborne insects motivates the design of biomimetic wing structures that can exhibit a similar structural dynamic behavior. For this purpose, this investigation describes a method for both manufacturing a biomimetic insect-sized wing using the photolithography technique and analyzing its structural dynamic response. The geometry of a crane fly forewing (family *Tipulidae*) is acquired using a micro-computed tomography scanner. A computer-aided design model is generated from the measurements of the reconstructed scanned model of the insect wing to design the photomasks of the membrane and the venation network required for the photolithography procedure. A composite material wing is manufactured by patterning the venation network using photoresist SU-8 on a Kapton film for the assembling of the wing. A single material artificial wing is fabricated using the photoresist SU-8 for both the membrane and the network of veins. Experiments are conducted using a modal shaker and a digital image correlation (DIC) system to determine the natural frequencies and the mode shapes of the artificial wing from the fast Fourier transform of the displacement response of the wing. The experimental results are compared with those from a finite element (FE) model of the wing. A numerical simulation of the fluid-structure interaction is conducted by coupling the FE model of the artificial wing with a computational fluid dynamics model of the surrounding airflow. From these simulations, the deformation response and the coefficients of drag and lift of the artificial wing are predicted for different freestream velocities and angles of attack. Wind-tunnel experiments are conducted using the DIC system to determine the structural deformation response of the artificial wing under different freestream velocities and angles of attack. The vibration modes are dominated by a bending and torsional deformation response. The deformation along the span of the wing increases nonlinearly from the root of the wing to the tip

of the wing with Reynolds number. The aerodynamic performance, defined as the ratio of the coefficient of lift to the coefficient of drag, of the artificial wing increases with Reynolds number and angle of attack up to the critical angle of attack.

Keywords: Biomimetic artificial insect-sized wing, vibrations, aerodynamics, MAVs, photolithography

CHAPTER 1 INTRODUCTION

The research on the field of aerodynamics has always been concerned on optimizing the structural dynamic response of airborne engineering systems. It is of special interest to implement design strategies that could maximize the aerodynamic efficiency of aerial vehicles, meaning increasing the lift production while minimizing the drag; and that could offer adequate bending and torsional resistance to aerodynamic and inertial loadings. Through flying insects, nature provides exceptional examples of biomechanical aerial assemblies with an outstanding structural dynamic performance. These organisms have developed incomparable flight skills thanks to the compliant reaction of their wings to the moving fluid. Researchers have turned their attention to this behavior and efforts are currently allocated to the design of biologically inspired insect-sized wing structures capable of successfully emulating the structural dynamic response of their nature analogs for their possible implementation into the new generation of biologically inspired micro air vehicles (MAVs). Detailed descriptions and analysis of the modal and the aerodynamics characteristics of both the insect and the artificial wings are required for biomimicking optimal flight and maneuver conditions similar to those encounter during insect flight.

1.1 Motivation and Objectives of the Study

MAVs are miniature-scaled autonomous aircrafts used for military and civilian operations at hazardous or inaccessible environments where human presence is to be avoided. Examples of the tasks performed by MAVs include field reconnaissance, surveillance, and weather conditions monitoring. The success in performing these duties is strongly dependent on a reliable maneuverability coupled to an exceptional structural dynamic performance. The need

for MAVs that meet the aforesaid characteristics has motivated the study and development of different design approaches for these aircrafts, one of them being the biologically inspired method which attempts to biomimic the excellent maneuver skills during low-speed flight and hovering mastered by insects. These nature-inspired MAVs offer several advantages with respect to their multirotor or fixed wing analogs, such as higher lift-to-drag ratios, lower power consumption, and smaller size systems.

The optimized design of a flexible wing structure is a critical element of a biologically inspired MAV. The research on the field of aerodynamics of insect flight advocates that the unique aerodynamic skills of aerial insects is strongly dependent on the presence of relatively flexible wings. The motivation of this study is the development of an artificial biologically inspired insect-sized wing capable of biomimicking the pliant structural dynamic behavior of its nature analog for the consequent implementation into a nature inspired insect-sized MAV. For this purpose, this investigation details at first a method for characterizing and analyzing the morphology and the structural behavior of a crane fly forewing to determine key design aspects that must be transferred to the artificial wing structure. A procedure is then detailed for manufacturing an artificial insect-sized wing of similar morphology and for investigating its structural dynamic response in terms of the modal characteristics, the time-varying deformation due to aerodynamic loading, and the aerodynamic coefficients. The outcomes of this investigation can be evaluated from the following objectives and sub-objectives.

1.1.1 Overall Objective

1) To develop a method for designing and analyzing a biologically inspired insect-sized wing for their suitable implementation as a wing structure of a MAV.

1.1.2 Sub-Objectives

1) To characterize the internal and the external morphologies of an insect wing.
2) To develop a computer-aided design (CAD) model of the insect wing.
3) To manufacture a biologically inspired insect-sized wing that mimics the morphology, mechanical properties, and structural dynamic performance from its nature counterpart.
4) To estimate the modal characteristics of the artificial biologically inspired insect-sized wing using a vibrational experimental setup.
5) To determine the structural dynamic response of the artificial biologically inspired insect-sized wing in a low-speed wind tunnel with airflow conditions that are representative of the flight regime of MAVs.
6) To develop a finite element (FE) model of the artificial wing to determine its modal characteristics.
7) To develop a structure-aerodynamic interaction model to investigate the structural dynamic response of the artificial biologically inspired insect-sized wing under different airflow conditions that are representative of the flight regime of MAVs.
8) To develop a FE model of the insect wing to determine its modal characteristics.
9) To develop a structure-aerodynamic interaction model to investigate the structural dynamic response of the insect wing under different airflow conditions that are representative of the flight regime of such insect.
10) To validate the structure-aerodynamic interaction models of the artificial biologically inspired insect-sized wing with the data acquired from the vibration and wind-tunnel experiments.

1.2 Background Theory

1.2.1 Aerodynamic Forces on an Object Immersed in a Fluid

The identification of general aerodynamic terminology associated to any object immersed in a fluid is required before proceeding with further discussion. The geometry of a body of any size and shape—namely a cylinder, a flat plate, or an insect wing for instance—immersed on a fluid consists of the leading or foremost edge which interacts with the flow streamlines at first and the trailing or rear edge where the flow streamlines leave the surface of the body. The chord length c is defined as the linear distance between the trailing edge and the leading edge. The freestream velocity V_∞ is defined as the flow velocity far ahead of the body. The angle of attack α is defined as the angle between the chord and the freestream velocity. These aerodynamic terms are exemplified in Fig. 1.1.

Moments and forces are generated at the fluid-body interface when a fluid moves over an immersed body. The generation of these forces and moments is directly related to the pressure and shear stress distributions along the surface area of the immersed body [1]. The pressure or normal stress acts normal to the surface of the body; whereas the shear stress acts tangential to the surface. The net effect of the pressure and shear distributions integrated over the complete body surface is a resultant aerodynamic force R and a moment M on the body, both of them are represented in Fig. 1.1.

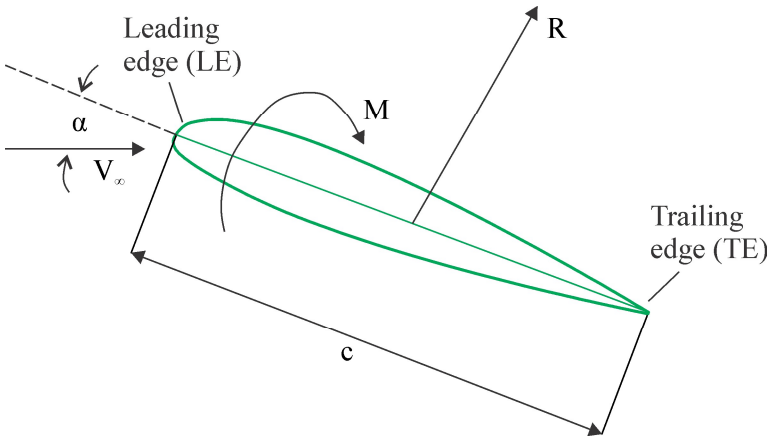

Figure 1.1 Aerodynamic definitions. *Resultant aerodynamic force and moment exerted on a body immersed on a fluid [1].*

The resultant aerodynamic force *R* can be split into an infinite number of components depending on which reference frame is employed. Commonly used reference frames are the freestream velocity and the chord length.

When the freestream velocity is used as the reference frame, the resultant aerodynamic force R can be divided into the lift force F_L and the drag force F_D as shown in Fig. 1.2. The lift force F_L is defined as the component of the resultant aerodynamic force *R* perpendicular to the freestream velocity. The drag force F_D is the component of the resultant aerodynamic force *R* parallel to the freestream velocity.

When the chord length is used as the reference frame, the resultant aerodynamic force *R* can be divided into the normal force F_N and the axial force F_A components as shown in Fig. 1.2. The normal force F_N is the component of the resultant aerodynamic force *R* perpendicular to the chord. The axial force F_A is the component of the resultant aerodynamic force *R* parallel to the chord.

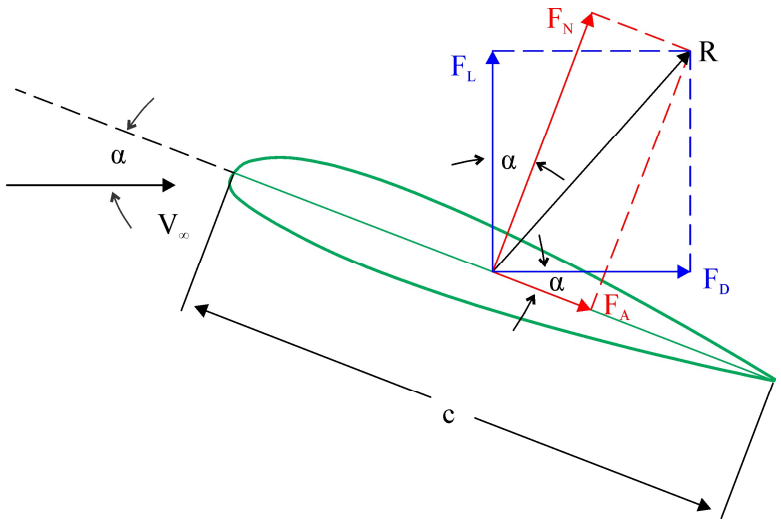

Figure 1.2 Aerodynamic force components. *Description of the drag, lift, axial, and normal force components exerted on a body immersed on a fluid [1].*

The generation of drag and lift determines the aerodynamic efficiency of a particular body; therefore, they are discussed in detail in the following paragraphs. The mathematical formulation to determine the drag and the lift forces exerted on a surface must take into account the pressure P and shear stress τ distributions. A basic trigonometric analysis on Fig 1.2 yields the relation for the drag force and the lift force in terms of the axial and normal force components. These mathematical relations are presented in Eqs. 1.1. and 1.2 [1].

$$F_D = F_N \sin\alpha + F_A \cos\alpha \tag{1.1}$$

$$F_L = F_N \cos\alpha - F_A \sin\alpha \tag{1.2}$$

The integrations of the pressure P (stress component normal to the surface and oriented at an angle θ relative to the perpendicular) and the shear stress τ (stress component tangential to the surface and oriented at the same angle θ relative to the horizontal) distributions over the surfaces of a differential element *ds*, shown in Fig. 1.3, are required to determine an expression for the normal and the axial forces. The details of these integrations and the respective derivations are

presented in [1]. The final equations for calculating the total axial force F'_A and the total normal force F'_N per unit span are shown in Eqs. 1.3 and 1.4, respectively [1].

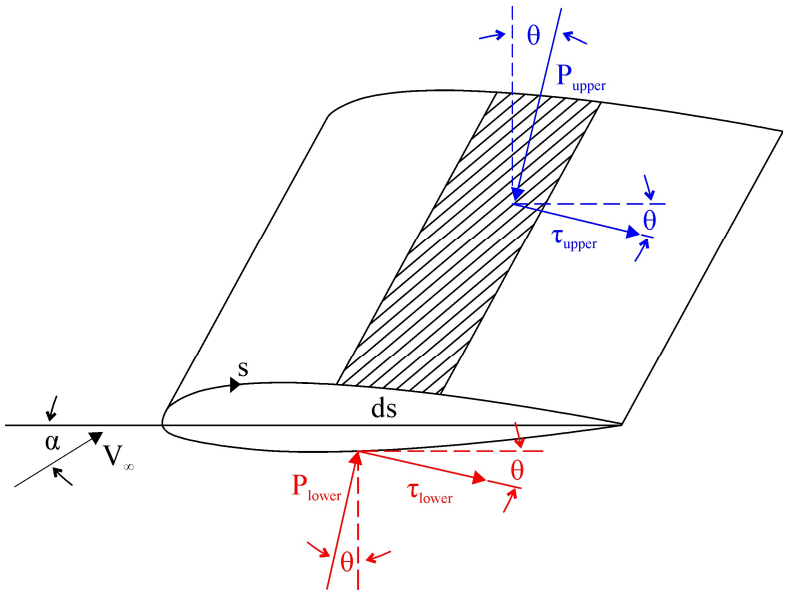

Figure 1.3 Force analysis acting on a differential element. *Nomenclature for the integration of the pressure p and the shear stress τ distributions over the surfaces of a differential element ds [1].*

$$F'_A = \int_{LE}^{TE} \left(-P_{upper} \sin\theta + \tau_{upper} \cos\theta\right) ds_{upper} + \int_{LE}^{TE} \left(P_{lower} \sin\theta + \tau_{lower} \cos\theta\right) ds_{lower} \tag{1.3}$$

$$F'_N = -\int_{LE}^{TE} \left(P_{upper} \cos\theta + \tau_{upper} \sin\theta\right) ds_{upper} + \int_{LE}^{TE} \left(P_{lower} \cos\theta - \tau_{lower} \sin\theta\right) ds_{lower} \tag{1.4}$$

Substituting Eqs. 1.3 and 1.4 into Eqs. 1.1 and 1.2 allows the calculation of the respective total drag and total lift forces per unit span of the object. Alternatively, the drag and lift forces can be defined in terms of dimensionless parameters called the coefficient of drag C_D and the coefficient of lift C_L which are defined in general terms in Eqs. 1.5 and 1.6, respectively [1].

$$C_D = \frac{F_D}{2\rho_\infty V_\infty^2 S} \tag{1.5}$$

$$C_L = \frac{F_L}{2\rho_\infty V_\infty^2 S} \tag{1.6}$$

where F_D is the drag force, F_L is the lift force, ρ_∞ represents the density of the fluid, V_∞ is the freestream velocity, and S is the reference area of the body.

1.2.2 Viscous and Inviscid Flow Concepts: Drag and Lift Generation

For most problems in aerodynamics, the shear stress has a meaningful effect on the flow region where the velocity gradients are substantial. For the vast region of the flow field away from the body, the velocity gradients are relatively small and friction plays virtually no role; therefore, the flow is considered to be inviscid. However, for the thin region of the flow adjacent to the surface, the velocity gradients are large and friction due to the viscosity plays a defining role. This thin viscous region adjacent to the surface of the body is called the boundary layer and it increases in the direction of the flow [1]. The boundary layer is extremely important in aerodynamics as far as to determine how much influence it has in the generation of the aerodynamic forces.

At this point, it is convenient to introduce the definition of the Reynolds number—a dimensionless quantity that represents the ratio of the inertial forces to the viscous forces. The Reynolds number governs the nature of viscous flows. Mathematically, the Reynolds number *Re* is defined in Eq. 1.7,

$$\mathrm{Re} = \frac{\rho_\infty V_\infty L}{\mu} \tag{1.7}$$

where ρ_∞ represents the density of the fluid, V_∞ is the freestream velocity, L is the characteristic length of the body, and μ is the absolute viscosity of the fluid.

Recalling Figs. 1.2 and 1.3, the pressure force P acts normal to the surface, which in general for the aerodynamic bodies is the same as the vertical direction, that is, the lift direction. Contrarily, the shear stress τ acts tangential to the surface, which is mainly the horizontal or drag direction. Therefore, it can be concluded that the generation of lift is mainly influenced by the pressure and it can be estimated from inviscid flow theory. On the other hand, the generation of drag can have two sources. At low Reynolds numbers, the viscous effects are predominant with significant amount of skin-friction drag; while at large Reynolds number, the inertial forces have more influence and pressure drag effects due to flow separation may exist.

1.2.3 Insect Flight Aerodynamics

The characterization of the aerodynamics of insect flight has been a challenging task. The small scale of insects and the high frequency flapping motion of their wings make experimental analysis difficult. Nevertheless, the development of different computational tools such as the computational fluid dynamics (CFD), together with the progression of advanced experimental setups such as high-speed cameras, digital image correlation software, and particle image velocimetry systems have made possible the analysis of the structural behavior of insect wings under aerodynamic loading and the flow characterization related to insect flight.

The geometry of a typical insect wing consists of the leading edge and the trailing or rear edge. Correlated to airfoil terminology, the wing span of an insect wing is referred as the linear distance from the tip of the wing to the root of the wing where it intersects with the thorax of the insect; the wing span is also known as the longitudinal axis of the wing. On the other hand, the chord length is defined as the linear distance between the trailing edge and the corresponding point in the leading edge. These terms are all presented in Fig. 1.4.

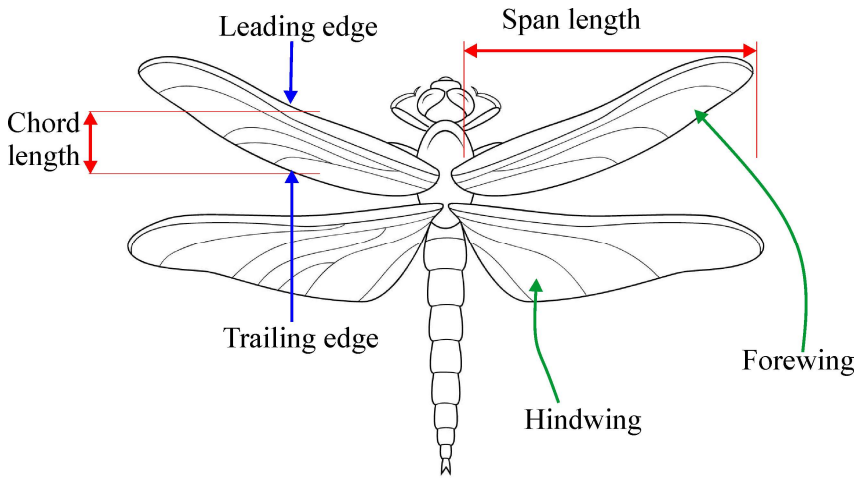

Figure 1.4 Insect wing terminology. *Identification of the main parts of an insect wing related to aerodynamics.*

The aerodynamic flapping cycle of insects entails more than the simple translation of the insect wing. The flapping cycle of an insect, shown in Fig. 1.5, consists of the downstroke and the upstroke, which refer to the translation of the insect wing over the air to a lower or higher angle of attack, respectively. The flapping cycle also consists of two transitional stages that involve the rotation about the longitudinal axis of the wing. These stages are known as the pronation and the supination. Wing pronation takes place during the transition from upstroke to downstroke and it consists in the inward rolling of the wing towards the thorax of the insect so that the leading edge faces downwards. Contrarily, wing supination occurs during the transition from downstroke to upstroke and it involves the outward rolling of the wing towards the torso of the insect so that the leading edge faces upwards [2, 3].

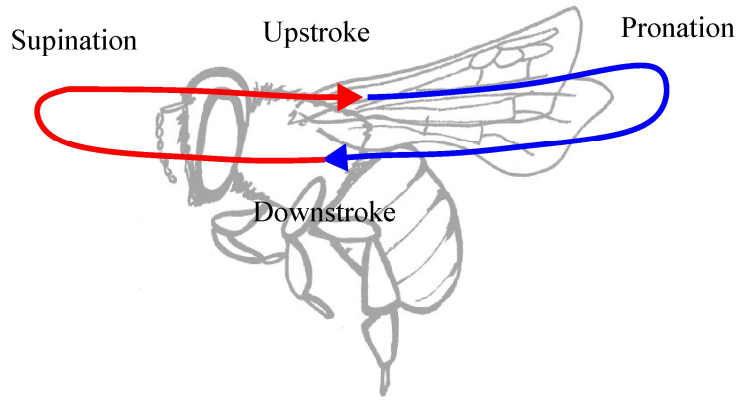

Figure 1.5 Flapping cycle of insects. *Description of the different stages of the flapping cycle for flying insects [2].*

Flying insects generate the necessary lift and thrust by passively experiencing elastic deformations in their compliant wings coupled to unsteady aerodynamic mechanisms derived from the structural response of the insect wing to aerodynamic and inertial loadings. These passive deformations may include twisting of the wings to change the angle of attack during the stroke cycle and altering the camber from the leading edge of the wing to the tip of the wing [2]. Different unsteady mechanisms that improve the aerodynamic performance of insects have been identified. The first mechanism is the clap and fling. At the end of the upstroke, the leading edge of each wing touches each other or "clap" before the trailing edge makes contact, progressively closing the gap between them and creating a shape similar to a vertical plate. As the wing presses together closely, the opposing circulations of the fluid from each of the wings are cancelled out each other. Following, at the beginning of the downstroke, the wings are quickly pronated with the leading edge "flinging" apart, creating a low-pressure region between them that causes the gap to be filled with entering air, consequently providing an initial momentum and a vortex of air [2–4]. Collectively, the clap and fling results in a modest, but significant, lift enhancement.

The second well-known unsteady aerodynamic mechanism in insect flight is the delayed stall. As the wing increases its angle of attack, the fluid stream going over the wing separates as it crosses the leading edge of the wing but reattaches before it reaches the trailing edge of the wing. In such case, the leading edge vortex occupies the separation zone above the wing and a greater downward momentum is imparted to the fluid, therefore, increasing the lift magnitude [2–4]. As the wing translates at a higher angle of attack, the leading edge vortex grows in size until flow reattachment is no longer possible and the lift dramatically decreases. This phenomenon is known as stall. The possibility of flow reattachment provided by the compliant deformation of the insect wing allows the delay of the stall condition.

The third unsteady aerodynamic mechanism is known as the wake capture and rotational circulation. This mechanism has a coupled effect in which the insect wing takes advantage of the wake created by the previous stroke. The wake allows an upward lift to be generated when the wing's own rotation creates air circulation at the end of the stroke [2]. The wake capture and rotational circulation mechanism starts as the wing reverses stroke and it sheds a vortex at both the leading and trailing edges. These shed vortices induce a strong velocity field. As the wing reverse direction, it encounters the enhanced velocity field which increases the magnitude of the aerodynamic forces immediately following the stroke reversal [2, 3].

1.2.4 Vibrations: Natural Frequency, Mode Shapes, and Resonance

Vibration, also commonly referred as oscillation, is a motion that repeats itself after an interval of time [5]. Vibrational loads are inherent to aerial insects and biologically inspired MAVs due to their flapping flying cycle. These repetitive loads cause fatigue that can eventually lead to failure or degrade the performance of the structure. For this reason, a characterization of the modal response of the wing structure is fundamental for the design of a reliable aerodynamic

assembly. In general, the modal characterization involves the calculation of the natural frequencies and the identification of the respective mode shapes of a particular structure.

The concept of frequency of vibration of any mechanical system or structure is one of the most important concepts in vibration analysis. If a system, after an initial disturbance, is left to vibrate on its own, the frequency or number of cycles per unit time at which it oscillates without external forces is known as the natural frequency [5]. The mode shape is a mathematical description of the deflection of the oscillations. It forms a pattern that describes the shape of vibration if the system is left to vibrate only at the corresponding natural frequency [6]. Identifying the natural frequency of a system is of importance to avoid failure due to resonance. Whenever the natural frequency of vibration of a structure matches with the frequency of external excitation, the amplitude of the oscillations increases substantially; this phenomenon is known as the resonance and may lead to significant structural damage or failure due to excessive deflections.

For the purpose of the modal analysis of this investigation, the artificial wing must be considered as a multiple-degree-of-freedom system where its mass and its stiffness is distributed throughout its structure as a series of infinitely small elements. Hence, the wing is called a distributed-parameter system in which each of these infinite number of elements will move relative to each other in a continuous fashion when vibrating. Given the infinite degrees of freedom, the artificial wing will have an infinite number of natural frequencies [6]. The concept of resonance in an infinite degree-of-freedom system is based on the idea that a harmonic driving force excites the system at its natural frequency and causes an unbounded oscillation in the undamped case and a response with a maximum amplitude in the damped case [6]. The objective of the modal characterization is to identify areas of the wing structure that may need

reinforcement from repetitive loads and to determine the resonance frequencies which may lead to oscillations of large amplitude. In general, for any structure, the first three natural frequencies dominate the vibration response—meaning their estimation and analysis is fundamental and necessary for the design of the structure.

1.2.5 Micro Air Vehicles

MAVs are autonomous, lightweight, small-scale flying devices with a maximum wing span of 15 cm and a maximum flying speed of approximately 15 m/s as detailed in Table 1.1. An interest in the design of these aerial devices has immensely grown over the last years due to their potential to operate in remote or otherwise hazardous locations where they may perform a variety of tasks, including but not limited to, reconnaissance, surveillance, and safety inspection. To accomplish these tasks, the wings of MAVs should be aerodynamically efficient, optimized structures; such as the wings found in different insects. The design of biologically inspired insect-sized wings aims to mimic the superlative maneuverability characteristics during low-speed flight mastered by insects for their implementation into the new generation of nature inspired MAVs.

Table 1.1 MAVs design requirements as outlined by the Defense Advanced Research Projects Agency (DARPA) [7, 8]

Specifications	Requirements	Details
Size	<15.24 cm	Maximum dimension
Weight	~100 g	Objective gross takeoff weight (GTOW)
Range	1 to 10 km	Operational range
Endurance	60 min	Loiter time on station
Altitude	<150 m	Operational ceiling
Speed	15 m/s	Maximum flight speed
Payload	20 g	Mission dependent
Cost	$1500	Maximum cost, 2009 USD

1.3 Literature Survey

1.3.1 Insect Wing Aerodynamics and Structural Behavior

The insect wings experience highly elastic deformations during flapping flight to be able to generate more upward than downward force. The compliant wing deformation achieves this purpose in different ways. For instance, the insect wing may twist to change the angle of attack throughout the stroke and create an asymmetric force generation; similarly, the camber of the wing may be altered to increase or decrease the area of the wing exposed to the aerodynamic forces [9]. Further evidence supported that the development of aerodynamic unsteady mechanisms coupled to the elastic distortion of the wing allowed insects to proficiently hover and maneuver in different airflow conditions [2, 10]. Miller and Peskin [4, 11] analyzed in detail the clap and fling mechanism and concluded that its lift-enhancing effects were greater for low Reynolds numbers. It was further confirmed that large lift forces were not only generated during the rotation of the wing but they were also transiently enhanced during the translation of the wing following the fling. Their results highlighted that the flexibility of the wing reduced the large drag forces generated during the clap and fling while maintaining lift for a certain range of wing flexibilities. Santhanakrishnan et al. [12] assessed the role of bristled wing structures to reduce the drag required to clap together and fling apart wings at lower Reynolds number. Their study showed that the porous nature of the wing contributed largely to the reduction of drag. The existence of the leading edge vortex related to the delayed stall aerodynamic mechanism and its contribution to the production of aerodynamic forces were addressed by Ellington et al. [13], Birch et al. [14] and Harbig et al. [15]. Their research demonstrated that the resulting high lift forces were influenced by the presence of a leading edge vortex which remained attached to the upper surface of the wing until stroke reversal. This vortex created a negative pressure region

above the wing that enhanced the generation of lift. The wake capture and rotational circulation unsteady mechanism was studied by Wang [16] to determine how the lift was affected by the enhanced velocity field generated during the flapping cycle. They concluded that flow circulation was induced as the trailing edge vortex was shed from the wing and dissipated into the wake to increase the velocity of the fluid relative to the wing. The enhanced velocity field exerted an additional upward momentum to the wing.

Further experimental characterizations of the structural dynamic behavior of insect wings were conducted. Rees [17] concluded that the corrugation of the wing could offer a reduction both in deflection and in the maximum stress experienced for a given loading. Ennos and Wootton [18] and Wootton [19, 20] determined experimentally that the bending and twisting of insect wings were highly dependent on their structure and venation morphology and that these altered the directions and magnitudes of the aerodynamic forces. Combes and Daniel [21, 22] studied the relationship between the venation pattern and wing flexibility and concluded that the veins were responsible for a spanwise-chordwise anisotropy flexural stiffness distribution which passively controlled the wing shape during flight. Zhao et al. [23] studied the impact of the elasticity of the insect wing on its aerodynamic efficiency and showed that the aerodynamic forces could be controlled by altering the trailing edge flexibility of the flapping wing. More recently, Mountcastle and Combes [24] underlined the importance of the wing flexibility in the hovering of a bumblebee, while Kang and Shyy [25] carried out simulations concerning insects of small size for low values of the Reynolds number showing that the deformability played a crucial role in the lift generation, enhancing the performance. In addition, Xiao et al. [26] highlighted the effect of torsional stiffness and inertia on the dynamics of low aspect ratio flapping wings.

1.3.2 Numerical Studies on Insect Wing Aerodynamics and Structural Behavior

The FE method proved to be a high-fidelity technique for studies regarding the structural response of insect wings. Wang et al. [27] and Li and Wang [28] studied the microstructures of wing veins and analyzed the effects on the mechanical behavior of the veins based on tensile and bending loading by the FE analysis. They observed that the veins of insects had a sandwich microstructure which could withstand a greater torsional deformation with minimal mass. Jongerius and Lentink [29] developed a FE model to determine the natural frequencies and the deformation response of a dragonfly wing subjected to analytical estimates of aerodynamic and inertial loads. Sims et al. [30] created a FE model of a hawk moth for the calculation of the modal characteristics.

Different studies have been developed to analyze the two-dimensional (2-D) and three-dimensional (3-D) fluid-structure interaction (FSI) of the insect wings and how it affects their structural dynamic behavior. Ishihara et al. [31] studied the 2-D FSI in *Dipterian* flapping flight and determined the cause of wing pitch changes. Yin and Luo [32] simulated the 2-D FSI in hovering flight to investigate the effect of inertia and fluid deformation on hovering performance. Young et al. [33] analyzed the aerodynamic consequences of wing deformation in the desert locust using a 3-D CFD simulation based on detailed wing kinematics. Their results showed that the time-varying wing twist and camber were essential to the maintenance of attached flow and the consequent reduction of the associated loss of energy dissipated into the wake; therefore, resulting in an overall increase of the aerodynamic efficiency. Dai et al. [34] modeled the 3-D FSI of an elastic rectangular wing at a low aspect ratio during hovering flight and showed that the chordwise deformation of the wing caused a passive dynamic pitching in addition to the active pitching applied at the wing root.

Complex numerical analysis with hybrid FSI formulations were conducted. These formulations often dealt with adaptive or moving meshes to investigate the aerodynamics of insect flight. The immersed boundary method (IBM) was among the accurate techniques for predicting insect flight aerodynamics [35, 36]. In particular, De Rosis et al. [36] considered a numerical approach that coupled the lattice Boltzmann method as the fluid solver and the Galerkin FE method as the structural solver to investigate the behavior of 2-D symmetric flapping wings moving in a viscous fluid. Su et al. [37] developed an unstructured mesh incompressible flow solver based on arbitrary Lagrangian-Eulerian (ALE) method to investigate the lift generation mechanisms of wings in hovering motions, including the wake capture, the delayed stall, the rapid pitch, as well as the clap and fling.

1.3.3 Manufacturing and Characterization of Artificial Insect-Sized Wings

The understanding of the structural response of the insect wing to aerodynamic loading has allowed the identification and development of suitable methods to manufacture insect-sized wings for biologically inspired MAVs. The research on the field of aerodynamics of insect flight advocates that the excellent maneuver skills during hovering and low-speed flight exhibited by aerial insects is strongly dependent on the presence of relatively flexible wings. The manufacturing of artificial wings for biologically inspired MAVs must not only attempt to replicate the aesthetics of the nature analogs but also to biomimic its morphology and flexibility in order to be able to emulate the structural dynamic performance of flying insects.

Different approaches have been considered to fabricate both single material and composite material insect-sized wings. For this purpose, micromolding, photolithography, and soft-lithography have been the most employed microfabrication techniques differing mainly on the materials selected to build the wing structure.

Pornsin-sirirak et al. [38] manufactured a composite wing structure by patterning a titanium-alloy metal onto a substrate to create the wing frame and attaching a Parylene-C film to act as the wing membrane. A flapping mechanism was designed to test both cicada and artificial insect-sized wings inside a wind-tunnel. Results suggested that the cicada wings had higher lift coefficients than the artificial wings possibly explained by the higher compliance of the natural wing.

The technique of soft-lithography was implemented by Tanaka et al. [39] to fabricate flexible polydimethylsiloxane (PDMS) molds with the shape and dimensions of an insect wing. These micromolds were used to cast a low-viscosity thermosetting polyurethane resin to create the structural veins and attach a Parylene-C film as the membrane. As an expansion of the previous approach, Tanaka et al. [40] studied the relationship between the stiffness distribution in the wing and the flight performance by fabricating three different types of wing and evaluating their performance in the free flight of an ornithopter. The wing that had a nonuniform stiffness distribution along the span provided the best result in terms of the aerodynamic force per unit weight and overall aerodynamic coefficients. Tanaka and Wood [41] developed corrugated artificial insect wings by micromolding a thermosetting resin using laser machined molds. Both techniques [39] [41] allowed the manufacturing of a single material wing structure.

Shang et al. [42] fabricated planar artificial insect-sized wings of diverse morphology through a versatile manufacturing process that combined smart composite microstructures with soft lithography. Insect-sized wings made of carbon fiber and a polyimide film for the biomimic of the veins and the membrane, respectively, were manufactured. Measurements of the spanwise and chordwise stiffness compared well with natural insect wings of equivalent span or chord

length. Their methodology was implement into the successful project of the Harvard Microrobotic Fly Robobee [43].

Xie et al. [44] fabricated a wing skeleton from carbon fibers cured inside a micromachined aluminum mold; hold together by a Capran film. Measurements of the time-averaged aerodynamic forces produced by the flapping wings in vacuum were conducted using a force and torque sensor. The deformation of the artificial flapping wing was measured using a digital image correlation (DIC) system. Results showed that the passive deformation of the wing was fundamental to create thrust.

Bao et al. [45] developed a composite artificial insect wing with a membrane made of PDMS and reinforced by SU-8 veins. Tests were conducted to measure the spanwise and chordwise flexural stiffness of the artificial wing.

1.3.4 Experimental Studies on Biologically Inspired Artificial Wings

Further research efforts were done in smart materials that could potentially biomimic the structural characteristics of insect wings. Different experimental setups were utilized for the measurement of the full-field deformation due to aerodynamic loading and the calculation of the aerodynamic coefficients of biologically inspired artificial wings.

Albertani et al. [46] documented both the elastic deformations using the DIC technique and the corresponding aerodynamic forces using a sting balance of a flexible wing made of a carbon fiber skeleton and a thin extensible rubber membrane.

Chakravarty [47] investigated the vibration characteristics of biologically inspired wings fabricated from composite polyester materials. The effect of added mass, aerodynamic pressure, and damping on the vibration characteristics of such wings were investigated. An inversely

proportional relationship was found between the magnitude of the natural frequency and the added mass. Moreover, Chakravarty and Albertani [48] investigated the effects of aerodynamic loads on the modal characteristics on a biologically inspired wing fabricated from a hyperleastic membrane. It was determined that the natural frequency of a membrane increased with prestrain level and that the damping of air had minimal effect on the natural frequencies of the wing but assisted on reducing the out-of-plane modal amplitude of vibration.

Wu et al. [49] studied the structural properties of hummingbird-shaped membrane wings fabricated from unidirectional carbon fibers and Capran by measuring the full-field deformation of the wing using a DIC system and characterizing the surrounding airflow using the stereo digital particle image velocimetry system at atmospheric pressure and in vacuum. The aeroelastic behavior of the artificial wings was described and the relationship between flexibility and thrust production was visually explained. Their research supported that wing deformation was a vital feature for generating aerodynamic thrust in insects.

The DIC technique has been employed for the estimation of the pressure distribution on the surface of artificial wings and the consequent prediction of the aerodynamic forces. Carpenter and Albertani [50] measured the elastic deformations and strains of a pliant membrane under aerodynamic loading using the DIC. The strain measurements were used to form virtual strain sensors which served as the sensory input to the estimation of the normal pressure distribution. Estimated pressure distributions were compared with a high-fidelity 3-D CFD. The coefficients of lift and pitching moment for steady state flow conditions were estimated and compared with measured wind-tunnel loads.

Banks et al. [51] developed a DIC based methodology that accurately captured the passive deformation of a foil wing structure under a fluid loading condition. The coupled deflection and blade twist for a range of wind speeds and angles of attack were evaluated. Steady deformations at low angles of attack were shown to be well-captured; however, unsteady deformations at higher angles of attack were observed as an increase in variability due to hardware limitations in the current DIC system.

Alioli et al. [52] conducted a membrane shape and load reconstruction from DIC measurements using the inverse FE analysis. They used DIC measurements to generate virtual strain sensors on the surface of the membrane. Measurement were further manipulated to remap the measured displacements and strains as needed to apply the inverse solution meshing of the FE method.

1.4 Concluding Paragraph

Nature provides multiple examples of biomechanical systems that operate efficiently. Researchers seek on them the inspiration to develop new concepts for their implementation in engineered systems that could potentially offer a better performance than traditional ones. The research on the field of aerodynamics of insect flight advocates that the excellent maneuver skills during hovering and low-speed flight mastered by aerial insects is strongly dependent on the presence of relatively flexible wings. Furthermore, the structure of an insect wing is evolutionary determined by the need to optimize the production of favorable aerodynamic forces during flight. Thus, to potentially emulate the structural dynamic performance of aerial insects, the manufacturing of artificial wings for biologically inspired MAVs must not only attempt to replicate the aesthetics of the nature analogs but also to biomimic its morphology and flexibility.

This investigation describes a method for designing, manufacturing, and characterizing the structural dynamic response of an artificial insect-sized wing. For this investigation, a crane fly (family *Tipulidae*) forewing was selected as the target specimen to be biomimicked. For this purpose, the artificial insect-sized wing was manufactured using the micro-fabrication technique of photolithography. At first, a micro-CT scan was conducted to characterize the internal and external morphologies of the forewing. A CAD model was developed from the micro-CT scan measurements. The photolithography process was then conducted using the CAD model as the template for the design of the photomasks and the faithful biomimicking of the morphology and flexibility of the insect wing. The natural frequencies and mode shapes of the artificial wing were determined using a vibrational experimental setup. Moreover, the time-varying deformation of the biomimetic insect-sized wing under different freestream velocities and angle of attack were determined using an aerodynamics experimental setup. A FE model of the artificial wing and a FSI simulation were developed to validate the experimental results.

CHAPTER 2 METHODOLOGY

2.1 Insect Specimen Description

A crane fly (family *Tipulidae*) forewing, shown in Fig. 2.1, was selected as the target specimen to biomimic its morphology and structural dynamic response. The selection basis was arbitrary within the framework of insect specimens that were proven to be aerodynamically efficient at low-speed flight and hovering [53, 54]. Morphological and kinematic parameters of the crane fly are presented in Table 2.1. Reported morphological parameters were averaged from individual specimen measurements performed by Ellington [54]; other morphological and kinematic parameters were extracted from Ishihara et al. [31] and Bao et al. [45].

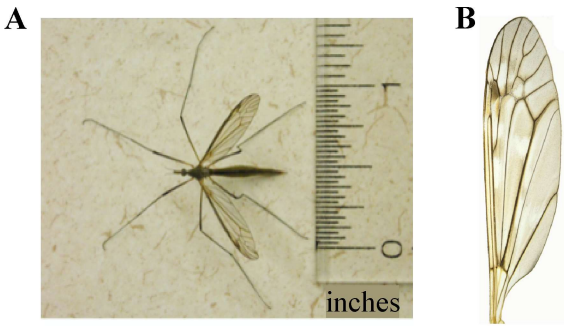

Figure 2.1 Crane fly specimens. *(A) Adult crane fly and (B) a sample of a crane fly forewing.*

Table 2.1 Reported morphological and kinematic parameters of the crane fly

Parameter	Reported values
Average span length per wing (mm)	13.2 [54]
Average chord length per wing (mm)	2.8 [54]
Average thickness of the membrane (μm)	7.2 [54]
Vein width (μm)	10–115 [45]
Vein thickness (μm)	6–69 [45]
Average wing pair mass (g)	0.000566 [54]
Flapping frequency (Hz)	45.5 [31]
Reynolds number	290 [31]

2.2 Micro-CT Scan of the Insect Wing

2.2.1 Overview

The wing structure of the crane fly forewing is a complex assembly made of a network of veins that intersect at multiple locations and that are attached to a thin membrane as seen in Fig. 2.1C. A meticulous visual inspection may reveal veins of different diameters that cannot be determined from this inspection. A high-fidelity 3-D characterization of the insect wing structure is required to identify key morphological design features that must be implemented on an artificial insect-sized wing for the successful biomimicry of the structural dynamic response of the nature analog. Because of the small scale, fragility, and complexity of the insect wing structure, the number of instruments and techniques capable of providing accurate quantitative and qualitative descriptions of the external and internal morphologies of the crane fly forewing are limited. One solution approach to this intrinsic problem is to reconstruct a 3-D image of the entire crane fly forewing using the micro-CT scan technique. This procedure is a nonintrusive 3-D microscopy technique—based on the principle of X-ray microtomography—which allows the reconstruction, visualization, and measurement of the wing geometry without any type of sample preparation; therefore, keeping intact the structural integrity of the insect wing.

2.2.2 Micro-CT Principle

The principle behind micro-CT is the measurement of the attenuation level of an X-ray signal after it has traveled through an object. A typical micro-CT scan setup is shown in Fig. 2.2 and it consists of the X-ray source, the specimen to be imaged which is mounted on a rotational stage, and the detector that measures the extent to which the intensity of the X-ray signal has been lessened by the sample. As the X-ray cone beam penetrates the specimen, the signal is

exponentially attenuated by scattering and absorption. The absorption rate of the X-ray signal through the object depends on the attenuation coefficients of the materials being scanned and in the length of the X-ray path through these materials as stated in Beer's law [55]. Partial absorption, meaning some of the X-ray photons are absorbed in the material while others are transmitted to the detector, and differential absorption, meaning that different materials within the object have different absorption characteristics to give contrast are required for a satisfactory micro-CT scan.

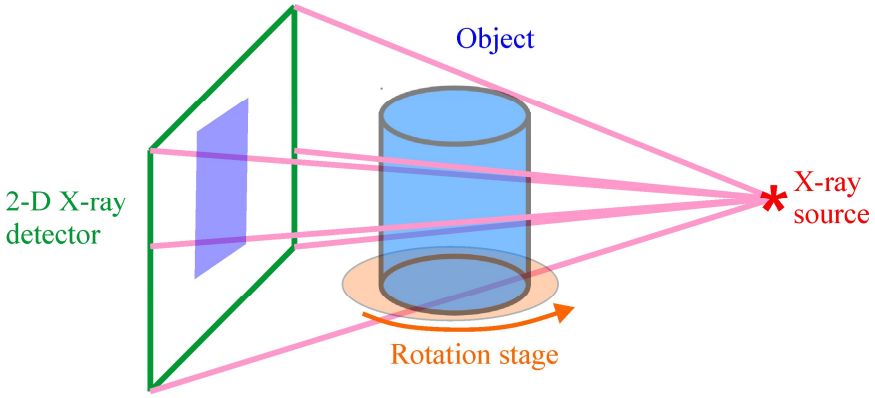

Figure 2.2 Typical micro-CT scan setup. *A view or projection is acquired by directing the X-ray signal through a slice plane of the object and collecting the intensity measurements on the detector for a given object position. The process is repeated for multiple angular views of the object.*

A so-called view or projection is acquired by directing the X-ray signal through a slice plane of the object and collecting the intensity measurements on the detector for a given position of the object. Next, either the specimen or the detector is rotated and another view is taken at the new position. This process is repeated for equiangular-spaced views until the object has rotated 180 deg or 360 deg. The set of views acquired are used to create 2-D images that are called slices because they are a representation of what would be seen if the object were sliced along the scan

plane. Lastly, the computer synthesizes the stack of virtual cross-sectional slices through the object to reconstruct the entire 3-D digital model [55].

2.2.3 Micro-CT Scanning Setup of the Crane Fly Forewing

The internal and external morphologies of the crane fly forewing wing must be characterized prior any attempt to manufacture an artificial wing structure that biomimics its structural performance. Specifically, it is necessary to determine the spatial coordinates, thicknesses, and cross-sectional profiles of both the membrane and the veins of the insect wing. For this purpose, a micro-CT scan of the crane fly forewing was conducted.

For this study, a SkyScan 1172 high-resolution micro-CT scanner [56] was used. A crane fly forewing was collected and placed inside the scanner chamber using one of the sample holders. No preparation was required on the sample; however, special care was taken to avoid damage or alteration to the structure of the wing. The acquisition settings of the scan were adjusted to achieve a good contrast between the different components of the wing, namely the membrane and the veins. This procedure was quite challenging given that the mass density of the membrane and the vein was quite similar; which, added to the miniature size of the wing, made the wing structure hard to appreciate in the preview snapshots.

In general, most of the acquisition settings were determined by trial and error; however, different trends were noticed during this experimental stage that facilitated the identification of optimal scanning settings. For this application, increasing the energy of the X-rays was not very effective as higher-energy beams of X-rays were less sensitive to attenuation as they traveled through the insect wing structure; thus, there was not sufficient differentiation, i.e. changes in material density and composition, between the membrane and the veins. Furthermore, the distinction between the components of the insect wing structure was better captured if no filter

was utilized between the specimen and the X-ray source. Since filters are commonly used to absorb the low energy beam of X-rays in the spectrum, it was furthered confirmed that the insect wing structure had a low rate of X-ray attenuation. Lastly, a small rotational step to complete an entire revolution around the specimen was desired due to the asymmetric features of the insect wing. The complete list of acquisition settings used for the scanning process of the crane fly forewing are presented in Table 2.2.

Table 2.2 Micro-CT scanning setup settings for the crane fly forewing

Parameter	Value
Source voltage (kV)	23
Source current (μA)	100
Filter	No filter
Object to source (mm)	169.420
Camera to source (mm)	273.504
Exposure (ms)	5400
Rotation step (deg)	0.250
Rotation degrees (deg)	360

2.2.4 Morphological Characterization of the Crane Fly Forewing

The reconstructed 3-D model from the micro-CT scan of the crane fly forewing is shown in Fig. 2.3. The different structural components of the forewing, including its veins distribution and the membrane, were accurately captured and distinguished by different gray scale values as seen in Fig. 2.3A. Furthermore, Figs. 2.3B and 2.3C present 2-D images of the cross-section of the wing at approximately half of its spanwise *y*-direction. Computational measurements of the thickness of the membrane, the spatial coordinates of the vein network, and the cross-sectional profiles of the veins were estimated using the SkyScan CT-Analyzer software version 1.13.2.1 [58] and the 2-D cross-sectional images of the reconstructed model.

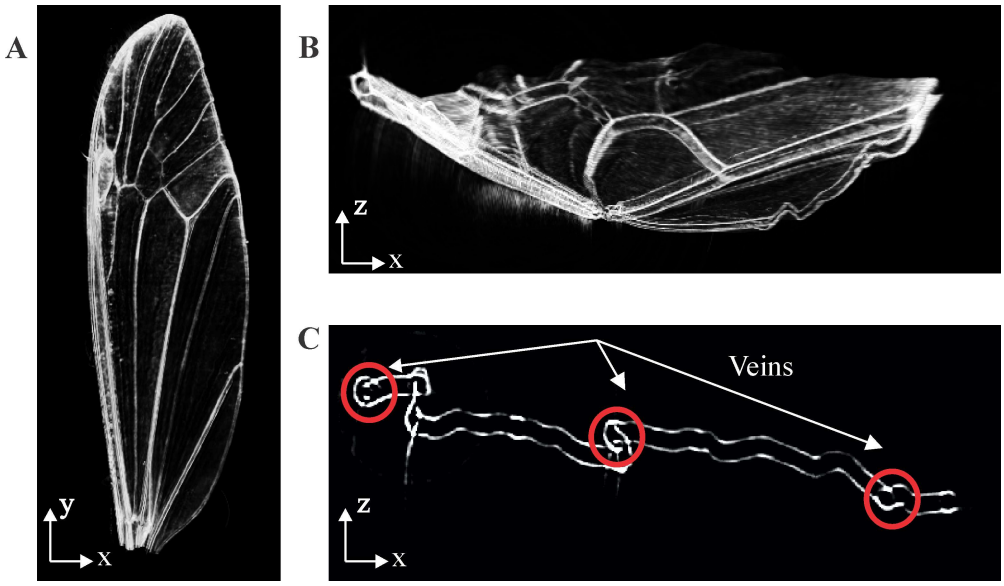

Figure 2.3 Reconstructed model from the micro-CT scan. *(A) 3-D reconstructed model of the crane fly forewing, (B) sliced-view of the reconstructed model at approximately a half its spanwise y-direction and (C) sample 2-D cross-sectional image [59].*

The analysis of the reconstructed micro-CT scan model of the insect wing allowed the characterization of its different morphological components. The crane fly forewing consisted of a thin membrane supported by a number of well-marked veins running along the span- and chordwise direction of the wing and connected to each other by cross-veins. An interesting characteristic was observed during the analysis of the internal morphology of the wing structure. Figures 2.3B and 2.3C show images of the cross-section at approximately half the span length of the wing. From these figures, two separated thin layers of cuticle were observed. The gap between these two layers was to some extent inaccurate since the insect wings consists of two layers of cuticle which are very close together, only separated at the positions where the veins are located [57]. The existence of this gap might be explained by the fact that the insect wing was not scanned immediately after being removed from the insect; thus the wing specimen lost moisture and the two layers of cuticle were slightly decoupled. Therefore, the total thickness of the membrane was approximated by averaging the thicknesses of these two layers of cuticle.

Using the sliced cross-sectional images from the reconstructed model, two different sets of tubular veins with different diameters were identified and estimated from averaging a set of measurements along the span of the insect wing. The venation network with the veins of different diameter created an asymmetric stiffness distribution along the span of wing. This was consistent with reports that supported that the Young's modulus and the flexural stiffness varied widely within the planform of an insect wing [22, 63, 67]. Furthermore, the existence of veins of different thicknesses has a role in the production of useful aerodynamic forces by the wing as a whole. On the leading edge of the wing, the longitudinal veins form a rigid structure supporting the wing as it moves through the air; whereas at the tip of the wing, the lack of veins of significant diameter creates a flexible region to enhance the twisting of the wing [57]. A summary of the main morphological parameters measured from the micro-CT model is presented in Table 2.3.

Table 2.3 Morphological parameters of the crane fly measured from the reconstructed micro-CT model

Parameter	**Measured values**
Average span length per wing (mm)	13.86
Average chord length per wing (mm)	3.01
Average membrane thickness (μm)	9.10
Thick vein diameter (μm)	126.55
Thick vein wall thickness (μm)	40.67
Thin vein outer diameter (μm)	105.10
Thin vein wall diameter (μm)	34.78

2.3 Computer-Aided Design Model of the Insect Wing

The commercially available modeling package Solidworks 2013 [60] was used to develop a CAD model of the crane fly forewing. The measurements from the reconstructed 3-D scanned model were written into a data file which was then imported into Solidworks. Spline curves were generated to develop the respective wing and vein contours shown in Fig. 2.4. The overall dimensions of the CAD model agreed with those presented in Table 2.3.

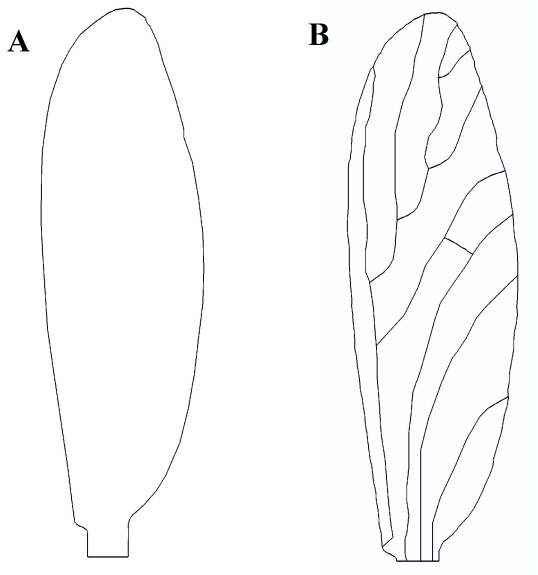

Figure 2.4 CAD model description of the crane fly forewing. *CAD model for the (A) Membrane contour and (B) vein contour of the crane fly forewing.*

Two sections of different vein thicknesses with tubular profiles were identified through the scan measurements and consequently implemented into the CAD model of the veins. The thicker veins were distributed near the root of the wing and along the leading and trailing edges of the wing. On the other hand, the presence of the thinner veins was more noticeable near the tip of the wing. The diameters and wall thicknesses of the two sets of veins was previously

presented in Table 2.3; however, their distribution along the span of the wing is introduced in Fig. 2.5.

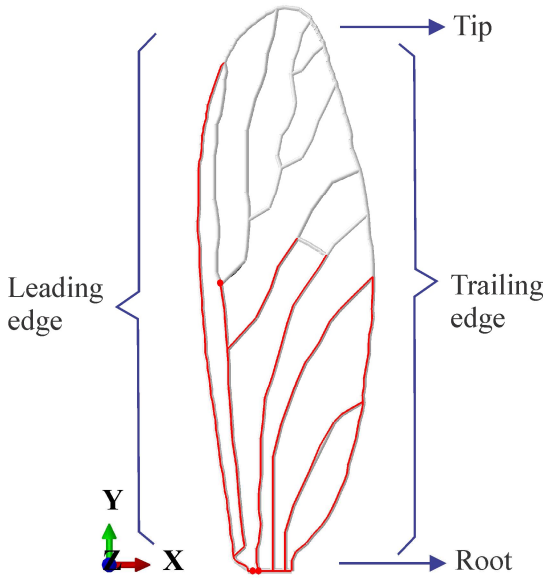

Figure 2.5 Thick veins and thin veins sets for the crane fly forewing. *Distribution of the thick (red lines) and thin (gray lines) veins on the CAD model of the crane fly forewing.*

2.4 Manufacturing of the Artificial Biologically Inspired Insect-Sized Wing

2.4.1 Overview

A microfabrication technique was required to biomimic with precision the structural complexity and the miniature scale of the crane fly forewing. For this purpose, the technique of photolithography was considered for the manufacturing of the artificial insect-sized wing. Photolithography refers to the use of an energy source—most commonly use is ultraviolet (UV) light—to pattern a substrate. Two different approaches were implemented. The first approach consisted on manufacturing a composite material wing structure in which the membrane was manufactured from a Kapton polyimide film and the vein network was patterned through

photolithography using the negative photoresist SU-8. The second approach entailed the manufacturing of a single material wing structure in which the membrane and the vein network were patterned onto the substrate through two consecutives photolithography processes using the negative photoresist SU-8 for both patterns.

2.4.2 Material Selection

2.4.2.1 Crane Fly Material Properties

The material properties for the crane fly forewing were required for selecting the appropriate materials for the biomimicking of the insect wing structure. After extensive literature survey, the authors did not find evidence of studies on the characterization of the Young's modulus for the membrane and the veins of the crane fly forewing. Nevertheless, the research on the mechanical properties of other insect species [63–64] and on the torsional and bending stiffness of the wing structures [21, 22, 66] showed that the veins of insects had a higher Young's modulus than that of the membrane. Therefore, following the observation that the crane fly forewing is a relatively flexible wing, an assumption similar to that from Sims et al. [30] was used for this study. The Young's modulus were assumed to be 1.9 GPa [30] and 4.0 GPa [30] for the membrane and the veins of the crane fly, respectively. Furthermore, the material density of the wing cuticle was considered to be 1200 kg/m^3 as measured in different insect samples by Wainwright et al. [62] and used by Ishihara et al. [31] and Jongerius and Lentink [29]. A Poisson's ratio of 0.495 was assumed as measured in some biological materials by Wainwright et al. [62]. The effects of the variation of Poisson's ratio were considered negligible as investigated by Combes and Daniel [21].

2.4.2.2 Biomimetic Materials Properties

The characterization of the material properties of the crane fly forewing allowed the identification of suitable materials with comparable mechanical properties. For this purpose, the Kapton film 50 HN from DuPont [70] and the negative photoresist SU-8-2050 from MicroChem [71] were selected for the biomimicking of the membrane and the veins of the crane forewing, respectively. The mechanical properties of the insect wing and the selected materials are summarized in Table 2.4.

Table 2.4 Mechanical properties of the artificial materials and the crane fly forewing

Wing component and materials		**Density (kg/m^3)**	**Young's modulus (GPa)**
Membrane	Kapton	1420 [70]	2.5 [70]
	Crane fly	1200 [30]	1.9 [30]
Veins	SU-8	1218 [71, 72]	4.0 [71, 72]
	Crane fly	1200 [30]	4.0 [30]

2.4.3 SU-8 and Photolithography

SU-8 is a negative photoresist prepared by dissolving EPON SU-8 resin [73] in an organic solvent such as propylene glycol methyl ether acetate (PGMEA), cyclopentanone, or gamma-butyrolactone (GBL) and adding up to 10 wt% of a photoinitiator [74]. The formulation SU-8-2050, which is commercially available from MicroChem [71], uses GBL as the casting solvent. The viscosity of the photoresist and hence the range of film thicknesses available are determined by the ratio of the solvent to the SU-8 resin. The EPON resin is an epoxy derivative that contains eight epoxy groups that explain the 8 in the name SU-8. This material has become widely use in the microfabrication industry because of its UV light absorption, high chemical

and thermal resistance, and good mechanical properties that make it suitable as a structural material [74].

Photolithography using SU-8 generally involves a set of basic processing steps: photoresist deposition, soft or prebaking, exposure, postexposure treatment, and developing. At first, the photoresist must be deposited and uniformly distributed on a clean substrate. Typical substrate materials include glass and silicon. The most common technique to deposit the photoresist is spin coating. The combination of spin speed and time selected for the spin coating step defines the final thickness of the film thanks to the centrifugal forces exerted on the substrate that cause the photoresist to flow to the edges, where it builds up until expelled when surface tension is exceeded [74, 75]. Thus, the resulting thickness of the resist is a function of the spin speed, spin time, and viscosity of the resist.

A soft bake or prebake is conducted following the deposition to evaporate the casting solvent from the SU-8 film. The use of a convection oven is not recommended since baking the photoresist layer in a convection medium evaporates the solvent present on the top of the photoresist first, hardens the surface, and hinders the evaporation of solvent from the bulk of the photoresist; therefore, the use of a hot plate is better suited and advisable [74, 75]. Elevated temperatures (>120 °C) during soft bake should be avoided because they could activate the polymerization of the resist.

The next step consists on exposing the substrate to UV light. Irradiation from an energy source generates a strong acid of low concentration that opens the epoxide rings of the resist and acts a catalyst for the cross-linking reaction [74, 75]. Typical energy sources include extreme, deep, and near-UV lights, X-rays, and ion and electron beams. The purpose of the illumination is

to deliver light with the proper intensity, directionality, spectral characteristics, and uniformity across the surface of the wafer, allowing a nearly perfect transfer of the mask image onto the resist in the form of a latent image [74, 75]. SU-8 is most commonly exposed using light in the near-UV range (350–450 nm), although the i-line (365 nm) is the recommended wavelength. UV light shorter than 350 nm is strongly absorbed near the top surface of the photoresist film, creating locally more acid that diffuses sideways along the top surface [74, 75]. This causes the surface of the resist layer to be overexposed while the bottom is underexposed. As a result, the walls of the photoresist film have a negative slope which greatly affects the resolution of the final pattern. This phenomenon is called T-topping and should be avoided [74].

The postexposure treatment consists of the further activation of the cross-linking reaction initiated during the exposure stage. This is achieved through the application of heat in a baking process conducted on a hot plate. It is recommended to progressively increase the temperature of the substrate to minimize the thermal stresses in the pattern [74].

The last step in a general SU-8 photolithography process is the development of the unexposed resist. The SU-8 is a negative type of photoresist; therefore, the photochemical reaction strengthens the polymer and becomes less soluble. The unpolymerized SU-8 is dissolved upon the immersion in a developer agent. Agitation during development is recommended to constantly feed developer to the resist pattern.

2.4.4 Photomask Design and Biomimicking of Wing Stiffness

The design and the fabrication of the photomask is fundamental for the successful conduction of a photolithography process. The photomask defines the regions that are exposed to UV light. These regions depending on the chemistry of the photoresist layer collectively define

either the positive or negative image of the to-be-transferred pattern. The photomask must have a high-resolution printout with excellent dimensional accuracy of the design to-be-transferred. For this investigation, two dark field masks were required—one corresponding to the overall membrane contour and the second one corresponding to the network of veins as shown in Fig. 2.6. The respective photomasks were printed on transparency film with a resolution of 10,000 DPI and were ordered from CAD/ART Services Inc. [76]. The photomasks required for the photolithography process were generated using the CAD models of the membrane and the veins of the crane fly forewing as templates. This guaranteed that the artificial wing was as similar as possible to the actual crane fly forewing. Furthermore, a small rectangular section was included at the bottom edge of each membrane and vein contours, as shown in Fig. 2.6, to have a segment where the wing could be securely handled and clamped for testing.

It was important to have an asymmetric stiffness distribution along the span of the wing to achieve a successful biomimic of the flexibility of an insect wing. Different studies concluded that the Young's modulus and the flexural stiffness of the wing declined both from the root to the tip of the wing and from the leading to the trailing edge [22, 63, 67]. To take into account the variation of stiffness along the span of the artificial wing, the two sets of veins with different diameter identified during the micro-CT scan measurements were implement into the design of the photomask. For this purpose, the line widths of the photomask of the vein network were matched with the thicknesses of the veins measured during the micro-CT scan. The dimensions of the veins were presented in Section 2.2.4 and Table 2.3 and the respective distribution along the insect wing was detailed in Section 2.3 and Fig. 2.5. This approach was analogous to that implemented by Sims et al. [30] in a numerical model of an hawk moth.

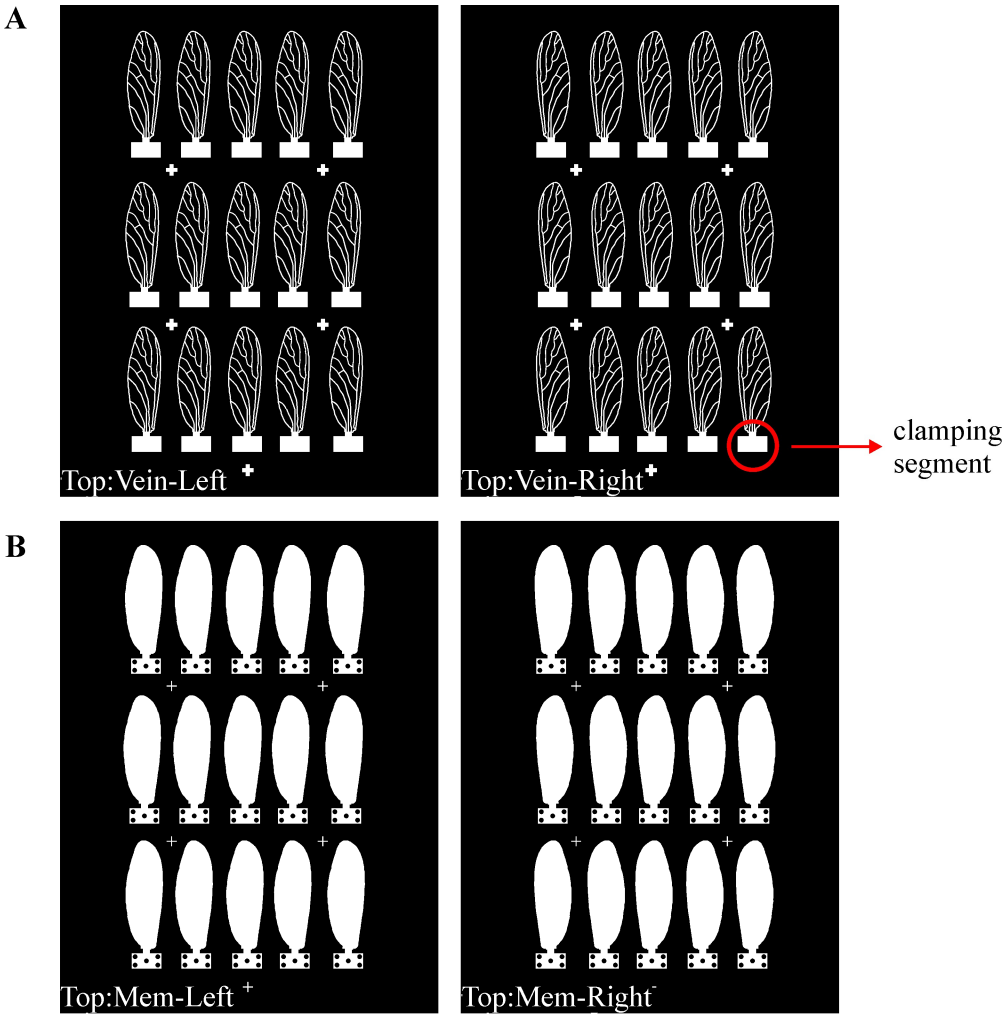

Figure 2.6 Photomask required for the manufacturing of the insect-sized artificial wing. *Dark field photomask with (A) membrane pattern and (B) venation pattern required for the manufacturing of the artificial insect-sized wing.*

2.4.5 Composite Material Artificial Insect-Sized Wing

The artificial vein structure was fabricated through photolithography using negative photoresist SU-8-2050 [71] and a Kapton film grade 50HN [70] was used as the membrane for the assembling of the composite material wing structure. The photoresist SU-8 and the Kapton film were selected due to their comparable mechanical properties with respect to the veins and the membrane of the crane fly forewing, respectively, as seen in Table 2.4. The recipe provided by the manufacturer [71] was followed for the selection of the spin coating time and speed, the

prebaking temperature and time, the exposure dose, the postbaking temperature and time, and the development time required for the optimal patterning of a specified thickness of negative photoresist SU-8. The photolithography process was conducted inside the cleanroom class 100 from the Advanced Materials Research Institute (AMRI) at the University of New Orleans. The cleanroom class 100 provided an effective environment with a low level of environmental pollutants—less than 100 particles in a cubic meter of air. The photolithography process for the manufacturing of the composite artificial insect-sized wing is described in the following sections and presented schematically in Fig. 2.7.

2.4.5.1 Conditioning of the Substrate Surface

A Silicon wafer was selected as the substrate to deposit the photoresist. The wafer was chemically treated prior entering the cleanroom to remove any external agents and impurities that would interfere with the resolution of the microfabrication process and to improve the adhesion properties of the substrate. Once inside the cleanroom, the wafer was rinsed with acetone, isopropyl alcohol, and deionized water to remove any remaining particulate matter from its surface. A thin Kapton film [70] was firmly attached to the substrate to act as the membrane of the wing structure and to pattern on it the vein network (Fig. 2.7A and B).

2.4.5.2 Deposition and Soft Bake of the Photoresist Film

The first layer of SU-8-2050 with a thickness of 100 μm required for the patterning of the venation network was uniformly distributed onto the surface of the substrate using the Spin Coater/Hotplate CEE-200-CB system [77]. Initially, the wafer was placed on the wafer platen from the resist spinner. The vacuum pump was turned on to held the wafer in place. A bulk amount of SU-8 was manually deposited on the center of the substrate. The wafer was spun initially at 500 rpm for 10 s with an acceleration of 100 rpm/s to spread the SU-8 on its surface.

Following, the wafer was spun at 1750 rpm for 30 s with an acceleration of 300 rpm/s to uniformly distribute the thin layer of SU-8 needed for the patterning of the veins (Fig. 2.7C).

The wafer was immediately removed from the vacuum chuck and placed on the hotplate to conduct the soft bake process. The soft baking guaranteed the removal of any remaining solvent in the photoresist to avoid mask contamination and to improve the resist adhesion to the substrate. The soft baking process was conducted in two steps to avoid drastic temperature changes for better lithography results. In the first step of the soft bake process, the temperature of the wafer was progressively increased from room temperature to 65 °C at a rate of 2 °C/min. The temperature of the wafer was dwelled at 65 °C for 5 min. In the second stage of the soft bake process, the temperature of the wafer was ramped up from 65 °C to 95 °C at a rate of 2 °C/min. The wafer was kept at 95 °C for 16 min. Higher temperatures should be avoided since they may activate an early, undesired thermal cross-linking of the SU-8 [74].

2.4.5.3 UV Exposure and Postexposure Treatment of the Venation Pattern

The transparency film mask with the outline of the vein network was aligned on top of the wafer using the mask aligner (Fig. 2.7D). The ink-side of the mask was placed on direct contact with the SU-8 coating. The resist-coated wafer was then exposed to UV light irradiated by the deep UV (220–260 nm) 500 W Oriel Flood Exposure Source model 97532 [78] using a Hg-Xe short arc lamp (Fig. 2.7D and E). The energy dose delivered to the SU-8 film was varied as part of a parametric study on the relation of exposure energy to wing stiffness. Four different batches of composite material artificial wings were manufactured by varying the UV exposure time of the resist-coated wafer.

The postexposure bake process of the wafer was conducted on a hotplate to complete the photoreaction initiated during the exposure. The temperature of the wafer was progressively increased from room temperature to 95 °C at a rate of 2 °C/min. An image of the pattern of the veins was noticeable after approximately one minute of reaching a temperature of 65 °C; this was an indication that the SU-8 coating was not underexposed. The temperature of the wafer was dwelled at 95 °C for 9.2 min. The substrate was allowed to cool-down to room temperature.

2.4.5.4 Development of the Unexposed Photoresist

The unexposed SU-8 was removed by immersing the substrate in a beaker with the respective MF-319 developer [71] (Step 2.8E). The wafer was immersed on the developer solution and manually agitated for approximately 8 min. During the development phase, the wafer was regularly rinsed with isopropyl alcohol to test if the unexposed SU-8 was completely removed. The development process was not complete if a white residue was present when rinsing with isopropyl alcohol. The wing structure was finally rinsed with deionized water and dried with the air gun.

2.4.5.5 Final Trimming of the Composite Material Artificial Insect-Sized Wing

The composite material wing structure was carefully removed from the wafer. A scalpel was used to closely trim the edges of the wing (Fig. 2.7F).

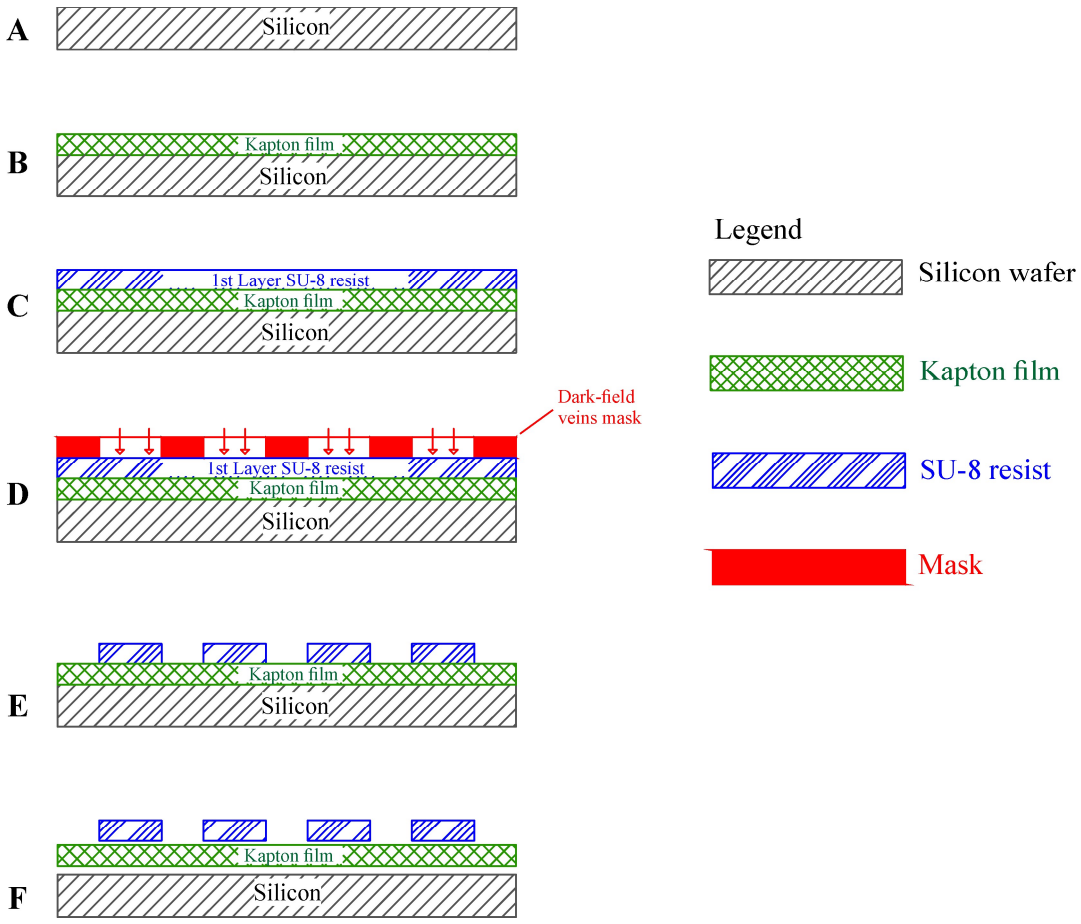

Figure 2.7 Description of the photolithography process for the manufacturing of the composite artificial insect-sized wing. *(A) Conditioning and cleaning of the surface of the wafer, (B) attachment of the Kapton film to the wafer to biomimic the membrane of the insect, (C) spin coating of the layer of the photoresist SU-8 to pattern the venation network on the substrate, (D) alignment of the photomask of the venation network and exposure to UV light to the substrate, (E) development of the unexposed SU-8, and (F) final trimming of the composite artificial insect-sized wing.*

2.4.6 Single Material Artificial Insect-Sized Wing

The patterns of both the membrane and the venation network were transferred onto the substrate by the cross-linking reaction of the negative photoresist SU-8 activated by the exposure to UV light. The photoresist SU-8-2050 [71] was selected due to its similar mechanical properties with respect to the crane fly forewing components as demonstrated in Table 2.4. The recipe provided by the manufacturer [71] was followed for the selection of the spin coating and baking parameters for the optimal patterning of a specified thickness of negative photoresist SU-

8. The photolithography process for the manufacturing of the single material artificial insect-sized wing is described below and presented schematically in Fig. 2.8.

2.4.6.1 Conditioning of the Substrate Surface

A Silicon wafer was selected as the substrate to deposit the photoresist. The wafer was chemically treated to remove any contaminants from the surface of the wafer. A thin Kapton film grade 50HN [70] was firmly attached to the substrate for the easier removal of the final structure (Fig. 2.8A and B).

2.4.6.2 Deposition and Soft Bake of the First Layer of Photoresist

The first layer of SU-8 with a thickness of 40 μm required for the patterning of the membrane of the wing was uniformly distributed onto the surface of the substrate using the spin coating system. At first, the wafer was placed on the wafer platen from the resist spinner. The vacuum pump was turned on to secure the wafer in place. A bulk amount of SU-8 was manually deposited on the center of the substrate. The wafer was spun initially at 500 rpm for 10 s with an acceleration of 100 rpm/s to spread the SU-8 on its surface. Then, the wafer was spun at 4000 rpm for 30 s with an acceleration of 300 rpm/s to uniformly distribute the first layer of SU-8 needed for the patterning of the membrane of the wing (Fig. 2.8C).

The wafer was immediately removed from the vacuum chuck and placed on the hotplate to conduct the soft bake process. The baking process was conducted in two steps to avoid drastic temperature changes for better lithography results. In the first step of the soft bake process, the temperature of the wafer was progressively increased from room temperature to 65 °C at a rate of 2 °C/min. The temperature of the wafer was dwelled at 65 °C for 3 min. In the second stage of

the soft bake process, the temperature of the wafer was ramped up from 65 °C to 95 °C at a rate of 2 °C/min. The wafer was kept at 95 °C for 6 min.

2.4.6.3 UV Exposure and Postexposure Treatment of the Membrane Pattern

The transparency film mask with the outline of the membrane was aligned on top of the wafer using the mask aligner (Fig. 2.8D). The ink-side of the mask was placed on direct contact with the SU-8 coating. The resist-coated wafer was then exposed to UV light delivered by the deep UV flood exposure source (Fig. 2.8D and E). The wafer was exposed to UV light for 8 min.

The postexposure bake process of the wafer was conducted on a hotplate to complete the photoreaction initiated during the exposure. The temperature of the wafer was progressively increased from room temperature to 95 °C at a rate of 2 °C/min. The temperature of the wafer was dwelled at 95 °C for 6 min. The substrate was allowed to cool-down to room temperature.

2.4.6.4 Deposition and Soft Bake of the Second Layer of Photoresist

The second layer of SU-8 with a thickness of 100 μm required for the patterning of the venation network was spun on top of the first layer of exposed and postexposure treated SU-8. The wafer was placed on the wafer platen from the resist spinner and a bulk amount of SU-8 was manually deposited on the center of the substrate. The wafer was spun initially at 500 rpm for 10 s with an acceleration of 100 rpm/s to spread the SU-8 on its surface. Following, the wafer was spun at 1750 rpm for 30 s with an acceleration of 300 rpm/s to uniformly distribute the second layer of SU-8 needed for the patterning of the venation network of the wing (Fig. 2.8F).

The wafer was removed from the vacuum chuck and placed on the hotplate to conduct the soft bake process. At first, the temperature of the wafer was progressively increased from room temperature to 65 °C at a rate of 2 °C/min. The temperature of the wafer was dwelled at 65

°C for 5 min. Following, the temperature of the wafer was ramped up from 65 °C to 95 °C at a rate of 2 °C/min. The wafer was kept at 95 °C for 16 min.

2.4.6.5 UV Exposure and Postexposure Treatment of the Venation Pattern

The transparency film mask with the outline of the veins was aligned on top of the wafer using the mask aligner (Fig. 2.8G). The ink-side of the mask was placed on direct contact with the SU-8 coated side of the wafer.

The energy dose delivered to the SU-8 film was varied as part of a parametric study on the relation of exposure energy to wing stiffness. Four different batches of composite material artificial wings were manufactured by varying the UV exposure time of the resist-coated wafer. The deep UV flood exposure source was used for the exposure step.

The postexposure bake process of the wafer was conducted on a hotplate. The temperature of the wafer was progressively increased from room temperature to 95 °C at a rate of 2 °C/min. The temperature of the wafer was dwelled at 95 °C for 9.2 min. The substrate was allowed to cool-down to room temperature.

2.4.6.6 Development of the Unexposed Photoresist

The unexposed SU-8 was removed by immersing the substrate in a beaker with the respective MF-319 developer [71] (Step 2.9H). The wafer was immersed and manually agitated for approximately 10 min. The wing structure was finally rinsed with isopropyl alcohol followed by deionized water and finally dried with the air gun.

2.4.6.7 Final Lift-Off of the Single Material Artificial Insect-Sized Wing

The single material wing structure was lifted-off from the Kapton film (Fig. 2.8I). A scalpel was utilized to carefully detach the artificial wing from the polyimide film.

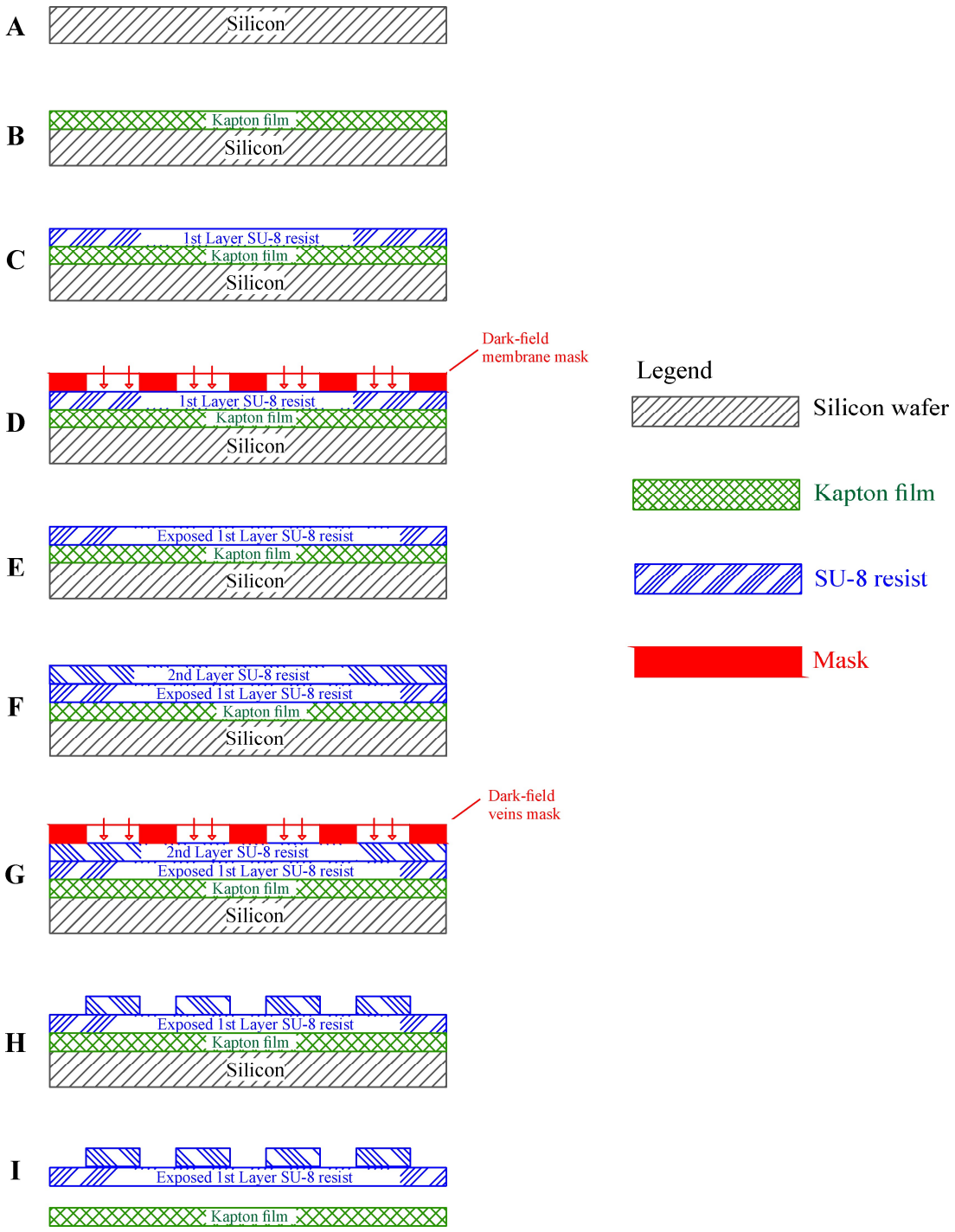

Figure 2.8 Description of the photolithography process for the manufacturing of the single material artificial insect-sized wing. *(A) Conditioning and cleaning of the surface of the wafer, (B) attachment of the Kapton film for the easier lift-off of the final wing structure, (C) spin coating of the first layer of the photoresist SU-8 to pattern the membrane on the substrate, (D and E) alignment of the photomask of the membrane and exposure to UV light to the substrate, (F) spin coating of the second layer of SU-8 to pattern the venation network on the substrate, (G) alignment of the photomask of the venation network and exposure to UV light to the substrate, (H) development of the unexposed SU-8, and (I) final lift-off of the single material artificial insect-sized wing.*

2.5 Experimental Modal Analysis of the Artificial Insect-Sized Wing

2.5.1 Overview

Modal analysis is an important tool for understanding the dynamic behavior of a structure. In general, a modal analysis consists on a series of steps that involve exciting the structure and measuring the excitation force, measuring the respective dynamic response, and processing the measured data to determine a set of modal parameters distinctive of the structure being analyzed. To determine the natural frequencies and mode shapes of the artificial wing, a broadband vibrational excitation signal was transmitted to the specimen using a modal shaker. The full-field deformation response of the artificial wing was captured using a DIC system. Following, the modal characteristics were determined from the Fourier analysis of the time-varying out-of-plane displacement of the artificial wing structure.

2.5.2 Fourier Analysis Theory

The principle behind the Fourier analysis is that any time-varying signal can be constructed by adding together a number of sinusoidal waves of appropriate frequency, amplitude, and phase. Hence, the Fourier analysis decomposes the excitation and the response signal in terms of their sinusoidal components to determine the respective frequency content or spectrum.

The Fourier analysis is conducted by calculating the Fourier transform. The continuous signal *f(x)* must meet two requirements to be able to calculate its respective Fourier transform *F(s)*: first, the area under the curve of the signal must be finite, i.e. the integral $\int_{-\infty}^{\infty} f(x)dx$ must exist; and second, any discontinuities in the signal must be finite [93]. The Fourier transform

F(s) of a continuous function *f(x)* and its inverse are defined mathematically in Eq. 2.2 and 2.3, respectively [93].

$$F(s) = \int_{-\infty}^{\infty} f(x) e^{-i2\pi xs} dx \tag{2.1}$$

$$f(x) = \int_{-\infty}^{\infty} F(s) e^{+i2\pi xs} ds \tag{2.2}$$

The Fourier transform of a continuous function or signal can be calculated from Eqs. 2.2 and 2.3 using analytical calculus. Nevertheless, most of the measured signals cannot be represented as continuous functions; instead, they must be digitized and considered as discrete signals. The discrete Fourier transform (DFT) must be implemented for discrete signals. The DFT *X(k)* of a discrete function *x(n)* and its inverse are mathematically defined in Eqs. 2.4 and 2.5

$$X(k) = \sum_{n=0}^{N-1} x(n) e^{\frac{-i2\pi kn}{N}} \qquad k = 0, ..., N-1 \tag{2.3}$$

$$x(n) = \frac{1}{N} \sum_{k=0}^{N-1} X(k) e^{\frac{+i2\pi kn}{N}} \qquad n = 0, ..., N-1 \tag{2.4}$$

where N is the total number of sample data and n and k are the counters for the function domain and the frequency domain discrete data, respectively.

Typical frequency measurements in vibration analysis include the calculation of the frequency response function (FRF) and the fast Fourier transform (FFT). The FRF is computed from two signals—namely the input (excitation) and the output (response) signals. The FRF is often called the “transfer function” as it describes the level of the input signal relative to the

output. In modal analysis, a common approach to calculate the FRF is to determine the ratio of the Fourier transform of the response signal to the Fourier transform of the excitation signal. Hence, the FRF is a complex signal with both magnitude and phase information. Mathematically, the FRF is defined in Eq. 2.6

$$H(s) = \frac{Y(s)}{F(s)} \tag{2.5}$$

Where *H(s)* is the FRF, *Y(s)* is the Fourier transform of the output signal *y(x)*, and *F(s)* is the Fourier transform of the input signal *f(x)*.

The FFT is an approach for the computation of the DFT that optimizes the speed of execution by eliminating redundant operations [93]. The calculation of the FFT requires the sampled signal in the function domain to be periodic—meaning it must be of finite extent and be able to repeat itself. When the FFT of a nonperiodic signal is computed, the FFT suffers from a phenomenon called leakage. Leakage is the effect of the signal energy smearing out over a wide frequency range and makes the frequency estimation inaccurate [93].

2.5.3 Modal Analysis Theory

The experimental modal analysis mainly involves two steps: first, to excite the structure using a vibrational signal of know spectra; and second, to measure and analyze the respective structural response of the specimen for the estimation of its modal characteristics.

Two excitation methods are commonly implemented: an impact hammer or a modal shaker. An impact hammer is a specialized instrument that produces short duration of excitation levels by striking the structure at a certain point. Different hammer tips can be used to change the

measurement frequency range of the impact. Using an impact hammer is practical for robust structures but inappropriate for fragile and small ones cannot withstand a direct external impact.

A modal shaker is commonly used for experimental modal analysis and it is the excitation method used in this investigation. Modal shakers are rated by the force they can produced. The modal shaker must be coupled or connected to the structure to be able to transmit the excitation signal. The shaker is usually attached to the structure using a long slender rod, called a stinger, so that the shaker can transmit the excitation force only along the axis of the stinger. A load cell is attached between the structure and the driving end of the stinger to measure the excitation force. Different accelerometers are usually attached on different points of the structure to monitor the respective response. The shaker is typically driven by a digital-to-analog controller, which is an electronic device that generates controlled electronic signals which are amplified and converted into an excitation signal.

2.5.3.1 Broadband Excitation Signals

Obtaining good measurements from an analyzer requires careful selection of the measurement settings for the averaging and windowing parameters necessary depending upon the broadband excitation signal employed. Averaging improves the estimate of the mean value at each frequency point by reducing the variance in the measurement and suppressing the background noise. It uses multiple data blocks to “smooth” the measurements. A linear average in which all the data blocks have the same weight is typically applied. It applies to both the time and the frequency domain.

Theoretically, the algorithm for computing the FFT requires the input single to be periodic in each data block. The calculation of the FFT of a nonperiodic signal will cause the

frequency domain data to have leakage. As explained previously, leakage is the effect of the signal energy smearing out over a wide frequency range. Since most signals are not periodic in the data block time period, windowing must be implemented to force them to be periodic. A windowing function should be exactly zero at the beginning and at the end of the data block.

A variety of broadband excitation signals have been developed for performing shaker measurements including pure random, burst random, sine sweep, and chirp. The characteristics of each of these broadband signals are detailed below.

The pure random signal is the most popular excitation signal used for shaker testing. This type of signal includes a broad range of frequencies and it has an unending nonrepeating random sequence. The main disadvantage of the pure random signal is that it is always nonperiodic in the time domain, meaning that it does not repeats itself over time; therefore, windowing and averaging must be applied to minimize leakage.

The burst random signal consists of a pure random or nonstationary pseudorandom signal followed by a portion of time with no excitation, meaning that the random signal is turned off prior to the end of the sampling window time period. This is done to allow the structural response to decay within the sampling window. Furthermore, it guarantees that both the excitation and the response signals are completely contained within the sampling window; hence, they are periodic and leakage free.

In sine sweep testing, the excitation signal consists of a sine wave at a single frequency at any time. The frequency itself; however, is varied with time. The sine sweep test may begin at a low frequency and then sweep to a high frequency, or vice versa. The sweeping rate can be either linear or logarithmic. Sine sweep testing is useful to verify the endurance of the structure or to

identify the structural behavior at a particular frequency. The main disadvantages of the sine sweep testing are the long test measurement times and the nonperiodic nature of the signal which produces leakage.

The chirp signal test is defined by a short profile that starts with a sine tone at a low frequency and then it is quickly swept to a high frequency usually in a time of seconds or less. After one sweep, the signal is turned off momentarily and then repeats itself. The quiet period is programmed to allow the structural response to damp out before the end of each time frame. This ensures that the excitation and respective responses are periodic within each time block; therefore, no window is required.

2.5.3.2 Excitation and Response Measurements

The excitation signal and the structural response can be measured using a variety of transducers. Commonly, a load cell is used to measure the driving excitation force; whereas, accelerometers are employed to measure the dynamic response of the system in terms of the acceleration levels at multiple locations of the structure. Both of these types of transducers are typically made of piezoelectric materials that generate an electrical charge when strained. The magnitude of this electrical charge is directly proportional to the physical quantity being measured. Thus, the force magnitude from the excitation force and the acceleration levels from the structural response can be determined from the measurement and analysis of the electrical signal of the respective transducer.

As an alternative, this investigation obtained the response in terms of the full-field deformation of the structure using the DIC system. The DIC is a noncontact optical measurement

technique that calculates the full-field displacements through the analysis of digital images as explained in Section 2.5.4.

2.5.4 Digital Image Correlation Theory

The DIC is an advanced non-contact optical measurement technique used to calculate the full-field shape and deformations of an object. The DIC has been identified as a superior deformation measurement method due to its full-field coverage, high-temporal and spatial resolution, and ease of use with minimum instrumentation needed [80].

The DIC requires the digital acquisition of the image of a random nonuniform speckled pattern applied on the surface of the object for its unloaded or initial configuration and throughout the loaded or analysis stage of the object. The basis of the DIC technique is the comparison of the digital images for various small regions of the speckle pattern—known as subsets— to locate and track the position of each of these subsets after deformation through digital image analysis [81].

The images of the speckled pattern are captured using digital imaging sensors, commonly referred as digital cameras. The use of one camera allows the reconstruction of shapes and the measurements of displacements in the in-plane direction only; whereas the implementation of two cameras, in the so-called stereo-triangulation configuration, allows the reconstruction of shapes and the measurement of displacements in both the normal and the out-of-plane directions. The concept of stereo-triangulation is depicted in Fig. 2.9A. This configuration recovers the 3-D structure of the environment by using two imaging sensors and computing the intersection of their respective optical rays at the features of interest as observed in Fig. 2.9A. The stereo-triangulation configuration requires calibration using special target specimens. During the

calibration, the DIC algorithm develops a model that includes the focal length, the image center, and the distortion of the lenses of the cameras; the distance and the angle of each camera relative to the other; and the geometry of the calibration target. Once the model is established, it can be used to locate the theoretical locations of the subsets of the acquired images from the analysis [81, 82].

Calibration is a process in which a so-called bundle adjustment algorithm determines the shape of the calibration target and the necessary calibration parameters [81]. The target does not need to be precisely flat or have a known shape to accurately calibrate the stereo system; however, the distance between at least two reference points on the target must be known to recover the absolute scale. For this purpose, targets with coded markers located at a known distance apart are used for automatic extraction as shown in Fig. 2.9B.

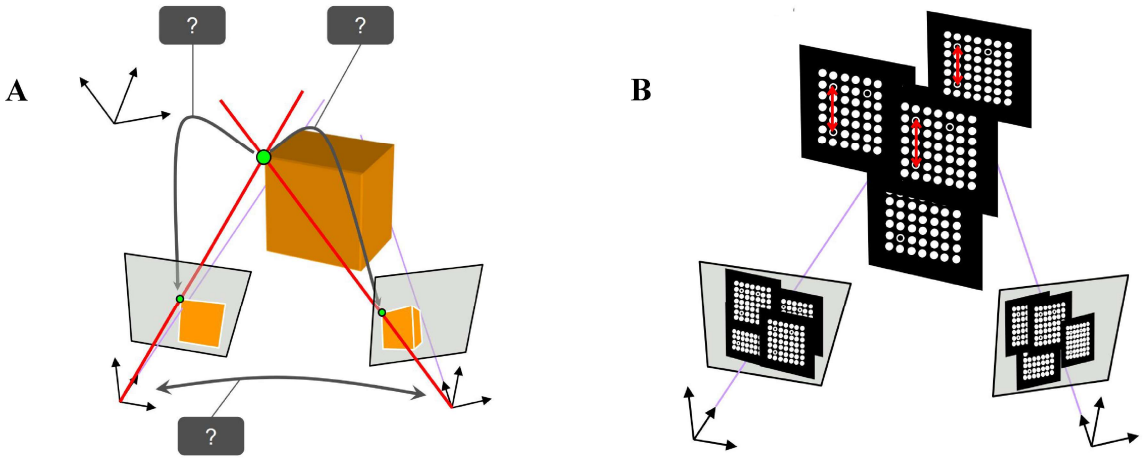

Figure 2.9 DIC calibration targets. *(A) The stereo-triangulation configuration requires calibration to locate the correct coordinate in space. (B) The bundle adjustment algorithm determines the shape of the calibration target by measuring the know distance between the coded markers; and thus, calculating the respective calibration parameters [82].*

The DIC technique tracks the changes in gray-scale value pattern in small collections of neighboring pixels called subsets during deformation. The specimen must be properly and densely speckled to perform this tracking correlation. Specifically, the surface of the specimen must have a non-repetitive, isotropic, high-contrast pattern; that is, the pattern must be random, should not exhibit a bias to one orientation, and should show a notably difference between the dark and white spots [83]. Furthermore, the pattern must be able to deform with the sample, not distort severely, and not reinforce the specimen. Examples of speckled patterns are shown in Fig. 2.10.

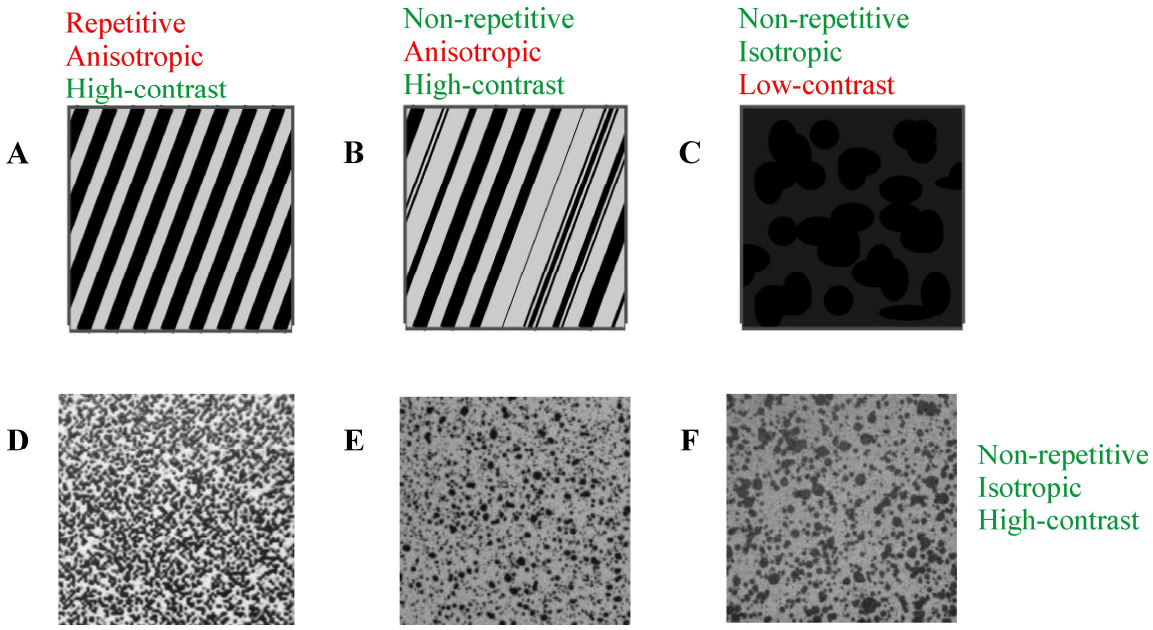

Figure 2.10 Speckled surface patterns. *(A, B, and C) Examples of inappropriate and (D, E, and F) proper speckled patterns for the DIC technique [82].*

Having the proper speckled pattern allows every subset of the digital image to have unique gray-scale information stored within it as an ordered array of numbers. Each of the pixels that define a particular subset is a number that describes the pixel intensity in terms of the gray-

scale. The most commonly used number of intensity levels is 256 gray levels, numbered from 0 (black) to 255 (white). For the aforementioned scale, it is said that the image has an 8-bit depth or that the image is able to store 8 bits per pixel. However, it is not uncommon to see 512 (9 bits-depth), 1024 (10 bits-depth), or 4096 (12 bits-depth) gray-scales.

To perform the tracking of subsets, a reference image is initially acquired and the respective subsets determined. For each subset, a unique array of numbers is generated based on the gray-scale intensity values of its pixels. The subset is shifted until the pattern in the deformed image matches that from the reference image as closely as possible; this match is calculated by analyzing the different bits or gray-scale values stored in each of the pixels within the subset. Since there might be possible matches at several locations, a classic correlation function based on the sum of squared differences of the pixel values is implemented to grade them and identify the correct match [81]. Lastly, the strains are computed from measured displacements of the object points. The subset tracking operation is presented schematically in Fig. 2.11.

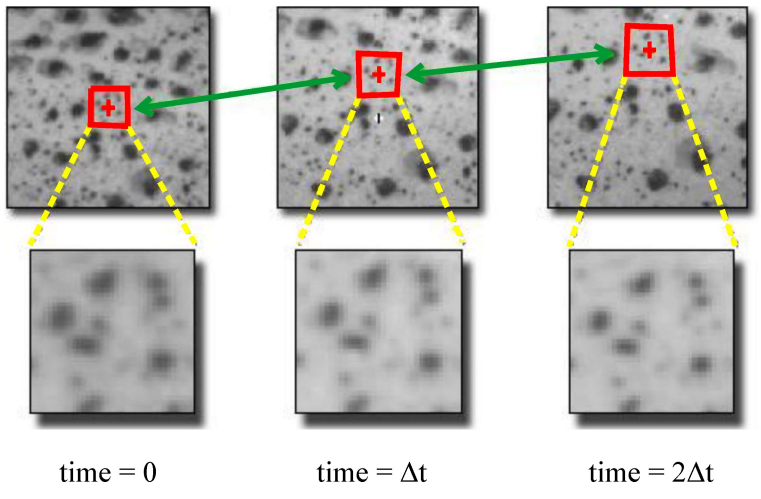

Figure 2.11 Subset tracking correlation. *The DIC technique tracks the changes in gray-scale value pattern in small collections of neighboring pixels called subsets, represented by the red squares, during deformation [83].*

On the early stages, the DIC was used mainly to measure planar translations and rotations, known as 2-D DIC image matching. Sutton et al. [81] identified more than 400 archival articles using the 2-D DIC technique within different fields such as fracture mechanics, material characterization, and mechanical behavior of a variety of composite and noncomposites materials and thin films. The 2-D image correlation; however, is limited to in-plane displacements and strains. The existence of a small out-of-plane motion would change the magnification and introduce errors in the measured in-plane displacements by the 2-D DIC technique. To overcome this limitation, the 2-D stereo-vision method was modified to include the effects of perspective on the subset shape, the use of a grid with a range of calibration motions, and the appropriate constraints on the analysis to include the presence of epipolar lines [81]. Due to the aforementioned advancements, the 3-D DIC technique is being used for a wide range of applications within the fields of fracture mechanics; material and structural characterization, and mechanical behavior of a variety of materials and structures. The 3-D DIC applications have included measurement of flexible wings undergoing aerodynamic loading [84, 85]; measurement of fracture undergoing mixed-mode loading [86, 87]; and material characterization in engineered materials [88, 89], bio-materials [90], and composites [91, 92].

2.5.5 Experimental Setup Description

The specimen must be subjected to a vibration excitation signal and the out-of-plane time-varying deformation response at multiple locations on the surface of the wing must be captured in order to determine the natural frequencies of the artificial insect-sized wing. The out-of-plane displacement data is then postprocessed and transformed to the frequency domain using the FFT [93]. The natural frequencies of the specimen appear as high amplitude data in the transform domain. For this purpose, the artificial insect-sized wing was mounted to the GW-V20

PAE100E Signal Force shaker from Data Physics [95]. The specimen was subjected to a random vibrational signal by the shaker. The excitation signal was generated by a 4-channel SignalStar Vector Vibration Controller from Data Physics [95], amplified by an 100 W Amplifier [95], and monitored by a 3005-B5 accelerometer from Dytran Instruments [96] with a sensitivity of 19.69 mV/g. The time-varying out-of-plane displacement data was captured using two FASTCAM MC2 high-speed cube cameras from Photron [97]. The DIC system and software were purchased from Correlated Solutions [98]. The images were acquired using the VIC-Snap software [99] and the postprocessing was conducted using the VIC-3D software [100]. A picture of the vibrations experimental setup is shown in Fig. 2.12.

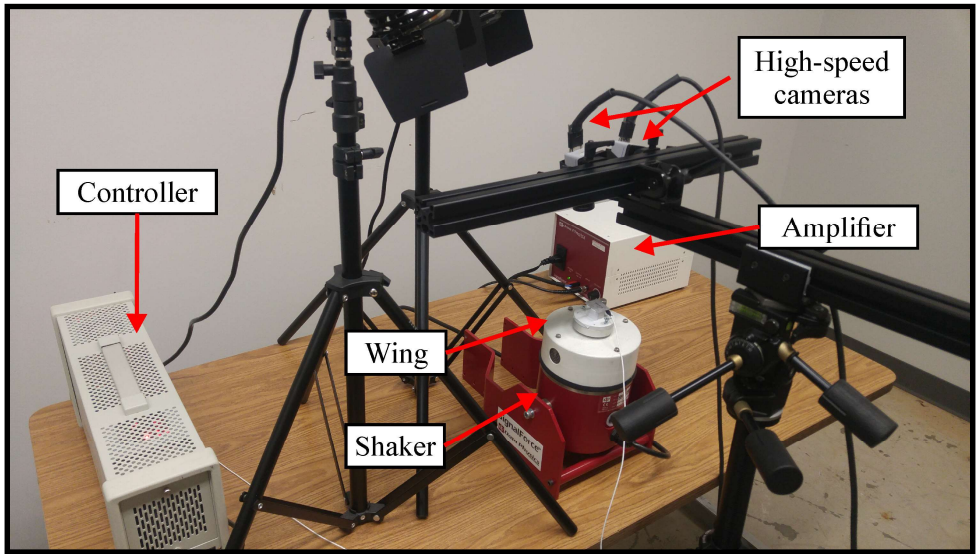

Figure 2.12 Description of the modal analysis experimental setup. *Illustration showing the controller, the amplifier, the shaker, and the high-speed cameras from the DIC system to conduct the experimental modal analysis.*

2.6 Experimental Aerodynamic Response of the Artificial Insect-Sized Wing

2.6.1 Overview

A body immersed in a moving fluid experiences a resultant force due to the interaction between the body and the fluid surrounding. This force can be described in terms of the pressure and shear stress distributions along the surface area of the immersed body. The resultant force in the direction of the upstream velocity is termed the drag force; whereas, the resultant force normal to the upstream velocity is known as the lift force. These two forces are well-known to be responsible for allowing the flight condition of wing structures.

For flexible wings, extensive literature has documented that the magnitudes and directions of the aerodynamic forces can be adjusted based on the pliant deformation response of the wing structure. It is of increasing interest, therefore, to be able to determine how the artificial wing would deform under aerodynamic and inertial loading. For this purpose, the full-field time-varying deformation of the artificial wing under aerodynamic conditions established by a low-speed wind tunnel was captured using the DIC system.

2.6.2 Experimental Setup Description

The artificial wing was mounted to the sting balance by a custom-manufactured socket that fits directly to the cylinder of the sting balance model 3/8 EWT from Aerolab [102]. The sting balance was implemented in this investigation solely to fix the artificial insect-sized wing inside the wind-tunnel. The sting balance could not be used to measure the aerodynamic forces in this investigation given that the resolution and sensitivity of the device was out of the range of the small force measurements required for the artificial insect-sized wing. Steady airflow conditions were established by adjusting the frequency of the motor of the subsonic wind tunnel.

The freestream velocity was measured using an air velocity transducer 8475 series from TSI Inc. [99]. The angle of attack was adjusted using the model-positioning system from Aerolab [102]. Furthermore, the time-varying deformations were captured using the DIC experimental setup. A picture of the aerodynamics experimental setup is shown in Fig. 2.13.

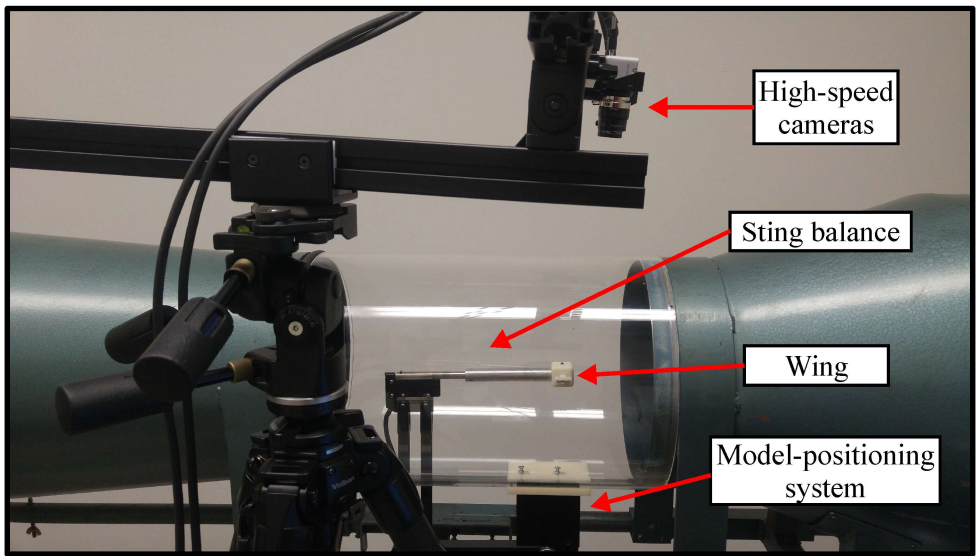

Figure 2.13 Description of the aerodynamics experimental setup. *Illustration showing the sting balance, the model-positioning system, and the high-speed cameras from the DIC system to conduct the aerodynamics experiments.*

2.7 Numerical Models of the Artificial Insect-Sized Wing

2.7.1 FE Model Description of the Artificial Insect-Sized Wing

The commercially available FE analysis package Abaqus 6.12 [61] was used to develop an Abaqus/Standard FE model of the artificial wing. The FE model consisted of two parts: the uniform thickness membrane and the network of veins. The membrane was modeled as a homogeneous shell with constant thickness and it included a short rectangular base which was also manufactured during the photolithography process. The veins were modeled as 2-D wires.

The photolithography process cannot generate hollow cross-sectional areas; thus, the 2-D wires were modeled with a rectangular cross-section. The network of veins included two sets of veins with different widths. Sections 2.2.4 and 2.3 discussed previously how these two sets of veins were determined and how they took into account the nonuniform stiffness distribution along the surface of the wing. Furthermore, the implementation of the two sets of veins in the manufacturing process of the artificial wing was described in detail in Sections 2.4.3.

The membrane was meshed using S4R (4-node general-purpose shell) type of elements with displacement and rotational degrees of freedom. The veins were meshed using B32 (3-node quadratic beam) type of elements with axial, bending, and torsional degrees of freedom. At the bifurcation of the veins, the nodes of the beam elements had rotational and translational degrees of freedom. The components of the FE model of the artificial wing with their respective mesh are shown in Figs. 2.14A–D.

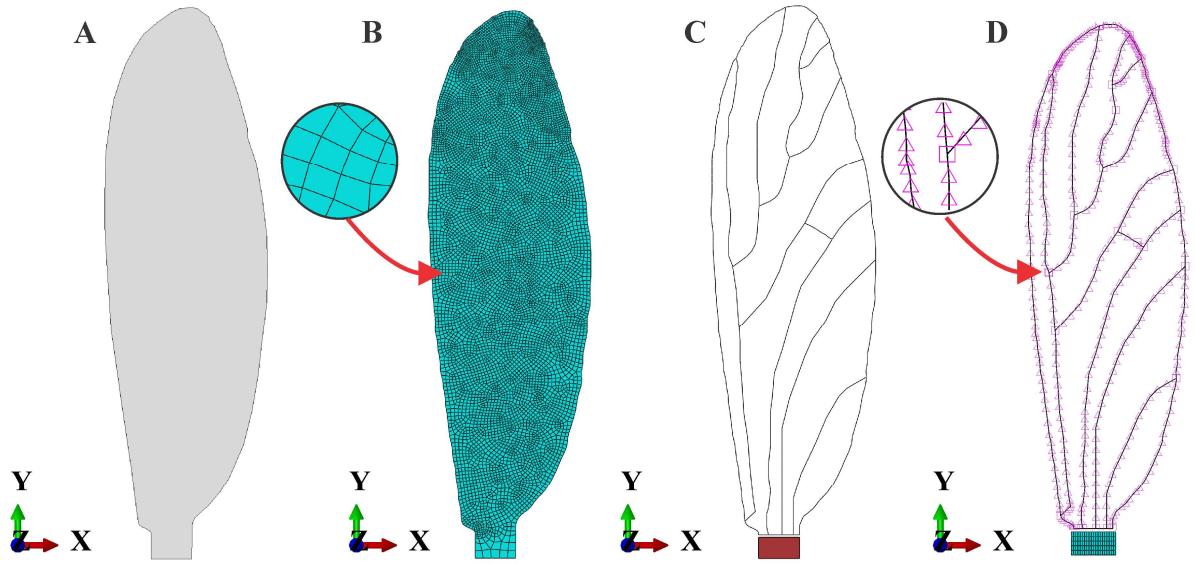

Figure 2.14 FE model description of the artificial insect-sized wing. *(A) Membrane model, (B) membrane mesh, (C) vein model, and (D) vein mesh of the artificial insect-sized wing.*

The material properties of the negative photoresist SU-8 were considered for the FE model of the single material artificial wing for both the membrane and the veins as presented in Table 2.4. The material properties of the Kapton film and the negative photoresist SU-8 were considered for the FE model of the composite material artificial wing for the membrane and the veins, respectively, as presented in Table 2.4.

A clamped condition with all degrees of freedom fixed was assigned at the bottom edge of the base of the membrane to simulate the corresponding condition of the insect wing attached to the flapping mechanism.

A so-called surface-based tie constraint with a node-to-surface formulation was implemented in the FE model to set a single-body deformable behavior between the membrane and the veins. This constraint was used to make all active degrees of freedom equal for the membrane and the network of veins. The tie constraint required the identification of a master and a slave surface. For this case, the master surface was the shell element-based membrane surface; while the slave surface was the node-based beam element network of veins. Nodes were tied only where the surfaces were close to one another. A position tolerance criterion was used to determine the constrained nodes based on the distance between the slave nodes and the master surface. For this case, the position tolerance criterion was equal to 5 % of the typical master facet diagonal length [68]. Slave nodes within this tolerance region were tied to the master surface. A schematic that exemplifies the tolerance region around the shell element-based membrane master surface is shown in Fig. 2.15.

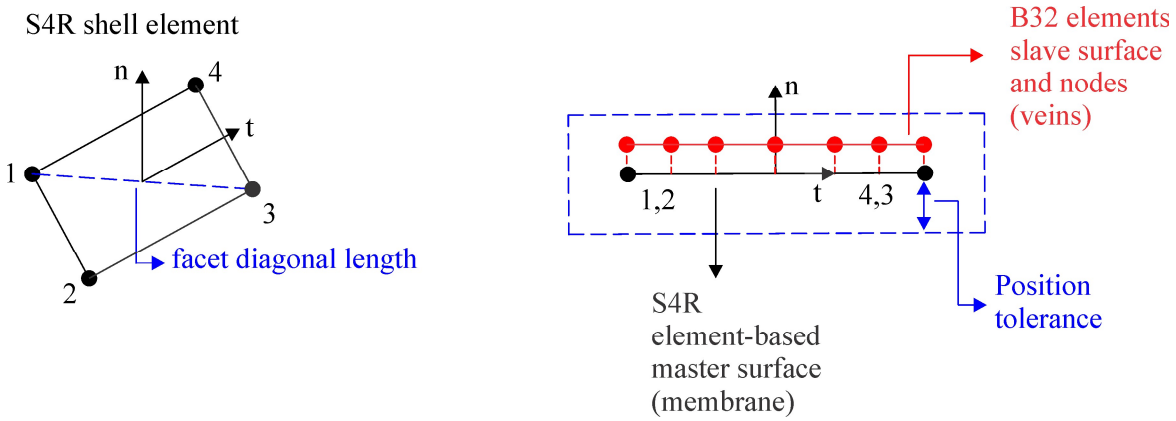

Figure 2.15 Tolerance region around the membrane master surface. *Description of the tolerance region where the slave nodes of the B32 elements were tied to the master nodes of the S4R elements of the FE model of the crane fly forewing [68].*

The criterion discussed previously was implemented to determine solely which slave nodes were tied to the master surface. It was also necessary to define how the master nodes and their respective tied slave nodes would be "communicating" with each other. For this purpose, a node-to-surface approach was implemented to interpolate quantities from the master nodes to the tied nodes. This approach set the tie coefficients equal to the interpolation functions at the points where the slave node projected onto the master surface. This approach was more efficient and robust for the complex surface under investigation [68]. Referring to Fig. 2.16, for instance, the master nodes *1*, *2*, *4*, and *5* are used to constrain node *a* of the slave surface.

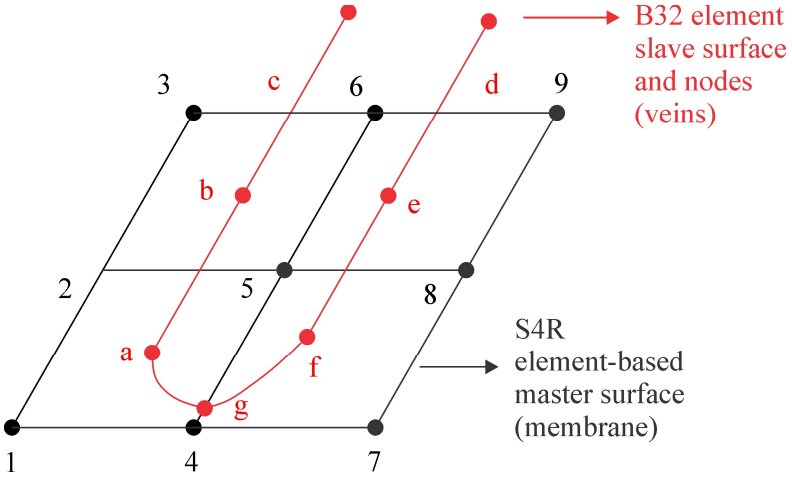

Figure 2.16 Node-to-surface tie constraint representation. *Description of the node-to-surface approach implemented to interpolate quantities from the master nodes to the tie point [68].*

2.7.2 CFD Model Description of the Artificial Insect-Sized Wing

The commercially available FE analysis package Abaqus 6.12 [61] was used to develop a CFD/Abaqus model of the surrounding airflow over the artificial wing. The CFD computational domain was modeled as a rectangular box that enclosed a seamed partition with the exact dimensions of the FE model of the artificial wing as shown in Fig. 2.17A. The CFD model was developed considering a length of 120 mm, a height of 40 mm, and a width of 50 mm. With these dimensions, the far-field and downstream boundaries were distant enough not to affect the flow behavior in the vicinity to the wing structure based on domain size limits suggested for CFD studies [69]. The fluid domain was meshed using FC3D8 (8-node linear fluid hexahedral) type of elements. The overall mesh of the CFD domain is presented in Fig. 2.17B. The mesh was refined near the seamed partition of the wing to reduce the aspect ratio between the elements of the CFD mesh and the elements of the FE mesh. This refinement was swept along the *z*-direction of the CFD domain as observed in Fig. 2.17C. Furthermore, layers were included to be able to capture the viscous effects near the wing surface as shown in Fig. 2.17D.

The fluid inside the CFD domain was modeled as incompressible air at standard atmospheric conditions. The fluid was modeled under these assumptions because of the low Reynolds number considered in this investigation. The air density and the dynamic viscosity of 1.225 kg/m^3 and 1.983×10^{-5} N·s/m^2 were assigned, respectively, as shown in Table 2.5.

Table 2.5 Fluid properties of the CFD model

Property	**Value**
Air density (kg/m^3)	1.225
Dynamic viscosity (kg/m·s)	1.983×10^{-5}

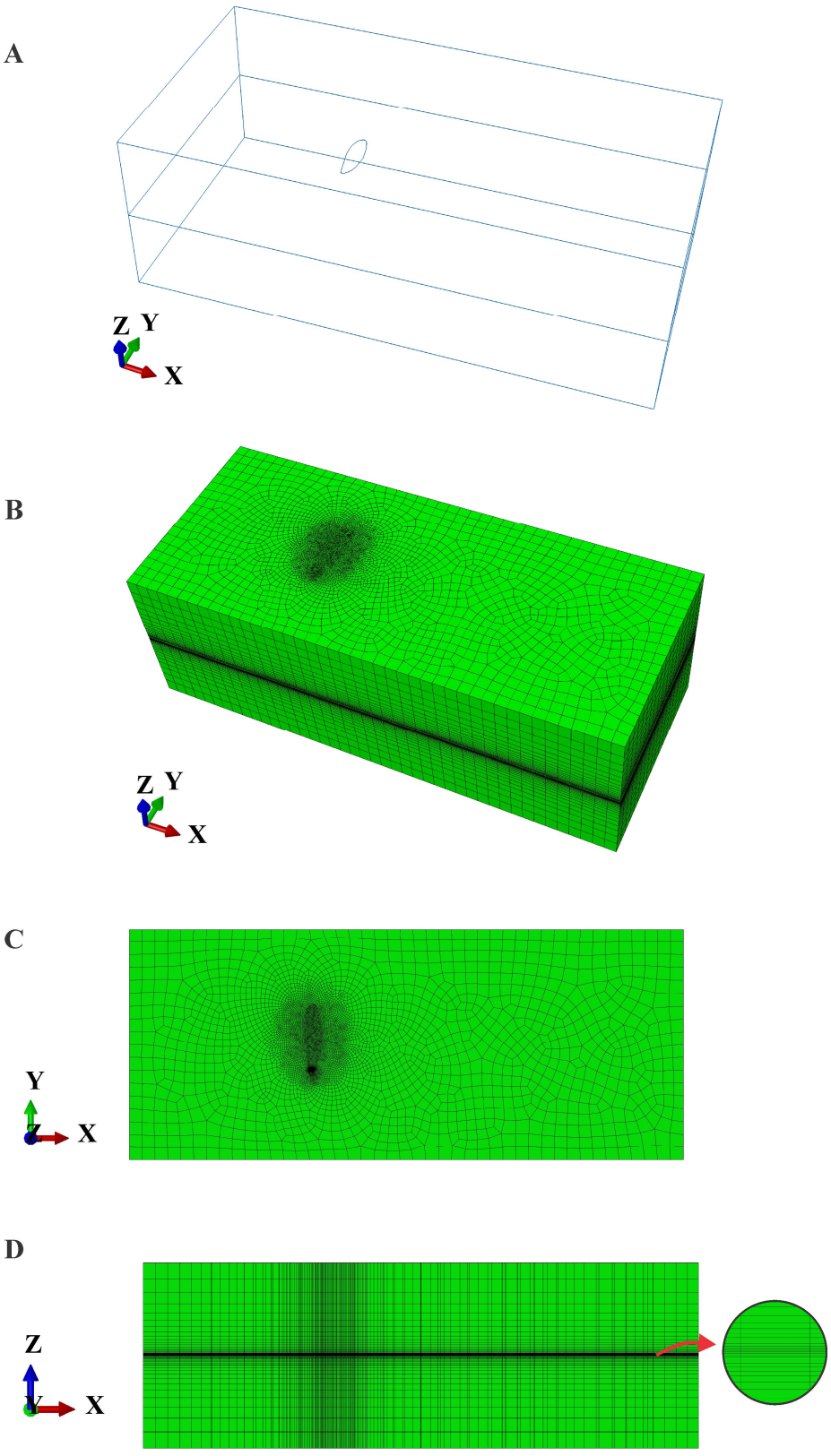

Figure 2.17 CFD model description of the artificial insect-sized wing. *(A) CFD domain (B) CFD mesh, (C) mesh refinement at the vicinity of the wing, and (D) mesh layers for capturing the viscous effects.*

The CFD formulation required the specification of boundary conditions to state a well-posed mathematical problem. Four boundary conditions were specified on the fluid domain: inlet velocity, far-field velocity, outlet pressure, and symmetry velocity; and two boundary conditions were assigned on the mesh: fixed and symmetry deformations. There was no need to apply a wall boundary condition at the wing seam because this was automatically assigned by the selection of the co-simulation interfaces described in Section 2.7.3.

The boundary conditions must also represent the physics of the flow surrounding the insect wing. For this purpose, an investigation of the Reynolds number typically sustained by the crane fly was conducted to determine the physics of the flow, e.g. whether the flow was laminar or turbulent and to determine the magnitude of the velocity at the very far upstream of the wing, also known as the freestream velocity. The crane fly operates at a Reynolds number of 290 [31]. Therefore, boundary conditions were applied on the fluid domain for different freestream velocities between the range of 10 mm/s to 1000 mm/s which corresponds to a Reynolds number of 2.9 and 290, respectively. The flow was modeled as laminar flow due to the low Reynolds number compared to the critical Reynolds number ($Re=5\times10^5$) at which the external flow would be considered turbulent. A summary of the boundary conditions is presented in Table 2.6 with reference to Fig. 2.18.

Table 2.6 Boundary conditions of the CFD model

Boundary condition	**Face**	**Parameter**
Steady inlet velocity in *x*-, *y*-, and *z*-directions (mm/s)	Inlet *y*-*z* plane	$v_x = V_\infty \cos\alpha;\ v_y = 0;\ v_z = V_\infty \sin\alpha$
Steady outlet pressure (Pa)	Outlet *y*-*z* plane	$p = 0$
Steady far-field velocity in *x*-, *y*-, and *z*-directions (mm/s)	Far-field top and bottom *x*-*y* planes	$v_x = V_\infty \cos\alpha;\ v_y = 0;\ v_z = V_\infty \sin\alpha$
Steady symmetric velocity in *z*-direction (mm/s)	Symmetry front and back *x*-*z* planes	$v_z = 0$
Mesh fixed deformation in *x*-, *y*-, and *z*-directions (mm)	Inlet, outlet, and far-field	$U_x = 0;\ U_y = 0;\ U_z = 0$
Mesh symmetric deformation in *z*-direction (mm)	Symmetry	$U_z = 0$

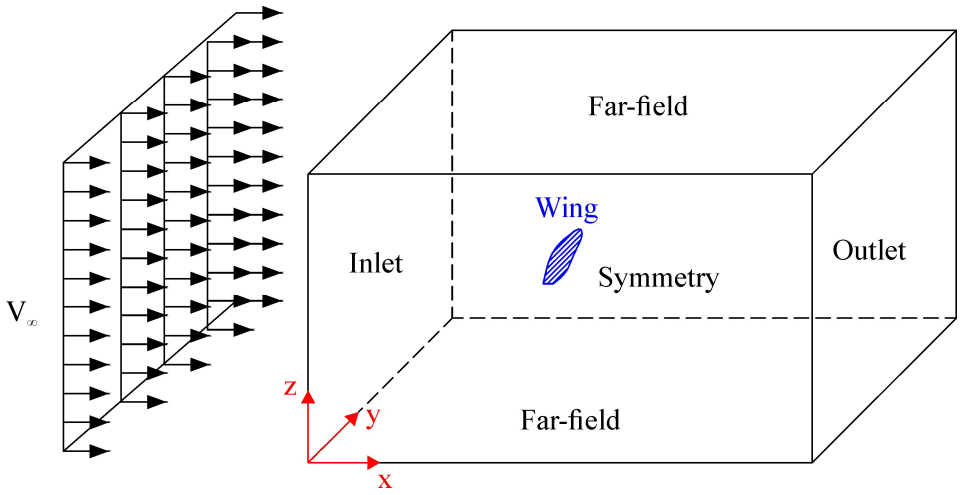

Figure 2.18 Boundary conditions surfaces of the CFD domain. *Description of the different faces of the CFD domain for the assignment of the boundary conditions.*

2.7.3 FSI Model Description of the Artificial Insect-Sized Wing

The FSI represents a class of multi-physics problem where fluid flow affects compliant structures, which in turn affects the fluid flow. Such behavior requires the structural and fluid equations to be solved independently and interface loads and boundary conditions to be exchanged after a converged increment. In this study, the Abaqus/CFD model consisting of the fluid domain was coupled with the Abaqus/Standard FE model consisting of the crane fly forewing through the co-simulation engine. Co-simulation interfaces across which data were exchanged during the co-simulation analysis were identified on each model. For the FE model, the fluid-structure interfaces were selected at both the bottom and top shell surfaces. Similarly, for the CFD model, the fluid-structure interface was allocated to the seamed partition with the exact geometry of the insect wing located inside the fluid domain. The co-simulation interfaces are presented in Fig. 2.19.

Distortion control and mesh smoothing tools were implemented on the numerical models. A smoother mesh was generated at regular intervals near the co-simulation interface of the CFD model to reduce the distortion of the elements and to maintain good element aspect ratios. The same mesh topology was maintained—the number of elements and nodes and their connectivity did not change. A distortion control option was implemented to prevent the development of negative element volumes during the CFD meshing movement.

A frequency linear perturbation analysis step was selected to perform a modal analysis. The Lanczos eigensolver was selected to determine the first three natural frequencies and mode shapes of the FE model of the artificial wing. For the FSI simulation, a dynamic-implicit step was selected in the FE model and an incompressible laminar flow analysis step was selected in the CFD model to determine the deformation response of the wing under steady airflow.

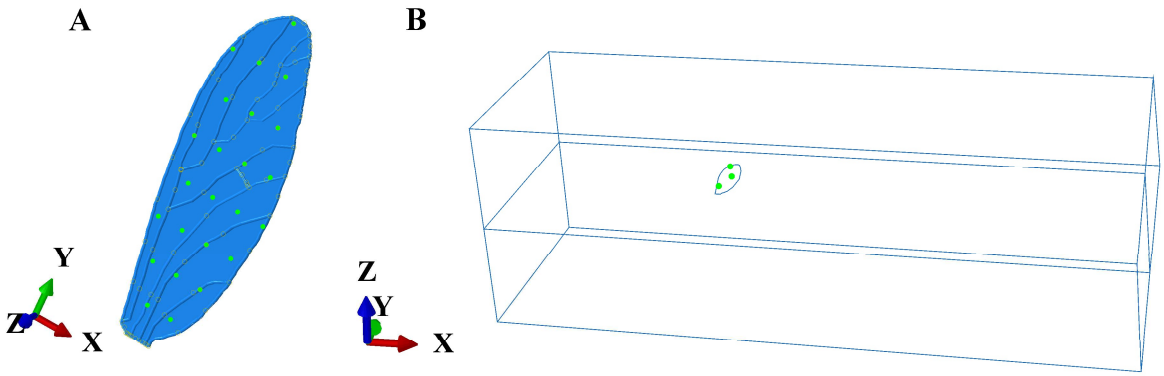

Figure 2.19 Co-simulation interfaces descriptions for the artificial wing FSI model. *(A) For the FE model and (B) for the CFD model.*

CHAPTER 3 MATHEMATICAL FORMULATION

The FSI represents a class of multi-physics problem where fluid flow affects compliant structures, which in turn affects the fluid flow. This section presents the governing differential equations for the FSI problem and the solution technique implemented to solve them.

3.1 Fluid Domain

3.1.1 General Vector Form of the Conservation Equations

The problem of flow over an immersed body describes the fluid model from the FSI simulation. The flow over an immersed body is governed by the conservation laws. The most general vector form of the conservation of mass and the conservation of momentum valid for steady and unsteady flows, laminar and turbulent flows, compressible and incompressible flows, viscous and inviscid flows, and Newtonian and non-Newtonian fluids are given in the so-called conservative form in Eqs. 3.1 and 3.2, respectively.

Conservation of mass (conservative form):

$$\frac{\partial \rho}{\partial t} + \vec{\nabla} \cdot (\rho \vec{V}) = 0 \tag{3.1}$$

Conservation of momentum (conservative form):

$$\frac{\partial \left(\rho \vec{V}\right)}{\partial t} + \vec{\nabla} \cdot \left(\rho \vec{V} \vec{V}\right) = \rho \vec{g} + \vec{\nabla} \cdot \tau_{ij}$$

$$where \tag{3.2}$$

$$\tau_{ij} = \begin{pmatrix} \tau_{xx} & \tau_{xy} & \tau_{xz} \\ \tau_{yx} & \tau_{yy} & \tau_{yz} \\ \tau_{zx} & \tau_{zy} & \tau_{zz} \end{pmatrix}$$

3.1.2 Assumptions

The following assumptions are considered for the fluid domain of the FSI study:

1) The system is at steady state—there is no change with respect to time of any variable or property.
2) The flow is incompressible.
3) The flow is 3-D.
4) The flow is laminar with a Reynolds number less than the Reynolds critical number for external flow which is equal to 5×10^5.
5) The properties of the fluid remain constant.
6) The fluid is Newtonian—there is a linear relationship between shear and strain.

3.1.3 Governing Differential Equations

Considering the assumptions stated previously, the conservation equations in vector form Eqs. 3.1 and 3.2 can be deduced to

Conservation of mass (conservative form for incompressible Newtonian fluid):

$$\vec{\nabla}\cdot\vec{V}=0 \tag{3.3}$$

Conservation of momentum (conservative form for incompressible Newtonian fluid):

$$\vec{\nabla}\cdot\left(\rho\vec{V}\vec{V}\right)=\rho\vec{g}-\vec{\nabla}p+\mu\vec{\nabla}^2\vec{V} \tag{3.4}$$

Equations 3.3 and 3.4 can be expanded and presented in Cartesian coordinates as follows

Conservation of mass:

$$\frac{\partial v_x}{\partial x}+\frac{\partial v_y}{\partial y}+\frac{\partial v_z}{\partial z}=0 \tag{3.5}$$

Conservation of momentum:

x-direction:

$$\frac{\partial\left(\rho v_x^2\right)}{\partial x}+\frac{\partial\left(\rho v_x v_y\right)}{\partial y}+\frac{\partial\left(\rho v_x v_z\right)}{\partial z}=-\frac{\partial p}{\partial x}+\rho g_x+\mu\left(\frac{\partial^2 v_x}{\partial x^2}+\frac{\partial^2 v_x}{\partial y^2}+\frac{\partial^2 v_x}{\partial z^2}\right) \tag{3.6}$$

y-direction:

$$\frac{\partial\left(\rho v_y v_x\right)}{\partial x}+\frac{\partial\left(\rho v_y^2\right)}{\partial y}+\frac{\partial\left(\rho v_y v_z\right)}{\partial z}=-\frac{\partial p}{\partial y}+\rho g_y+\mu\left(\frac{\partial^2 v_y}{\partial x^2}+\frac{\partial^2 v_y}{\partial y^2}+\frac{\partial^2 v_y}{\partial z^2}\right) \tag{3.7}$$

z-direction:

$$\frac{\partial\left(\rho v_z v_x\right)}{\partial x}+\frac{\partial\left(\rho v_z v_y\right)}{\partial y}+\frac{\partial\left(\rho v_z^2\right)}{\partial z}=-\frac{\partial p}{\partial z}+\rho g_z+\mu\left(\frac{\partial^2 v_z}{\partial x^2}+\frac{\partial^2 v_z}{\partial y^2}+\frac{\partial^2 v_z}{\partial z^2}\right) \tag{3.8}$$

3.1.4 Boundary Conditions

Equations 3.5–3.8 are nonlinear second order partial differential equations that require the specification of Neumann, Dirichlet, or mixed type of boundary conditions to state a well-posed mathematical problem. The boundary conditions of the fluid domain are presented in the following section.

At the inlet surface, the velocity must be equal to the freestream velocity V_∞. Mathematically, this boundary condition is defined as

$$v_x = V_\infty;\ v_y = 0;\ v_z = 0 \tag{3.9}$$

At the outlet surface, the sum of the static and dynamic pressure must be zero. This boundary condition is defined mathematically as

$$p_{total} = 0 \tag{3.10}$$

The boundary conditions at the far-field surfaces requires that the velocity must be equal to the freestream velocity V_∞. This condition is imposed because the location of the far-field is distant enough to be unaffected by the interaction of the fluid with the immersed body. Mathematically, the far-field boundary condition assigned at the far-field surfaces is defined as

$$\begin{gathered} v_x = V_\infty;\ v_y = 0;\ v_z = 0 \\ or \\ \frac{\partial v_x}{\partial y} = \frac{\partial v_x}{\partial z} = 0 \end{gathered} \tag{3.11}$$

The boundary conditions at the fluid-solid interface refers to the no-slip condition which states that the fluid must stick to the surface of the immersed body due to viscous effects. The no-slip boundary condition assigned to the fluid-solid interface is mathematically defined as

$$v_x = 0;\ v_y = 0;\ v_z = 0 \tag{3.12}$$

3.1.5 Solution Procedure

The Abaqus/CFD is used as the numerical solver to solve the well-posed mathematical problem stated by the governing differential equations in Eqs. 3.6–3.9 and the respective boundary conditions defined in Eqs. 3.9–3.12.

The Abaqus/CFD uses the finite volume method to discretize the governing differential equations of the fluid domain. The finite volume method transforms the coupled nonlinear conservation equations into a system of algebraic equations by discretizing the entire fluid

domain into small regions called control volumes and integrating the conservation equations over each of these control volumes. The primitive variables—namely density, temperature, pressure, velocity—are typically defined at the center of each control volume or cell. The second-order accurate least-square gradient estimation method is implemented to determine the gradients at the cell faces for the diffusive and convective terms.

The discretized equations must be solved by numerical methods. For this investigation, the solution approach is based on the second-order accurate SIMPLE (Semi-Implicit Method for Pressure Linked Equations) method. The SIMPLE scheme is an iterative pressure-based solver. The main idea of this scheme is to deduce a pressure correction equation from the continuity equation and solve it to obtain a pressure correction field which in turn is used to update the velocity and pressure fields. These guessed fields are progressively improved through the iteration process until convergence is achieved for the velocity and pressure fields. When coupled with other governing variables such as temperature and turbulent quantities, the calculations are solved sequentially for a specified number of iterations. The algorithm of the SIMPLE process is shown in Fig. 3.1.

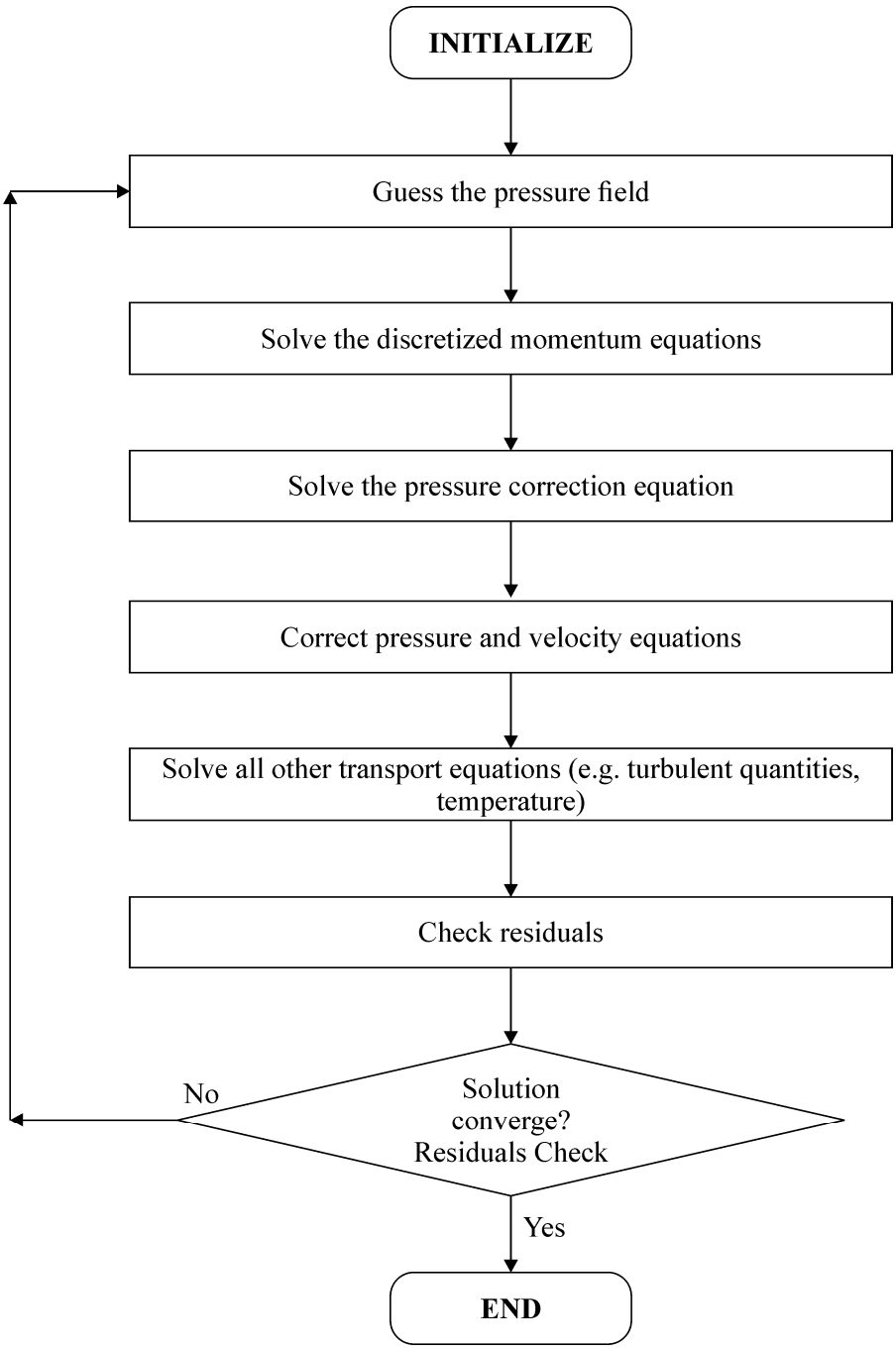

Figure 3.1 SIMPLE method algorithm. *Description of the steps for the implementation of the SIMPLE algorithm*

3.2 Structural Domain

3.2.1 Assumptions

The problem of the static response of a shell describes the structural model for the FSI simulation. The following assumptions related to the structural domain are considered for the development of the FSI study:

1) The mass of the shell per unit area is constant—namely, the shell is homogeneous.
2) The material of the shell is elastic and isotropic.
3) The normal component of the displacement vector, the so-called out of plane deflection *w*, of the shell is small compared with the thickness of the shell. Therefore, the slope of the deflected surface is very small and the square of the slope is a negligible quantity.
4) The applied loads are independent of time. Thus, the inertia effects, caused by the effective forces that results from the acceleration of the shell, are neglected.

3.2.2 Governing Differential Equations

The equation of the structural response of a shell is derived from the Newton's second law of motion. The general vector form that governs the dynamic motion of a shell is given in Eq. 3.13

$$D\overline{\nabla}^4 w + \frac{\partial^2 w}{dt^2} = q$$
$$where \tag{3.13}$$
$$D = \frac{Eh^3}{12(1-\nu^2)}$$

By neglecting the inertia effects due to the acceleration of the body, Eq. 3.13 can be reduced to

$$\vec{\nabla}^4 w = \frac{q}{D} \tag{3.14}$$

Equation 3.14 can be expanded in Cartesian coordinates as follows

$$\frac{\partial^4 w}{\partial x^4} + 2\frac{\partial^4 w}{\partial x^2 \partial y^2} + \frac{\partial^4 w}{\partial y^4} = \frac{q}{D} \tag{3.15}$$

3.2.3 Boundary Conditions

Equation 3.15 is a fourth order linear partial differential equation that requires the specification of boundary conditions to state a well-posed mathematical problem. The clamped condition assigned to the root or bottom edge of the wing requires both the deflection at the edge and the slope in the normal direction *n* to the boundary to be zero. Mathematically, the clamped boundary condition is defined as

$$\begin{gathered} w = 0 \\ and \\ \frac{\partial w}{\partial n} = 0 \end{gathered} \tag{3.16}$$

The deflection and slope at the surrounding edge of the wing is unconstrained. This boundary condition is called a free-edge. Mathematically, the free edge boundary condition is defined as

$$EI\frac{\partial^2 w}{dx^2}=0$$
$$and \tag{3.17}$$
$$\frac{\partial}{\partial x}\left[EI\frac{\partial^2 w}{dx^2}\right]=0$$

3.2.4 Solutions Procedure

The Abaqus/FE is used as the numerical solver to solve the well-posed mathematical problem stated by the governing differential equation in Eq. 3.13 and the respective boundary conditions defined in Eqs. 3.16 and 3.17.

The Abaqus/FE uses the finite element method to generate a set of algebraic linear equations which solutions approximates those from the governing differential equations. The finite element method discretizes or divides the structural domain into a finite set of small pieces called elements. In each finite element, the spatial variation of a field quantity is approximated or described by a spatial function, often a polynomial. The algebraic equations generated from the discretization are solved for the points where the elements are connected—the so-called nodes. The solution of the nodal quantities when combined with the assumed shape function of the field quantity completely determines the spatial variation of the field in that element. Thus, the field quantity is approximated in a piecewise fashion.

CHAPTER 4 RESULTS AND DISCUSSION

4.1 Manufacturing of the Artificial Insect-Sized Wing

4.1.1 Composite Material Artificial Insect-Sized Wing

A sample of the composite artificial insect-sized wing is shown in Fig. 4.1. The millimeter scale of the structure is noticeable when compared against the scale. Measured morphological parameters of the composite material artificial insect-sized wing are presented in Table 4.1. These measurements had a good correlation with those from the reconstructed micro-CT model of the crane fly forewing presented in Table 2.3 and with the line widths assigned to the photomask and discussed in Section 2.4.4. Rectangular cross-sections were observed for the veins of the composite material artificial wing as a result of the limitation and the intrinsic nature of the photolithography technique. The width of the rectangular veins increased with exposure time as a result of the T-topping effect and overexposure.

Table 4.1 Measured morphological parameters from the composite material artificial insect-sized wing

Parameter	Value
Average span length (mm)	13.50
Average chord length (mm)	3.21
Membrane thickness (μm)	12.5
Thick veins width (μm)	126–155
Thin veins width (μm)	105–128
Vein thickness (μm)	100

Figure 4.1 Composite material artificial insect-sized wing sample. *A zoomed-in view of a sample of a composite artificial insect-sized wing.*

4.1.2 Single Material Artificial Insect-Sized Wing

A sample of the single material artificial insect-sized wing is shown in Fig. 4.2. Similar to the composite material wing structure, a good agreement was found between the morphological characteristics and dimensions of the single material artificial wing structure and the crane fly forewing. The venation network presented rectangular cross-sections and the width of the veins increased with exposure time as well. The main difference with respect to the composite material wing was the thickness of the membrane. The thinnest film that could be deposited using SU-8-2050 was 40 μm; therefore, this was the thickness patterned for the membrane layer. The measured morphological parameters of the single material artificial insect-sized wing are presented in Table 4.2.

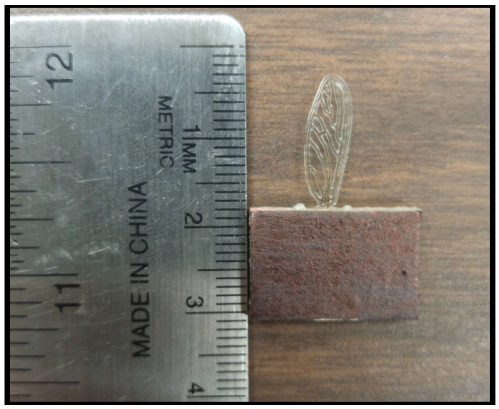

Figure 4.2 Single material artificial insect-sized wing sample. *A zoomed-in view of a sample of a single material artificial insect-sized wing.*

Table 4.2 Measured morphological parameters from the single material artificial insect-sized wing

Parameter	Value
Span length (mm)	13.50
Average chord length (mm)	3.21
Membrane thickness (μm)	40
Thick veins width (μm)	126–155
Thin veins width (μm)	105–128
Vein thickness (μm)	100

4.2 Experimental Modal Analysis of the Artificial Insect-Sized Wing

4.2.1 Sample Preparation

The only preparation required on either the composite material or the single material wing was the application of the speckled pattern. The characteristics of the pattern must follow the guidelines provided in Section 2.5.4. Black spray paint with a matte finish was used to coat a random speckled pattern on the wing surface. The high-contrast required for the black speckles was achieved by backlighting a white area behind the wing. The backlighting technique was

necessary because of the transparency of both the composite material and the single material wing.

4.2.2 Shaker System Setup

A custom-made circular plate was manufactured to attach the wing to the armature of the modal shaker; and thus to transmit the respective base excitation force from the modal shaker to the wing. The circular plate was designed so that it could be attached to the shaker in a way that the excitation force was only transmitted in the out-of-plane direction of the artificial wing. The plate included an extruded square planform to attach the wing to it, threaded holes to fasten the plate to the armature of the shaker, and a threaded hole to mount the accelerometer. The plate was painted in white color to provide the white background that could be backlighted for the high-contrast of the black speckles from the artificial wing.

The artificial wing must be securely clamped at its bottom edge to conduct the vibration tests. The wing was attached to the square planform of the circular plate using 3M Super 77 multipurpose adhesive 3M [104] and an adhesive label Avery 5165 [105]. The circular plate, with the artificial wing attached to it, was secured to the modal shaker. The accelerometer was also mounted to the circular plate to monitor the acceleration levels of the excitation signal. The prepared wing sample mounted on the shaker is shown in Fig. 4.3.

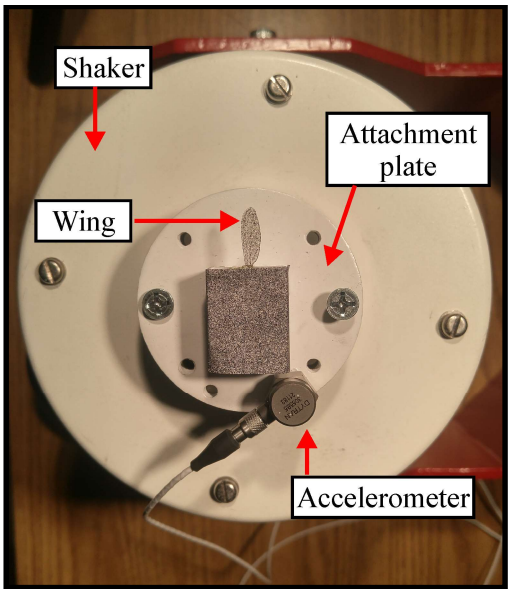

Figure 4.3 Wing sample prepared and mounted on shaker. *The wing sample prepared with the required speckle pattern and attached to the circular plate for the conduction of the vibration experiments.*

The vibration tests were conducted using a closed-loop feedback setup that monitored and adjusted the excitation signal to exhibit the desired acceleration levels. The configuration of the closed-loop feedback setup was made in the following arrangement. The vibration controller generated and monitored the excitation signal. The output channel of the vibration controller was connected to the input channel of the amplifier. The amplifier increased the power of the excitation signal and its output was connected to the modal shaker. The accelerometer mounted on the shaker monitored the acceleration levels of the excitation signal. The output of the accelerometer was connected to the input channel of the controller to adjust the levels of the excitation signal. This feedback process is schematically presented in Fig. 4.4.

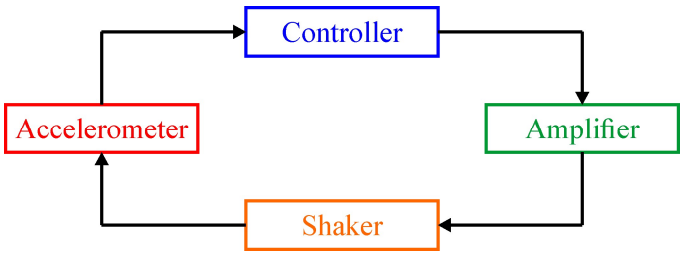

Figure 4.4 Closed-loop feedback control system for the experimental modal analysis setup. *The different components of the vibrational experimental setup were configured as a closed-loop feedback system to provide and monitor the correct excitation levels.*

4.2.3 DIC System Setup and Calibration

The setup of the DIC system started by positioning the two high-speed cameras in the appropriate stereo-triangulation configuration at a distance that filled the view of each camera with the area of interest—namely the surface of the artificial wing. Each camera was mounted on a camera flex mount which were in turn secured to an extruded aluminum profile fixed to a 3-axis adjustable head of the tripod. A Xenoplan 1.9/35 lens [107] with a focal length of 35 mm and an aperture range of 1.9–16f was attached to each camera. The cameras were positioned fairly symmetrical about the specimen to keep the magnification level consistent [83]. The stereo-angle was set to approximately 20 deg with respect to the wing specimen following the recommendation of stereo-angle configurations for 35 mm lenses [83].

After establishing the correct stereo-triangulation configuration, two diffusive lamps were positioned to illuminate and backlight the specimen. Both the composite material and the single material artificial wings were transparent structures; therefore, it was necessary to illuminate the white background behind the wings to achieve the high-contrast speckled pattern—this technique is known as backlighting. It was also considered to avoid both projecting a shadow behind the wing and locating the lamps near the head of the cameras. The former would decrease the

contrast of the acquired images; whereas, the latter would introduce refracted heat waves on the captured images; both would negatively interfere with the DIC process.

The next step consisted on adjusting the focus and the brightness on the image from each camera. The objective was to have an image that was as sharp and bright as possible without showing any saturation. It was also desired to have a broad range over which the focus of each camera was sharp—commonly referred in optical terminology as a large depth of field—in case there were large out-of-plane deformations during the conduction of the test. In general, setting the focus and the brightness of the image for each camera was an iterative process that depended on adjusting the aperture of the lenses and the exposure time of the camera sensors. These in turn were determined for a specific stereo-triangulation configuration and location of the diffusive lights; thus, no specific parameter is reported in this investigation. However, the guidelines to have a sharp and bright image with a large depth of field where the speckled pattern can be well-distinct are provided below. To begin, the aperture of the lens for each camera was completely opened to the lowest f-number; this caused the depth of field to become very small and to exaggerate any out-of-focus area of the artificial wing. The focus on each camera was adjusted with this opened aperture. Once a sharp image was achieved, the aperture of the lens was returned to the appropriate configuration for the conduction of the test. It was important to monitor the effects on the brightness of the image when setting the suitable aperture. Closing the aperture to a larger f-number increased the depth of field at an expense of a decrease of the brightness of the image. To have a large depth of field with a small aperture, the brightness of the image was also adjusted by varying the exposure time—this parameter determined the amount of time that the sensor of the camera gathered light before reading a new image [83] and it was controlled using the VIC-Snap [99] software. Longer exposure times involved a brighter image

at the expense that blur could be present if significant out-of-plane motion occurred. As mentioned previously, the aperture and the exposure time were iteratively determined to optimize the focus and brightness for a particular test.

The last step of the setup of the DIC system was to perform the calibration. As explained in Section 2.5.4, the purpose of the calibration was to determine the intrinsic and extrinsic parameters of the cameras. The calibration procedure required using a calibration target with coded markers. The selected calibration target must have the approximate size of the area of interest, namely the size of the artificial wing. For this application, a customized calibration target (pitch: 1.780 mm, number of dots: 9 by 9, offset in X and Y: 4, length in X: 3, and length in Y: 4) was used. To capture the calibration images, the circular plate was removed temporary from the armature of the shaker. The calibration target was then held at approximately the same location of the area of interest and 20 to 50 images of the calibration target were acquired at different views rotated about all the three axes using the VIC-Snap software. It was necessary to make sure that all the three coded markers of the calibration target were visible in every image. The calibration images were then loaded on the VIC-3D software [100] to proceed with the calibration. Once the calibration was successfully completed, the circular plate with the attached wing was mounted again to the shaker. At this moment, the position of the cameras and the focus and aperture settings of the lenses must not and were not altered.

4.2.4 Sampling Acquisition Settings

The Shannon sampling theorem states that the sampling frequency should be at least twice the highest frequency contained in the signal. This highest frequency in the signal is commonly referred as the Nyquist frequency or the maximum resolvable frequency of the

frequency spectrum. For a sampling frequency f_s and a Nyquist frequency $f_{Nyquist}$, the Shannon sampling theorem can be mathematically expressed in Eq. 4.1.

$$f_s \geq 2 f_{Nyquist} \tag{4.1}$$

The sampling acquisition settings of the deformation response of the artificial wing were determined based on the Nyquist frequency (maximum resolvable frequency) required on the frequency spectrum. The deformation response of the artificial wing was sampled at either 2000 Hz, 3000 Hz, or 4000 Hz to analyze frequency spectra below 1000 Hz, 1500 Hz, or 2000 Hz, respectively. It was also imperative to capture the images with the highest resolution possible to have a large number of pixels within each subset. This would ultimately lead to a better tracking of the subsets by the DIC algorithm. The total recording time was automatically determined by selecting the sampling rate and image resolution; nonetheless, a total recording time of at least 2 s was sought. The sampling acquisition settings for the conduction of the vibration experiments were defined on the VIC-Snap software and are summarized in Table 4.3.

Table 4.3 DIC acquisition settings for the conduction of the vibration experiments

Parameter	**Required values for a Nyquist frequency of**		
	1000 Hz	**1500 Hz**	**2000 Hz**
Sampling rate (Hz)	2000	3000	4000
Resolution (pixels × pixels)	512 × 512	512 × 256	512 × 256
Recording time (s)	2.046	2.728	2.046
Number of samples per camera	4092	8184	8184

4.2.5 Shaker Excitation Signal Settings

A random excitation signal was selected for this investigation. The random vibration signal consisted of a continuous spectrum of frequencies within a specified bandwidth. The

advantage of implementing a random signal was that all the frequency components within the specified bandwidth were excited at the same time. This provided a more realistic representation of the operational conditions experienced during insect flight. Furthermore, the duration of the experimental tests decreased significantly.

The bandwidth of the excitation signal was the first parameter to be defined. The random signal must not include frequency content higher that the Nyquist frequency; otherwise, a phenomenon in which the higher frequencies appeared as lower frequencies in the spectrum could happen. This phenomenon is known as aliasing and must be avoided. The random excitation signal was defined to have a resolution of 2.5 Hz. The resolution represented the difference between two adjacent frequency points. Lastly, the test was run at a level of 10 dB. The parameters that defined the random excitation signal are summarized in Table 4.4.

Table 4.4 Random excitation signal parameters

Parameter	**Required values for a Nyquist frequency of**		
	1000 Hz	**1500 Hz**	**2000 Hz**
Bandwidth lower frequency (Hz)	10	10	10
Bandwidth upper frequency (Hz)	1000	1500	2000
Kurtosis	3	3	3
Resolution (Hz)	2.5	2.5	2.5
Frequency lines	400	600	800
Run scheduled level (dB)	10	10	10

Following, a test spectrum profile must be defined. A power spectral density (PSD) function is generally used to represent the test spectrum of a random signal. The PSD plot describes the mean square acceleration of the random signal at any frequency. The PSD profile uses real-time acquisition measurements—in this case from the accelerometer—to generate a statistical approximation of the motion experienced at the control point on the specimen. A

Gaussian probability distribution with a kurtosis of 3 was defined for this statistical approximation. Specifying a Gaussian or normal distribution guaranteed that the majority of the random acceleration data points at any frequency were closely centered to the mean value.

The PSD function of the random signal implemented in this investigation is defined in Table 4.5 and plotted in Fig. 4.5. Each segment from the PSD function was defined from the frequency of the selected breakpoint up to the frequency of the next breakpoint in the table. The reference column described the reference value for the specified PSD segment. If the type specified was "level", the reference was defined in acceleration units per Hertz (g^2/Hz). Otherwise, if the type was "slope", the reference was defined in decibels per octave (dB/oct) and represented the slope of a straight line segment between the current frequency and the next higher frequency. The parameters shown in Table 4.5 were experimentally determined based on realistic acceleration values that the artificial wing structure would experience. Furthermore, high acceleration levels that would damage the integrity of either the artificial wing or the modal shaker were avoided.

Table 4.5 Breakpoint table for the PSD function of the random excitation signal

Breakpoint frequency (Hz)	**Reference**	**Unit**	**Type**
10	1	dB/Oct	Slope
40	0.00025	g^2/Hz	Level
350	0.00025	g^2/Hz	Level
2000	-1	dB/Oct	Slope

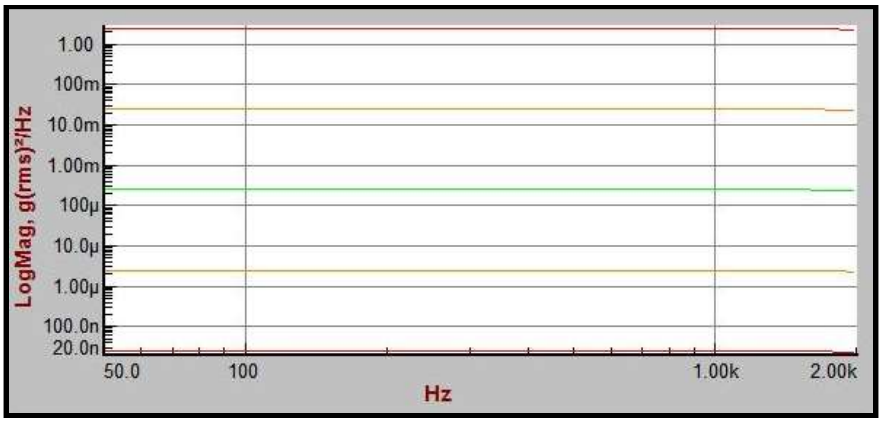

Figure 4.5 PSD profile of the random excitation signal. *Plot of the PSD function showing the different acceleration levels for the random excitation signal.*

4.2.6 FFT Calculations

The full-field deformation response of the artificial wing to the broadband random excitation force was captured using the VIC-Snap software and postprocessed using the VIC-3D software. Four data blocks were acquired throughout the base excitation for averaging purposes. Rigid body motion effects were removed from the area of interest of the artificial wing using the VIC-3D software.

The time-varying out-of-plane deformation and velocity data at seven different points, hereafter referred as measurement points, located along the surface of the wing was extracted to calculate the respective FFTs. The measurement points were randomly selected at distant coordinates relative to each other along the surface of the artificial wing. Their approximate locations are shown in Fig. 4.6. Selecting and analyzing a higher number of measurement points decreased the probabilities of omitting the identification of a natural frequency by selecting a nodal point from the mode shape of that particular frequency.

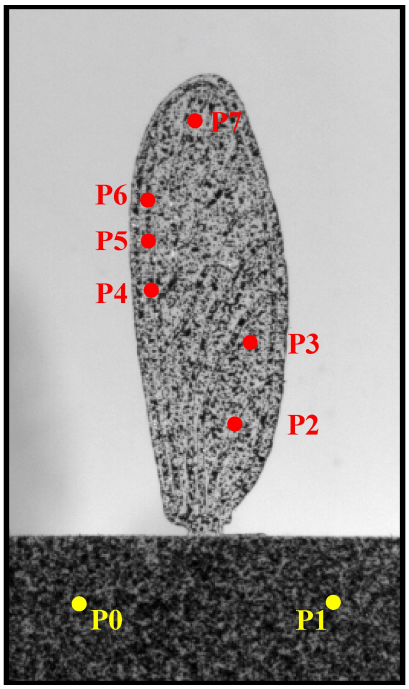

Figure 4.6 Measurement points for the calculation of the FFT. *The time-varying out-of-plane displacement data was extracted from random measurement points located along the surface of the artificial wing for the calculation of the FFT.*

The extracted time-varying out-of-plane deformation and velocity data was preprocessed before calculating the corresponding FFTs. The FFT is an algorithm designed to calculate the spectrum of a signal with a number of discrete samples which is a power of 2. Hence, it was required to pad with zeros the out-of-plane deformation and velocity data extracted from each measurement point until the number of samples was equal to a power of 2. Furthermore, the deformation response was random and nonperiodic; thus, a Hanning window was applied to the displacement data to compel with the periodicity requirement for the calculation of the FFT. The Hanning window artificially forced the deformation data block to be exactly zero at the beginning and at the end of the time block to make it appeared periodic to the analyzer.

A linear averaging method was implemented to attenuate the noise of the FFT. This method consisted on computing the FFT for each of the four time-varying displacement data

blocks acquired during the base excitation. The FFTs were then averaged to reduce the noise of the spectrum and to be able to better identify the frequency components of higher magnitude. The averaged FFT was smoothed using a Savitzky-Golay filter with a 4^{th} polynomial model. The smoothing of the averaged FFT further allowed an easier identification of the resonant peaks from the frequency spectrum.

4.2.7 Results

A parametric study was conducted to determine the effects of exposure time on the natural frequencies of the artificial wing. Four different batches were manufactured for the composite material and the single material wing with different exposure times. The experimental natural frequencies for the composite material wing and the single material wing are shown in Tables 4.6 and 4.7, respectively. The FFTs of the out-of-plane deformation and velocity data for the measurement points of the composite material wing and the single material wing are shown in Figs. 4.7–4.14 and Figs. 4.15–4.22, respectively. The Fourier analysis showed that the natural frequency increased with exposure time. This behavior was expected for two reasons. First, the cross-link reactions of the SU-8 were further completed as the exposure time to UV light increased; thus, the homogeneity and stiffness of the pattern increased. Second, the venation pattern was broadened with exposure time as a result of the T-topping effect; this added bending and torsional resistance as the moment area of inertia of the veins increased.

The first three mode shapes of the artificial wing are shown in Fig. 4.23. Both the composite material and the single material wing exhibited the same mode shapes. The first mode shape showed a bending deformation response with the location of the maximum displacement at the tip of the wing. This behavior was expected due to the inherent stiffness variation along the spanwise *y*-direction of the wing provided by the venation pattern with varying line widths. The

second mode shape showed the location of the maximum distortion at approximately 3/4th of the spanwise *y*-direction of both the leading and the trailing edge of the wing with a nodal line extending along the central *y*-axis of the wing. This torsional structural response identified less rigid regions at both the leading and the trailing edges of the wing. The third mode shape displayed the maximum displacement at the tip of the wing with two nodal lines extending in the chordwise *x*-direction—one developed near the root of the wing and the second one developed near the center of the spanwise *y*-direction. The third mode shape further confirmed the relative flexibility of both the leading edge and the tip of the artificial insect-sized wing as seen in the wing structure of different insect species [22].

Table 4.6 Experimental natural frequencies for the composite material wing

Sample ID	**UV exposure time (s)**	**Natural frequency (Hz)**		
		First	**Second**	**Third**
Composite 1	180	99.12	450.20	562.50
Composite 2	420	123.04	565.43	636.72
Composite 3	600	125.97	632.32	760.74
Composite 4	780	175.97	672.72	1001.02

Table 4.7 Experimental natural frequencies for the single material wing

Sample ID	**UV exposure time (s)**	**Natural frequency (Hz)**		
		First	**Second**	**Third**
Single 1	180	146.48	745.12	849.12
Single 2	420	156.73	753.24	979.02
Single 3	600	157.71	772.34	1065.31
Single 4	780	191.40	796.41	1225.20

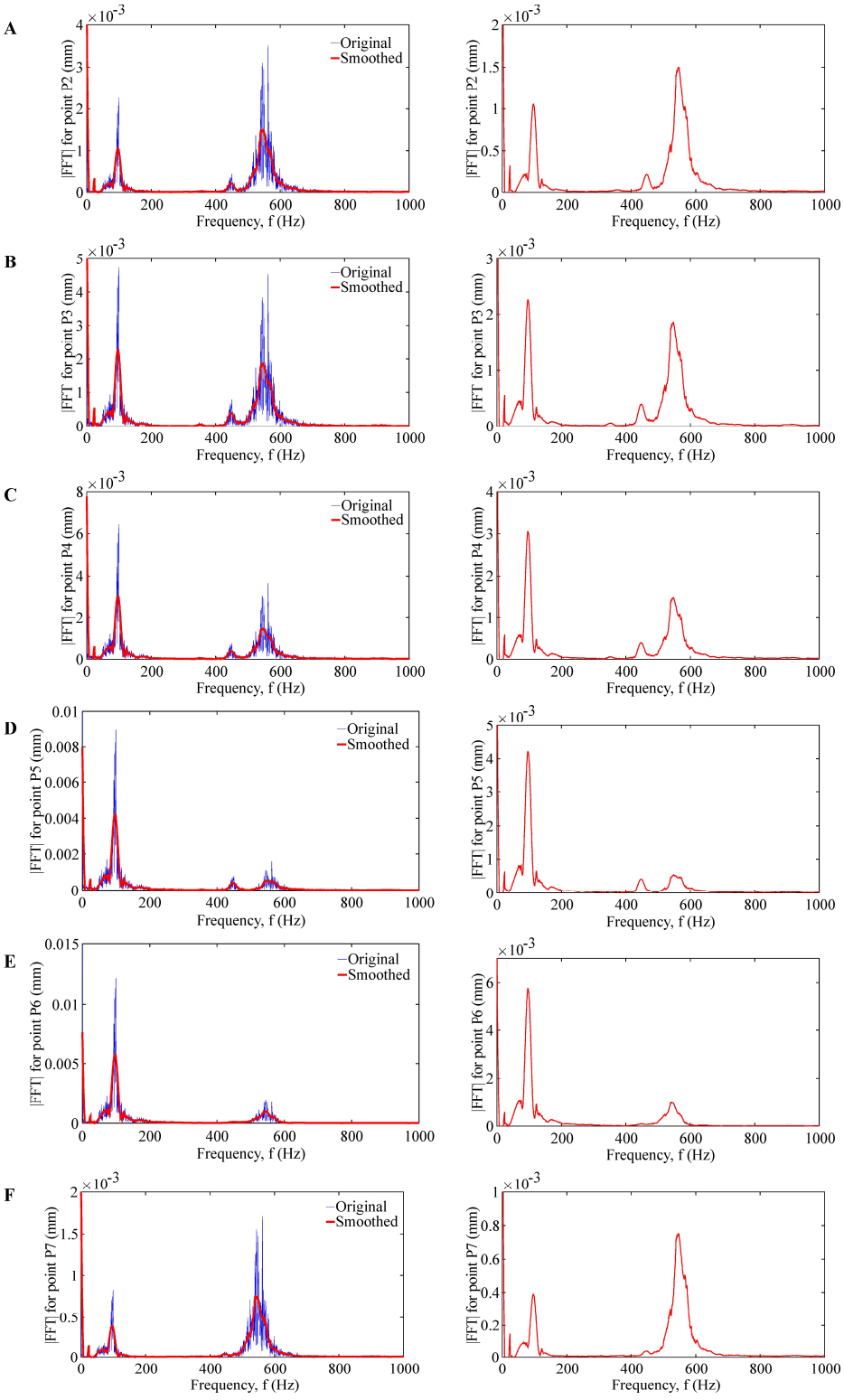

Figure 4.7 FFT of the displacement response of the Composite-1 artificial wing. *On the left column both the FFT averaged from the four runs with the respective smoothed FFT and on the right column only the smoothed FFT for the out-of-plane displacement response of (A) point P2, (B) point P3, (C) point P4, (D) point P5, (E) point P6, and (F) point P7 of the Composite-1 artificial wing.*

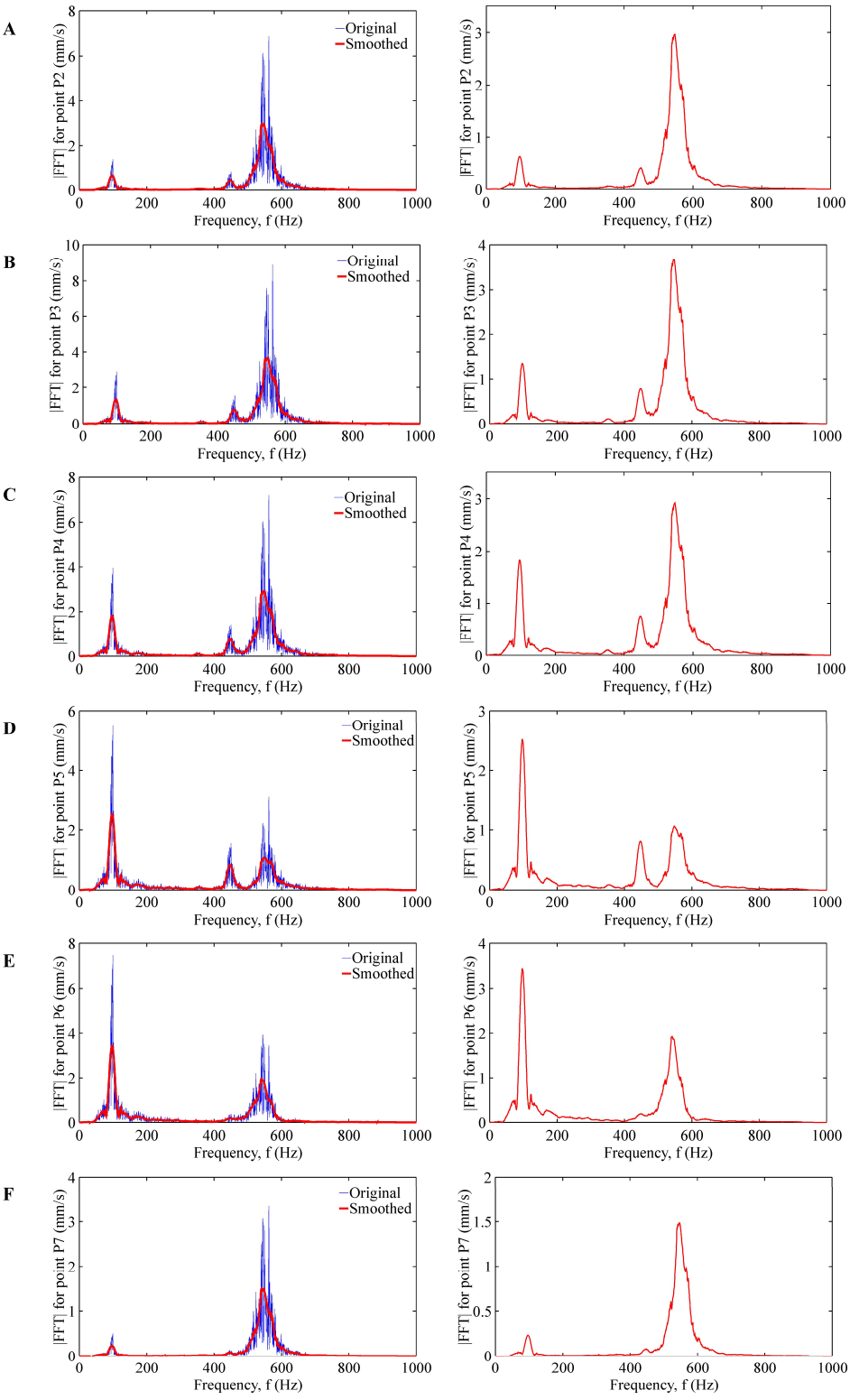

Figure 4.8 FFT of the velocity response of the Composite-1 artificial wing. *On the left column both the FFT averaged from the four runs with the respective smoothed FFT and on the right column only the smoothed FFT for the velocity response of (A) point P2, (B) point P3, (C) point P4, (D) point P5, (E) point P6, and (F) point P7 of the Composite-1 artificial wing.*

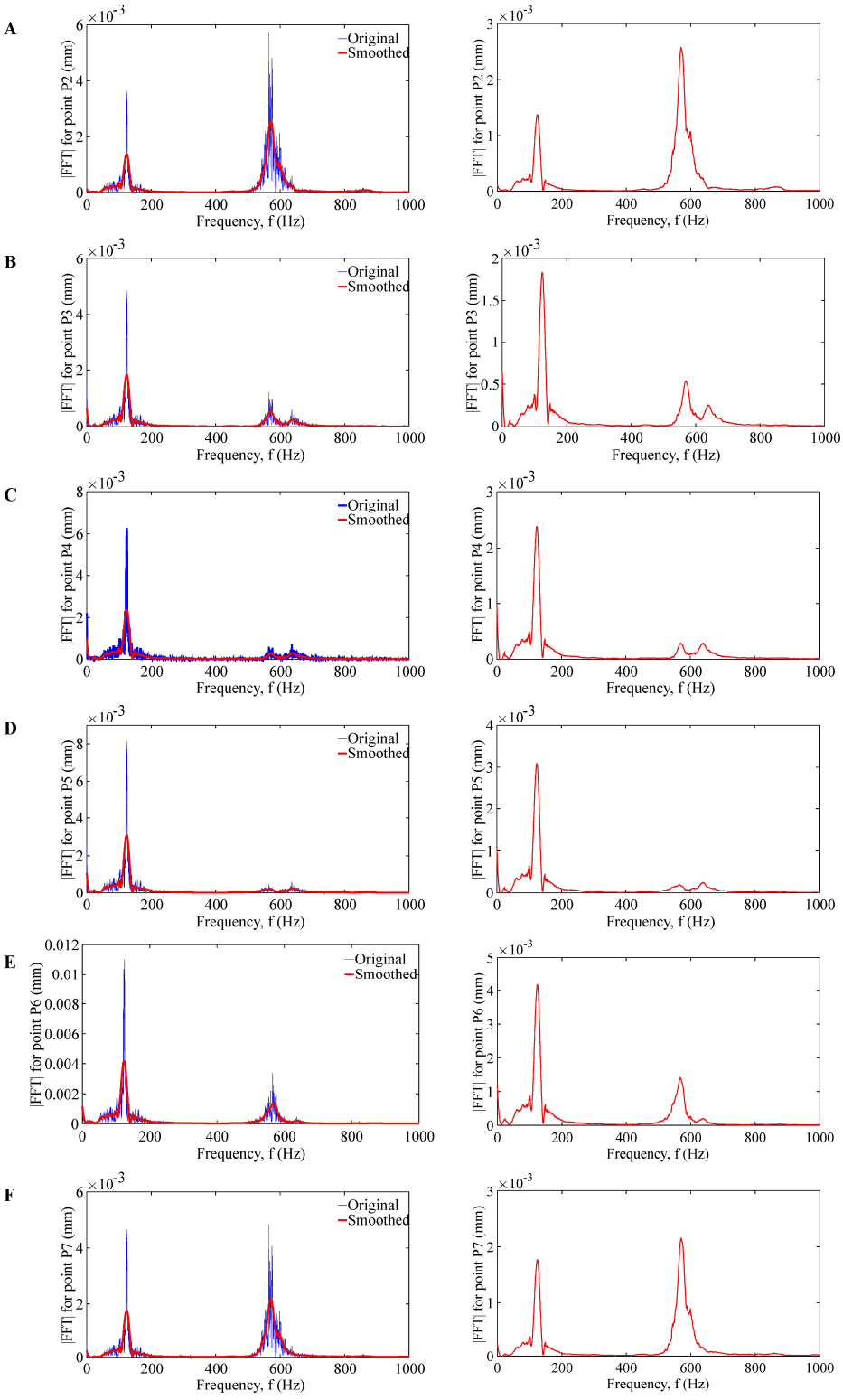

Figure 4.9 FFT of the displacement response of the Composite-2 artificial wing. *On the left column both the FFT averaged from the four runs with the respective smoothed FFT and on the right column only the smoothed FFT for the out-of-plane displacement response of (A) point P2, (B) point P3, (C) point P4, (D) point P5, (E) point P6, and (F) point P7 of the Composite-2 artificial wing.*

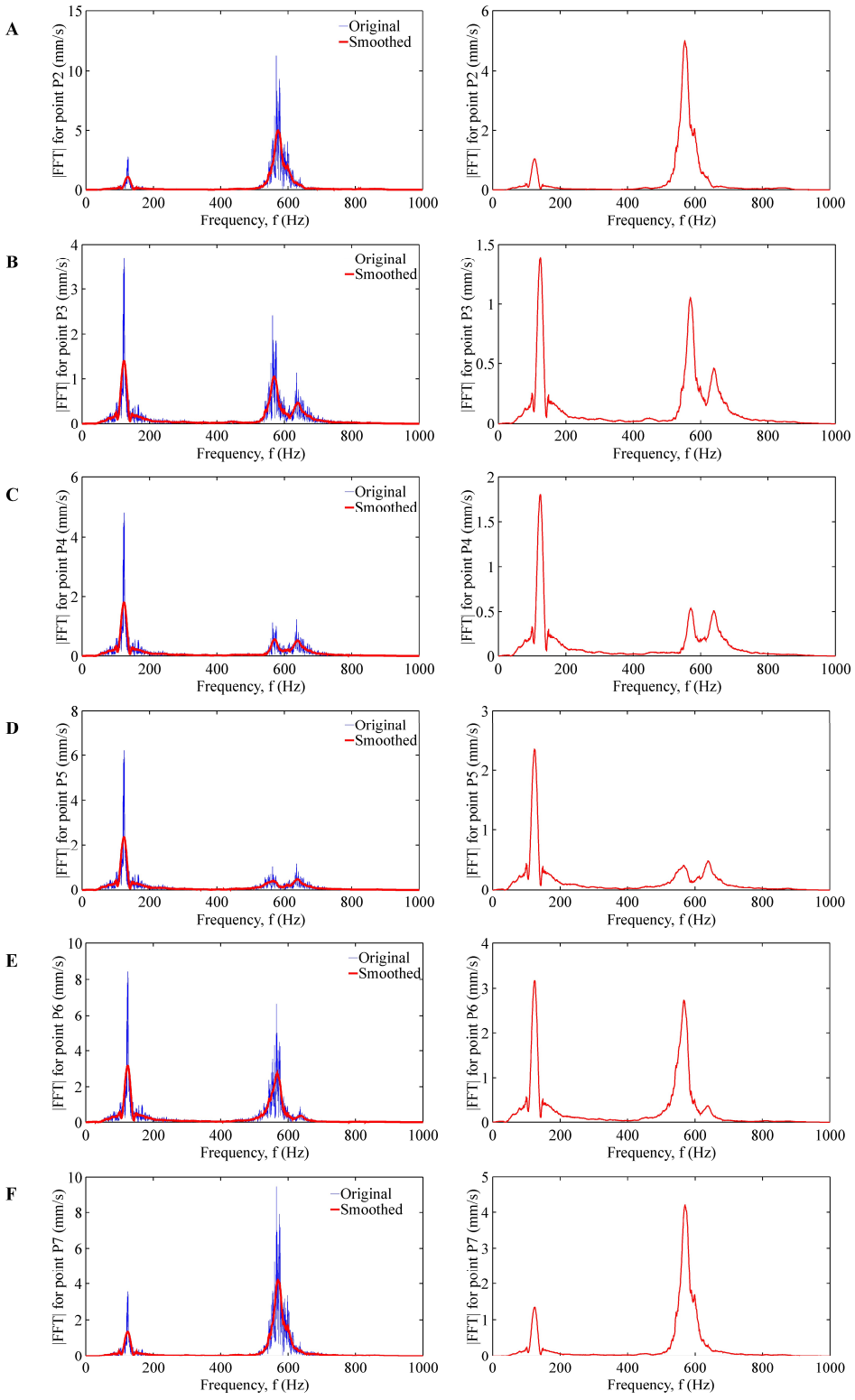

Figure 4.10 FFT of the velocity response of the Composite-2 artificial wing. *On the left column both the FFT averaged from the four runs with the respective smoothed FFT and on the right column only the smoothed FFT for the velocity response of (A) point P2, (B) point P3, (C) point P4, (D) point P5, (E) point P6, and (F) point P7 of the Composite-2 artificial wing.*

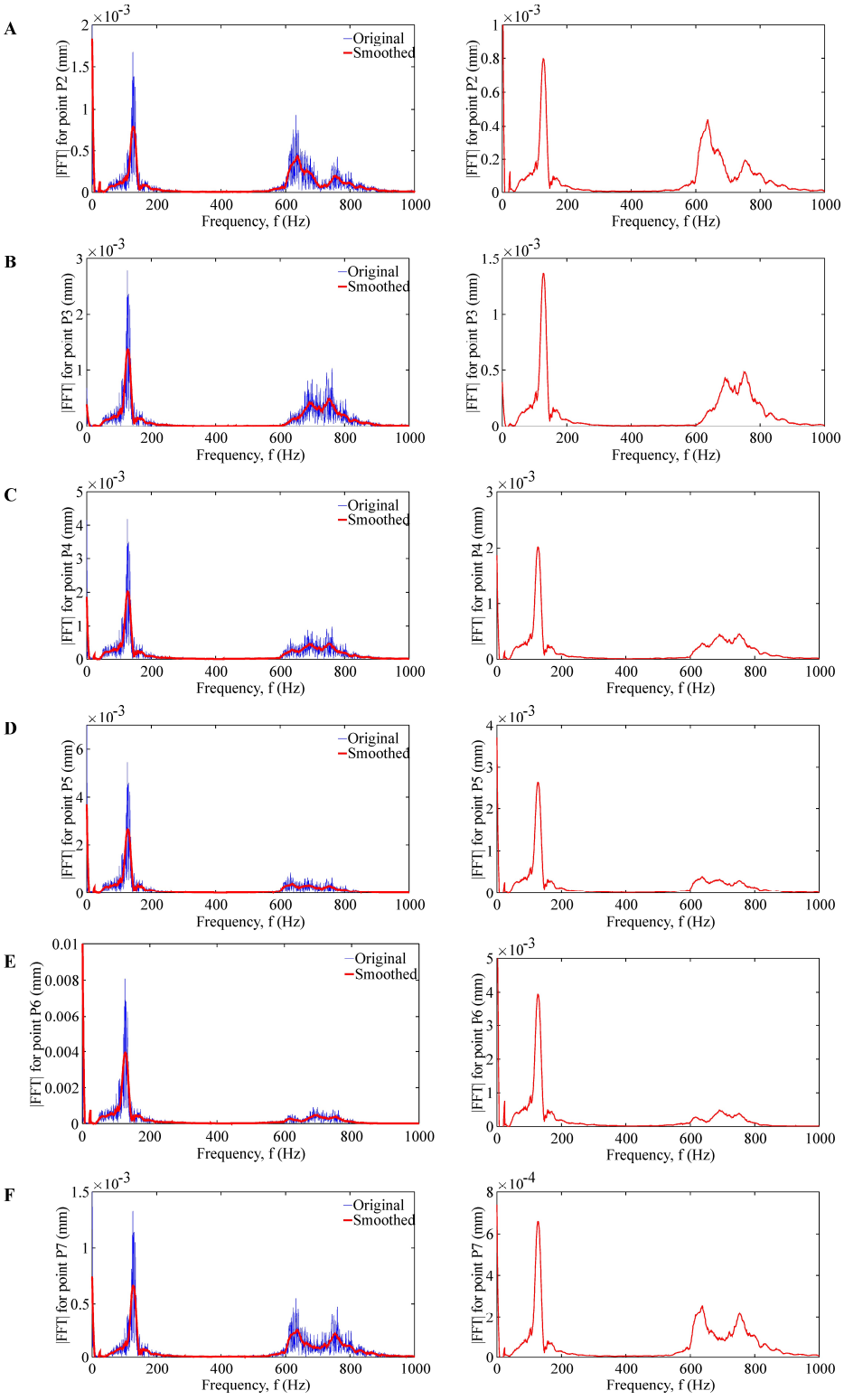

Figure 4.11 FFT of the displacement response of the Composite-3 artificial wing. *On the left column both the FFT averaged from the four runs with the respective smoothed FFT and on the right column only the smoothed FFT for the out-of-plane displacement response of (A) point P2, (B) point P3, (C) point P4, (D) point P5, (E) point P6, and (F) point P7 of the Composite-3 artificial wing.*

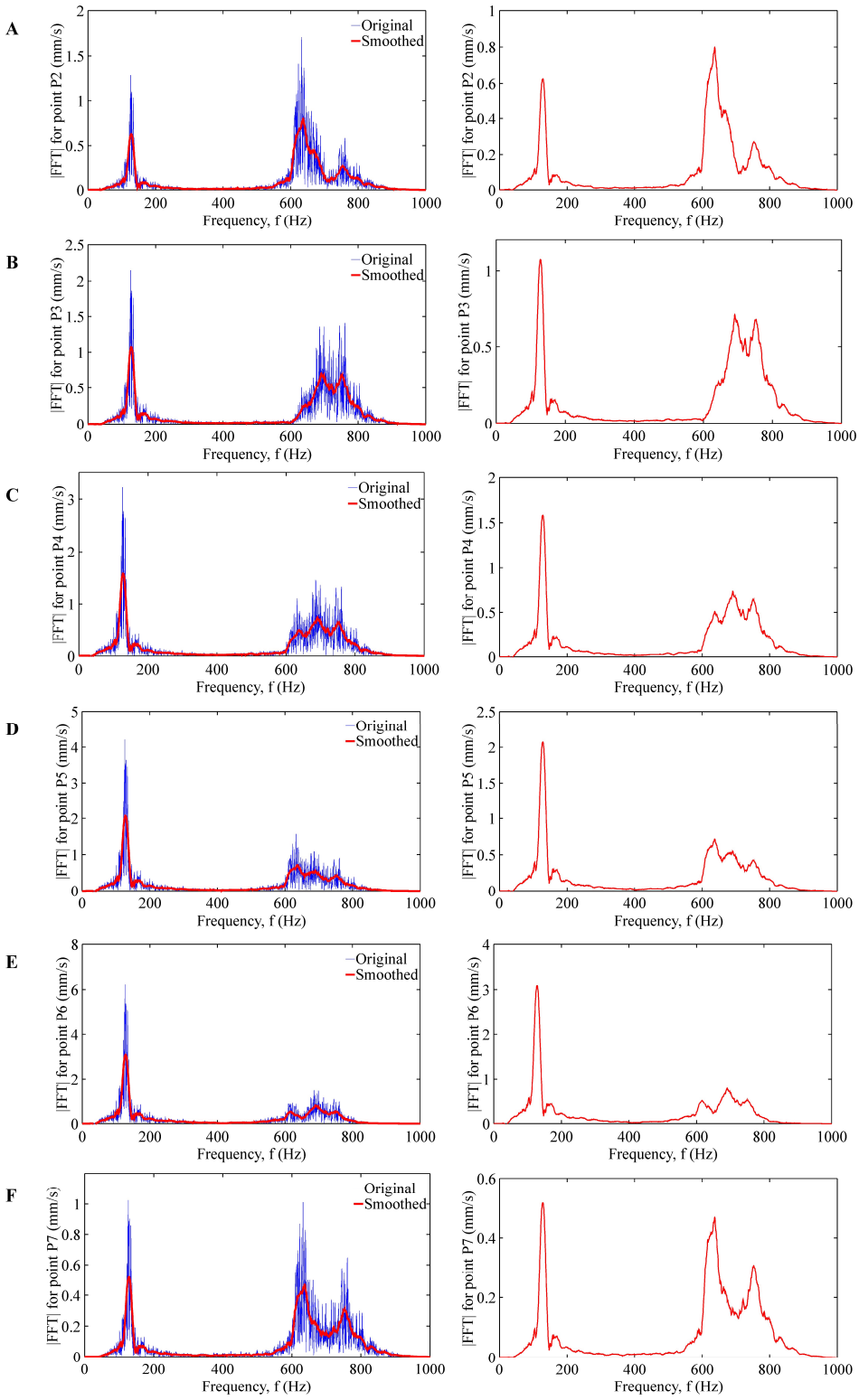

Figure 4.12 FFT of the velocity response of the Composite-3 artificial wing. *On the left column both the FFT averaged from the four runs with the respective smoothed FFT and on the right column only the smoothed FFT for the velocity response of (A) point P2, (B) point P3, (C) point P4, (D) point P5, (E) point P6, and (F) point P7 of the Composite-3 artificial wing.*

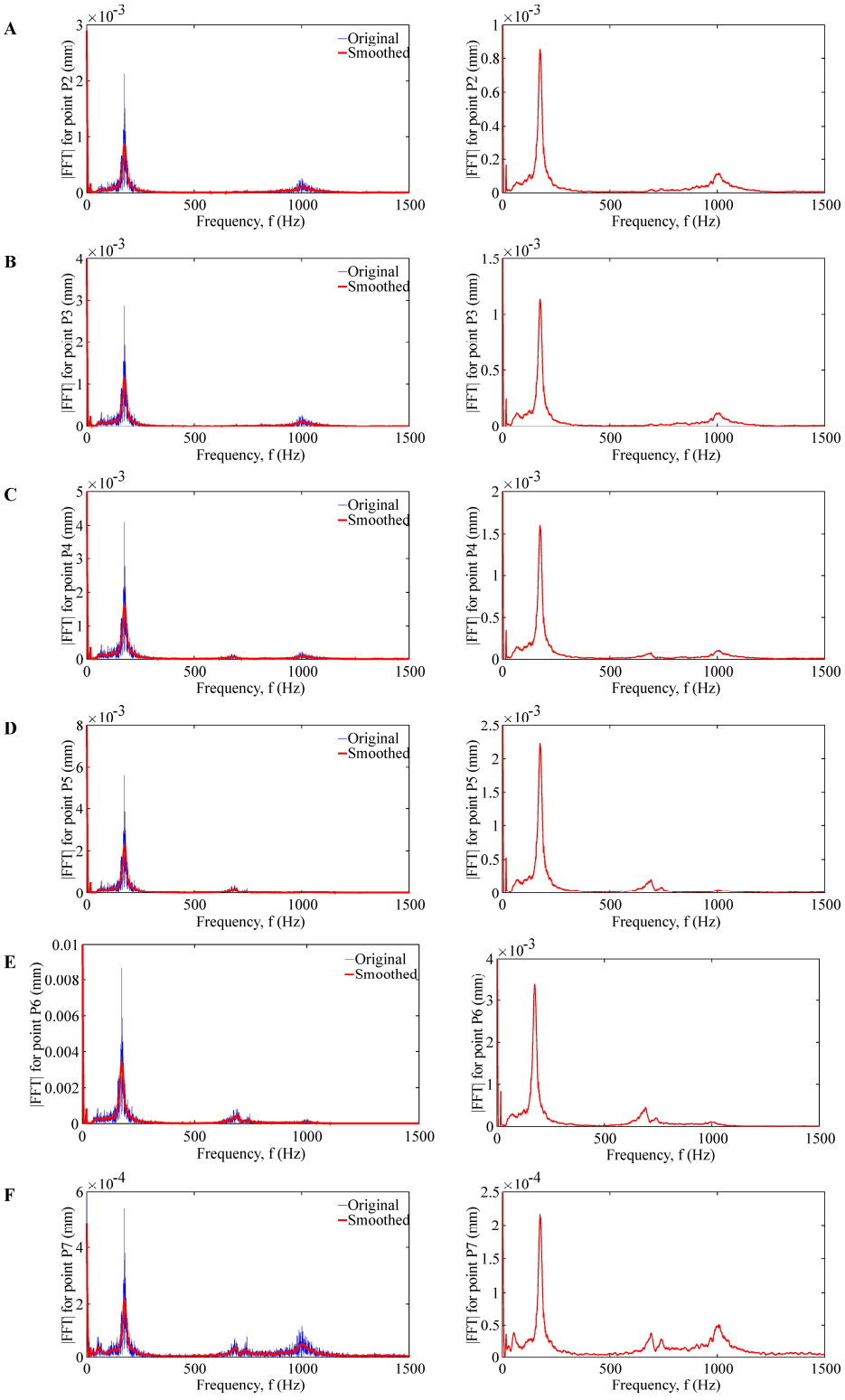

Figure 4.13 FFT of the displacement response of the Composite-4 artificial wing. *On the left column both the FFT averaged from the four runs with the respective smoothed FFT and on the right column only the smoothed FFT for the out-of-plane displacement response of (A) point P2, (B) point P3, (C) point P4, (D) point P5, (E) point P6, and (F) point P7 of the Composite-4 artificial wing.*

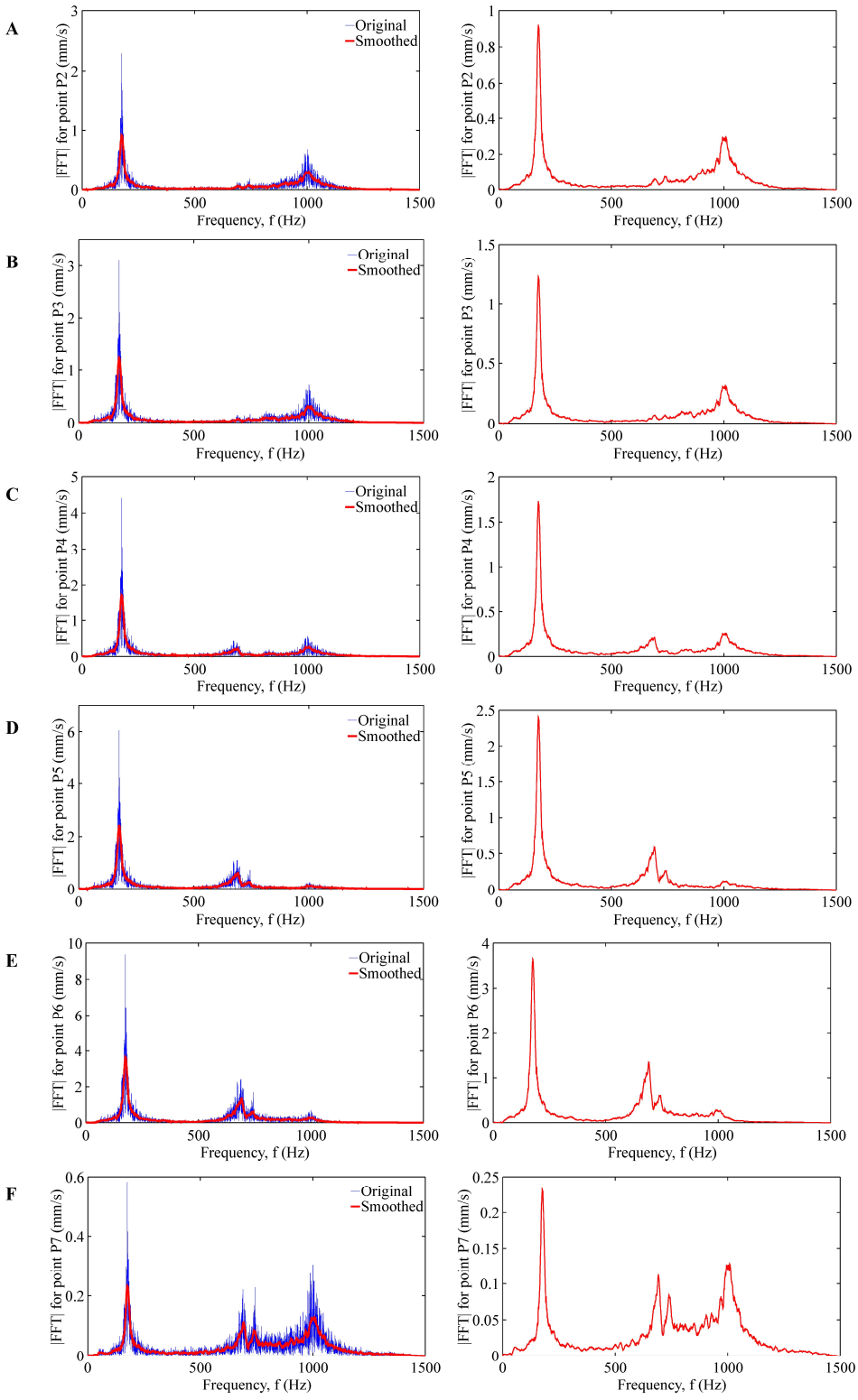

Figure 4.14 FFT of the velocity response of the Composite-4 artificial wing. *On the left column both the FFT averaged from the four runs with the respective smoothed FFT and on the right column only the smoothed FFT for the velocity response of (A) point P2, (B) point P3, (C) point P4, (D) point P5, (E) point P6, and (F) point P7 of the Composite-4 artificial wing.*

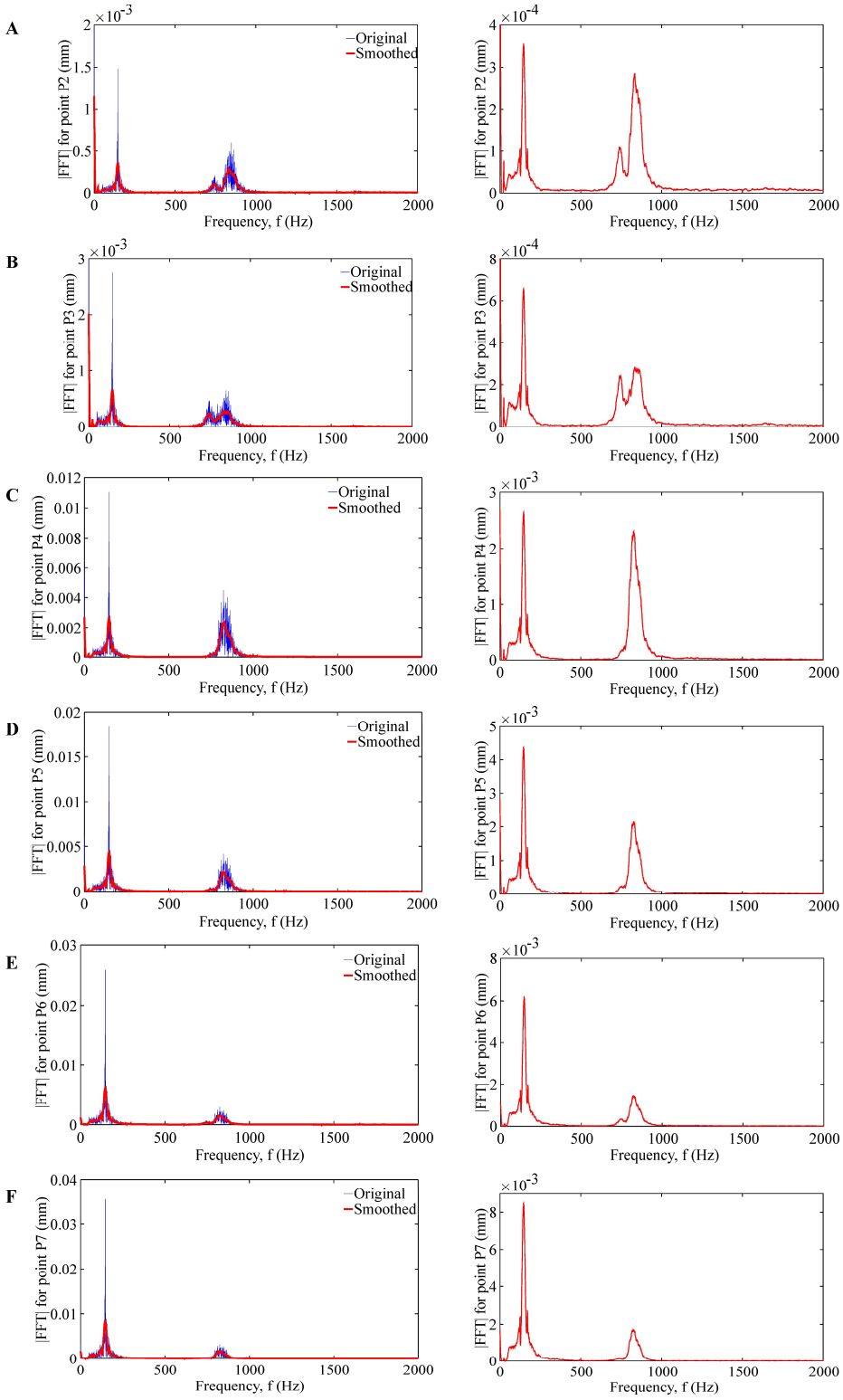

Figure 4.15 FFT of the displacement response of the Single-1 artificial wing. *On the left column both the FFT averaged from the four runs with the respective smoothed FFT and on the right column only the smoothed FFT for the out-of-plane displacement response of (A) point P2, (B) point P3, (C) point P4, (D) point P5, (E) point P6, and (F) point P7 of the Single-1 artificial wing.*

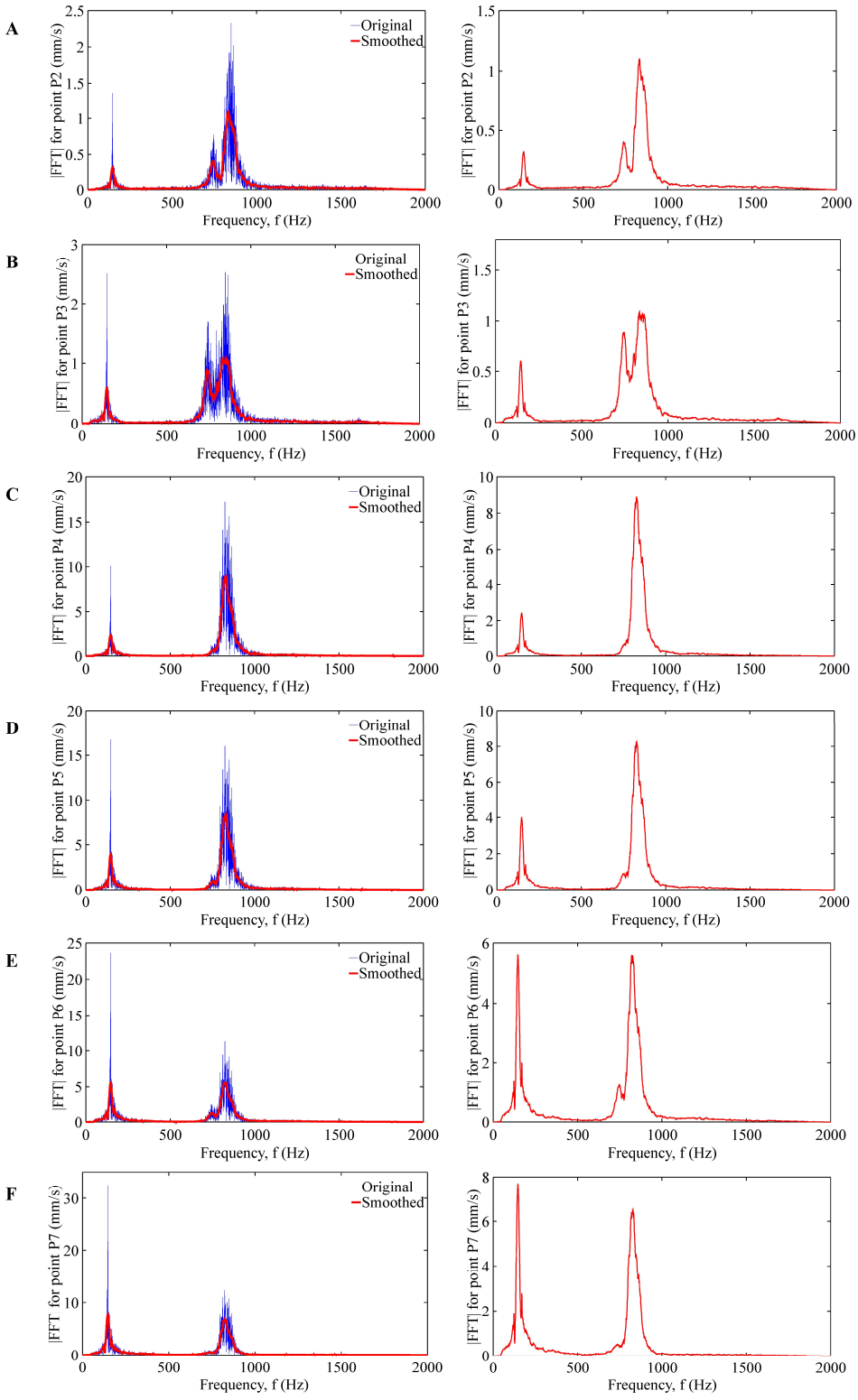

Figure 4.16 FFT of the velocity response of the Single-1 artificial wing. *On the left column both the FFT averaged from the four runs with the respective smoothed FFT and on the right column only the smoothed FFT for the velocity response of (A) point P2, (B) point P3, (C) point P4, (D) point P5, (E) point P6, and (F) point P7 of the Single-1 artificial wing.*

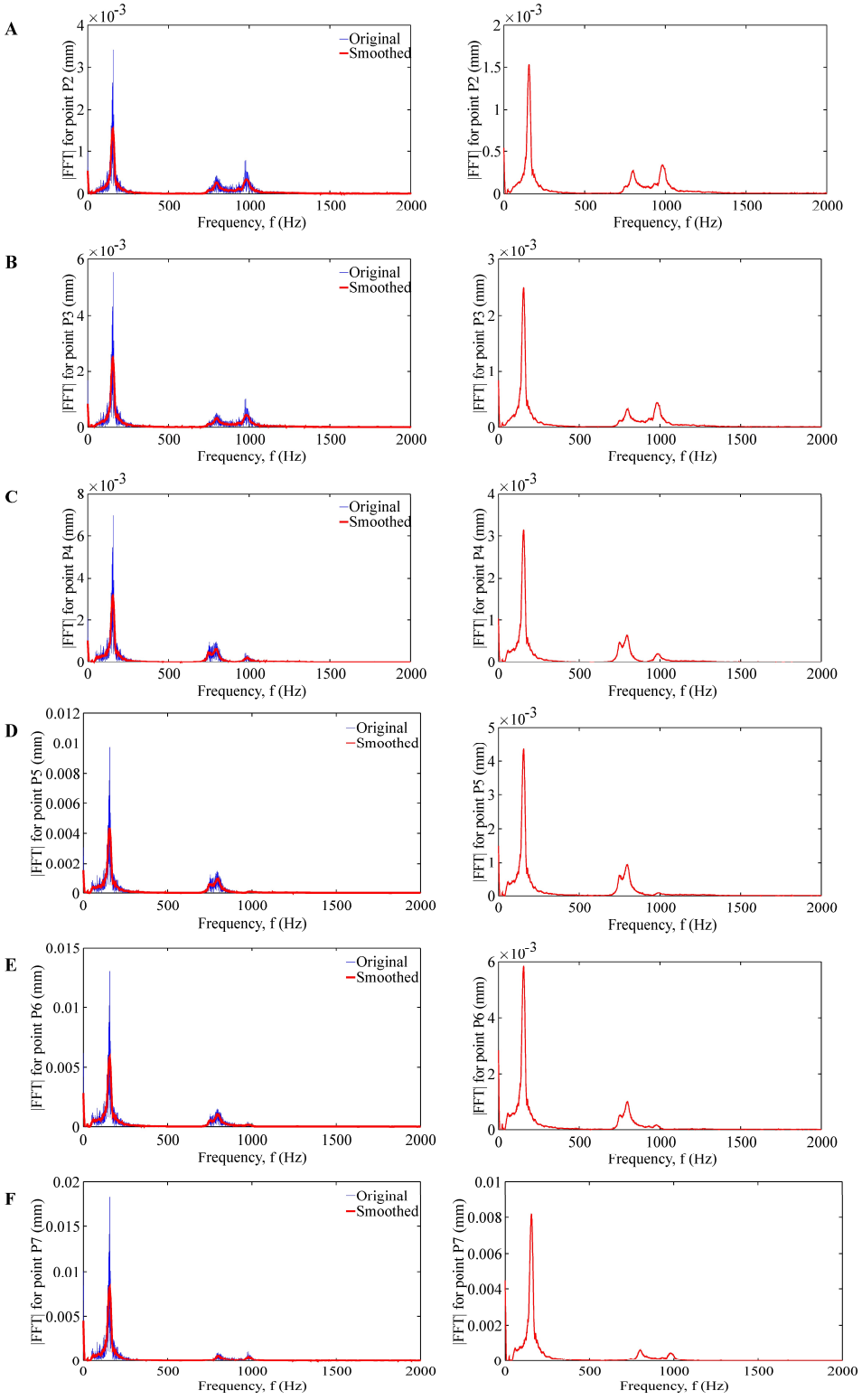

Figure 4.17 FFT of the displacement response of the Single-2 artificial wing. *On the left column both the FFT averaged from the four runs with the respective smoothed FFT and on the right column only the smoothed FFT for the out-of-plane displacement response of (A) point P2, (B) point P3, (C) point P4, (D) point P5, (E) point P6, and (F) point P7 of the Single-2 artificial wing.*

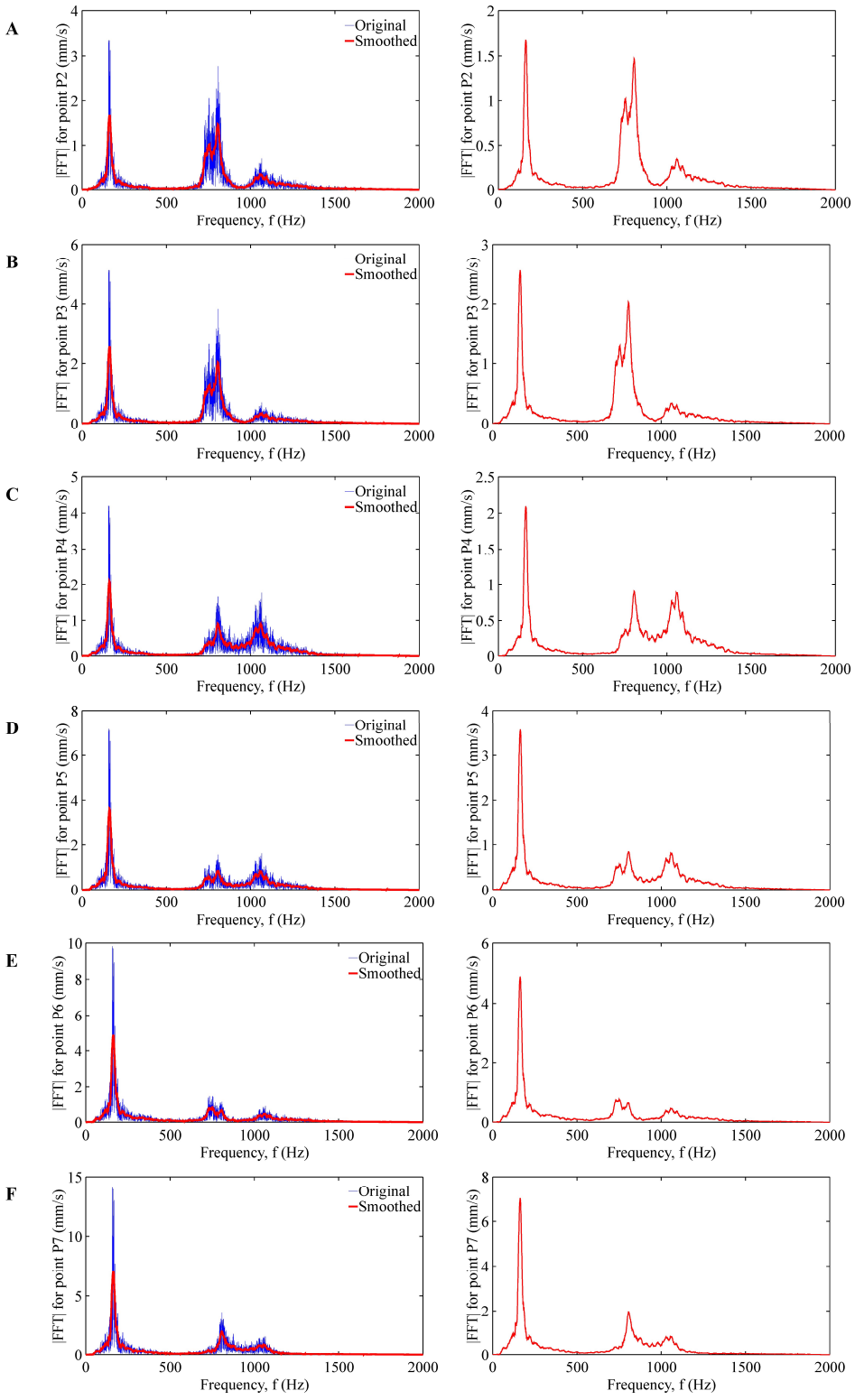

Figure 4.18 FFT of the velocity response of the Single-2 artificial wing. *On the left column both the FFT averaged from the four runs with the respective smoothed FFT and on the right column only the smoothed FFT for the velocity response of (A) point P2, (B) point P3, (C) point P4, (D) point P5, (E) point P6, and (F) point P7 of the Single-2 artificial wing.*

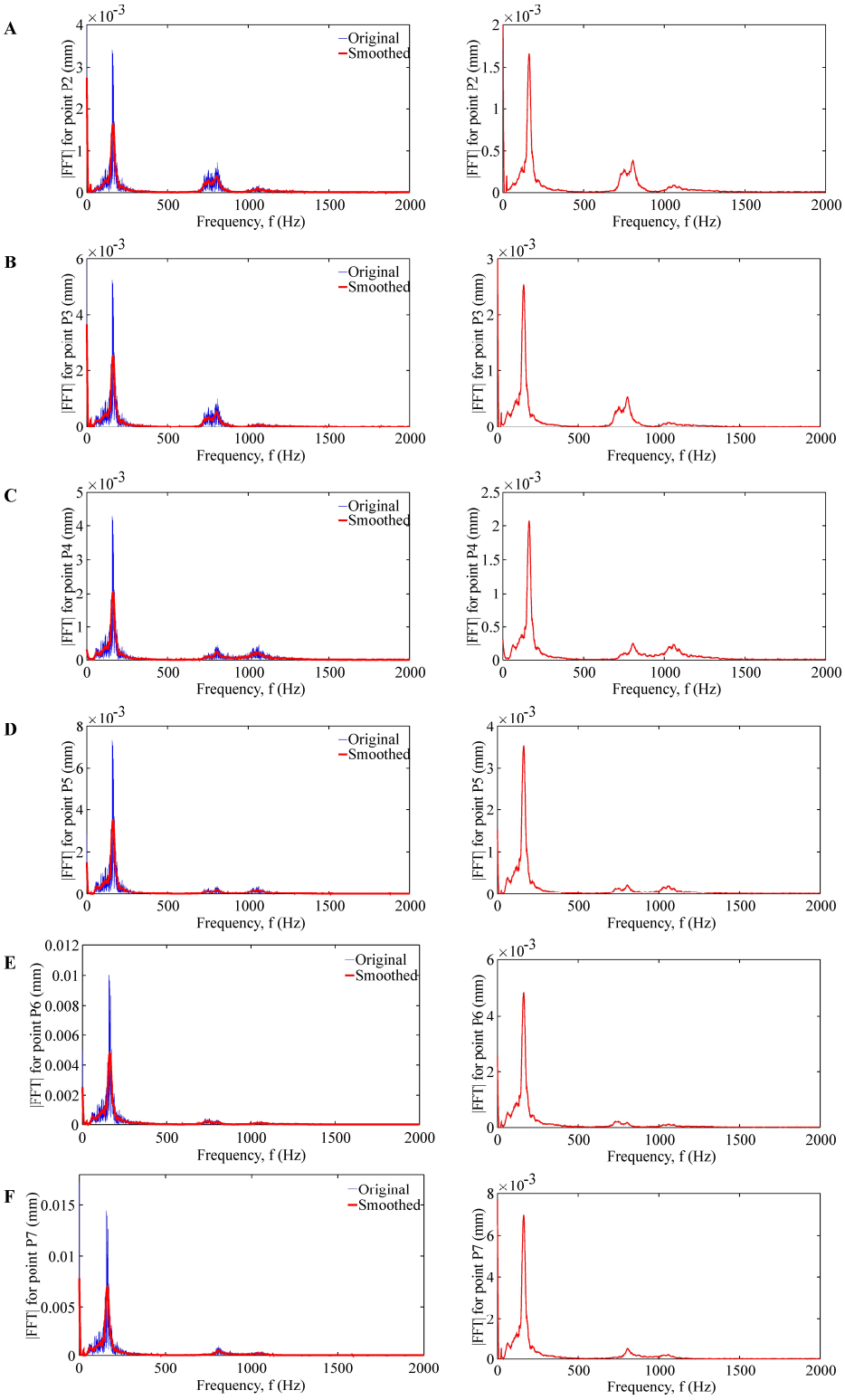

Figure 4.19 FFT of the displacement response of the Single-3 artificial wing. *On the left column both the FFT averaged from the four runs with the respective smoothed FFT and on the right column only the smoothed FFT for the out-of-plane displacement response of (A) point P2, (B) point P3, (C) point P4, (D) point P5, (E) point P6, and (F) point P7 of the Single-3 artificial wing.*

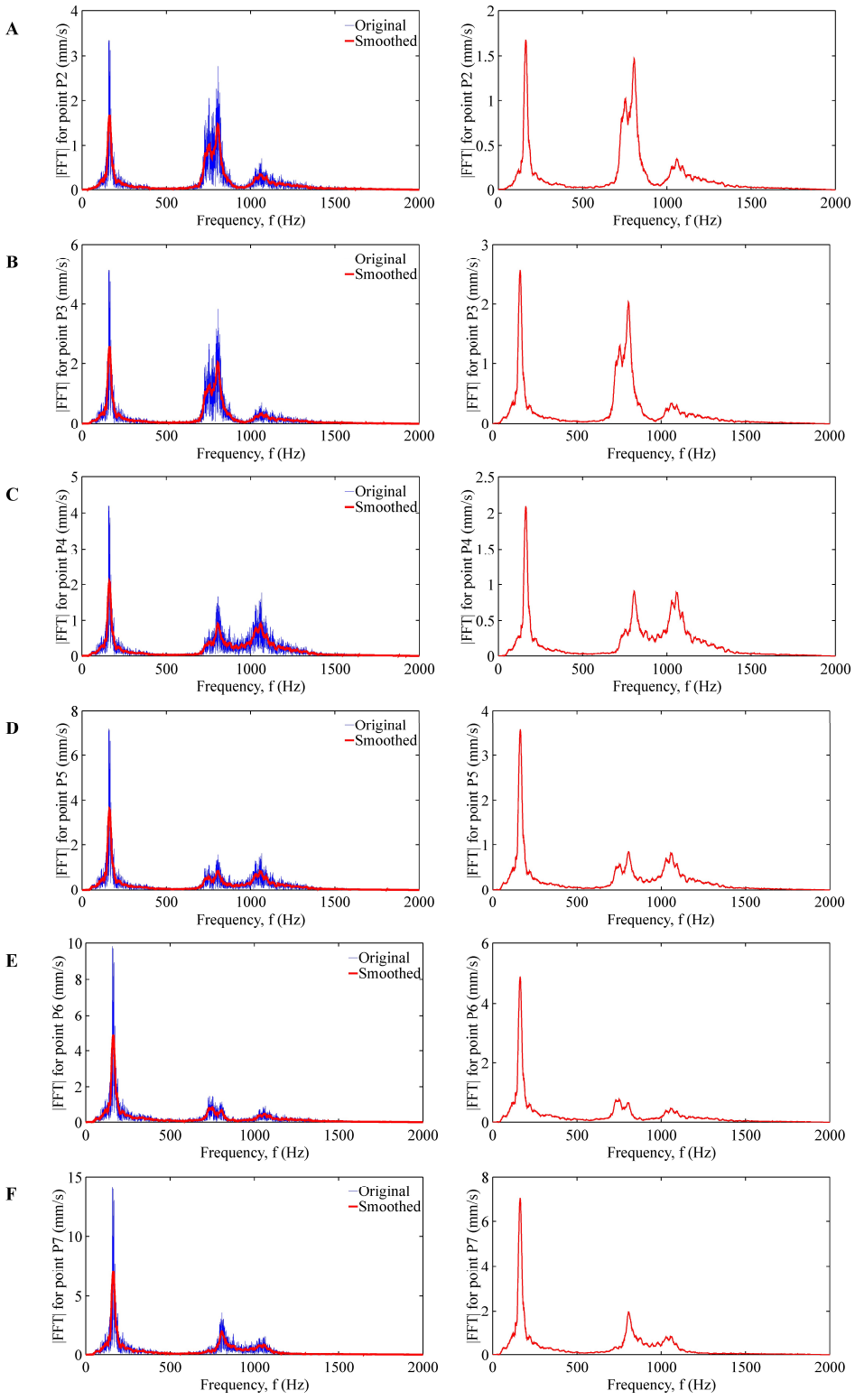

Figure 4.20 FFT of the velocity response of the Single-3 artificial wing. *On the left column both the FFT averaged from the four runs with the respective smoothed FFT and on the right column only the smoothed FFT for the velocity response of (A) point P2, (B) point P3, (C) point P4, (D) point P5, (E) point P6, and (F) point P7 of the Single-3 artificial wing.*

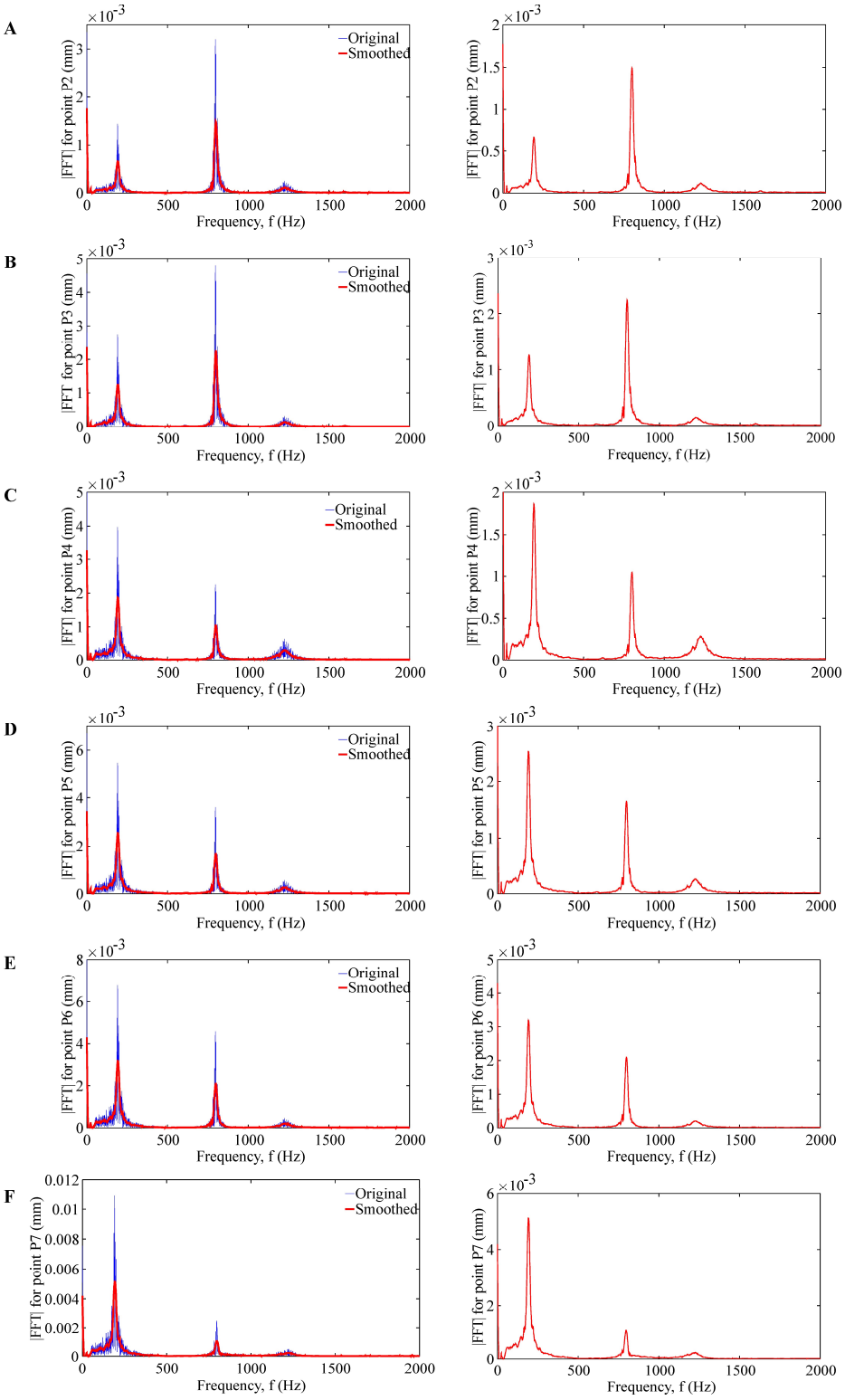

Figure 4.21 FFT of the displacement response of the Single-4 artificial wing. *On the left column both the FFT averaged from the four runs with the respective smoothed FFT and on the right column only the smoothed FFT for the out-of-plane displacement response of (A) point P2, (B) point P3, (C) point P4, (D) point P5, (E) point P6, and (F) point P7 of the Single-4 artificial wing.*

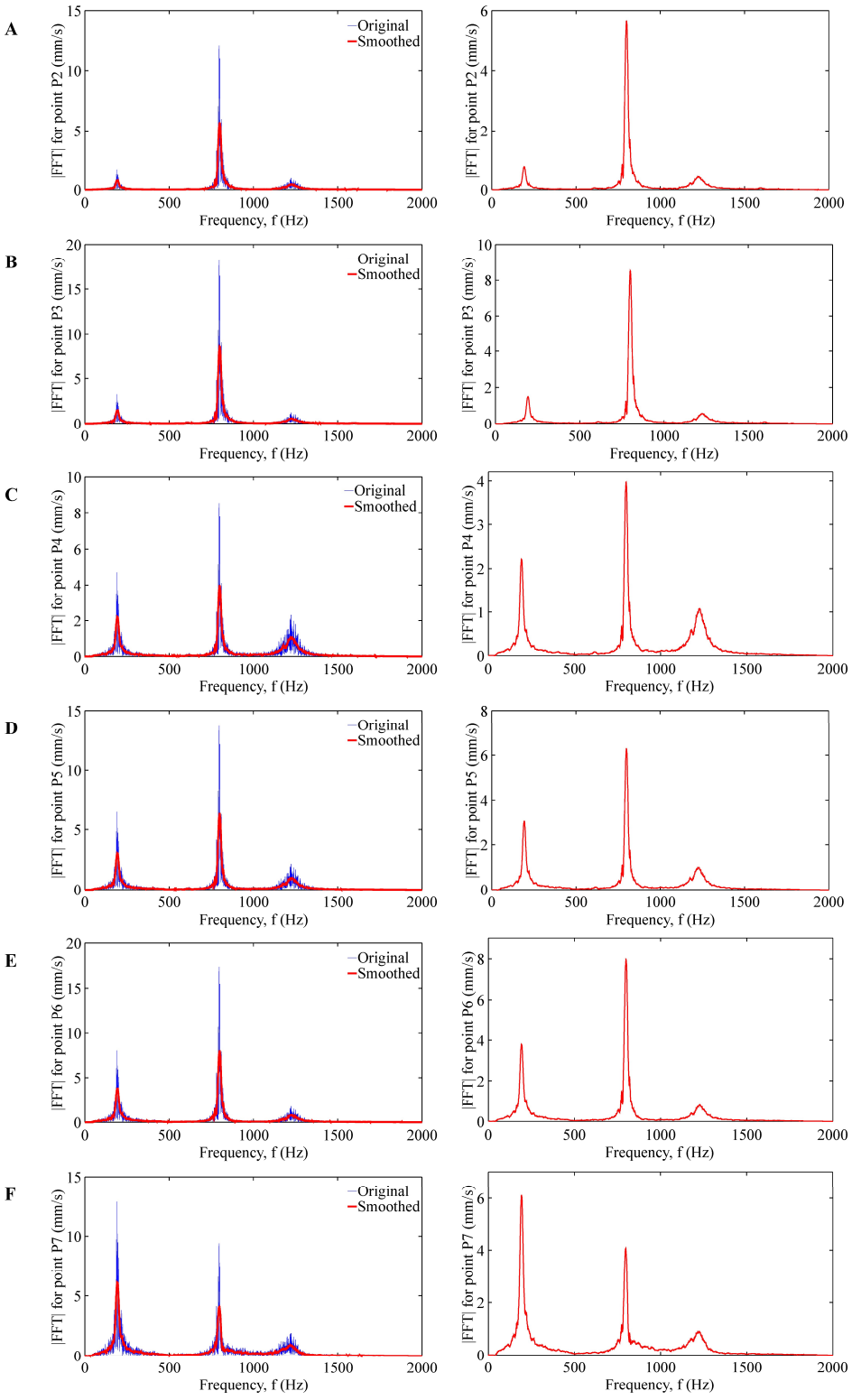

Figure 4.22 FFT of the velocity response of the Single-4 artificial wing. *On the left column both the FFT averaged from the four runs with the respective smoothed FFT and on the right column only the smoothed FFT for the velocity response of (A) point P2, (B) point P3, (C) point P4, (D) point P5, (E) point P6, and (F) point P7 of the Single-4 artificial wing.*

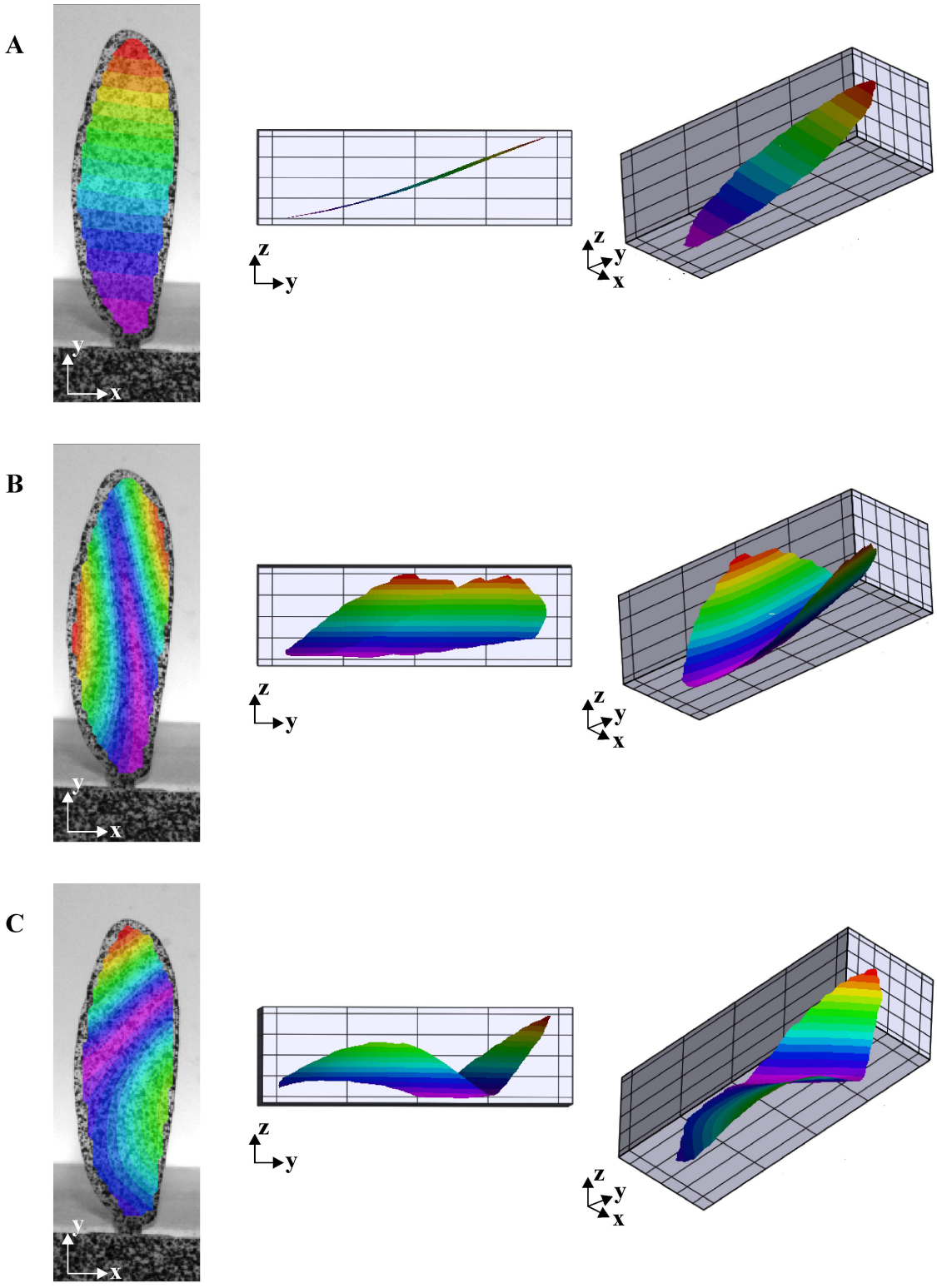

Figure 4.23 Experimental mode shapes of the artificial insect-sized wing. *(A) First (B) second, and (C) third mode shape of the artificial insect-sized wing.*

4.3 Experimental Aerodynamic Response of the Artificial Insect-Sized Wing

4.3.1 Sample Preparation

The sample preparation required to conduct the aerodynamic experiments was basically the same one from the vibration experiments discussed in Section 4.2.1. Black spray paint with a matte finish was used to coat the speckled pattern. Several pieces of white cardboard were attached to the wall of the test section of the wind tunnel to create a white background that could be backlighted by the diffusive lights; and thus, to achieve the high-contrast speckled pattern.

The artificial wing must be securely clamped at its bottom edge to conduct the aerodynamic tests. For this purpose, two pieces of high-density cardboard were clamped together at the bottom the rectangular segment of the wing using a multipurpose adhesive Super 77 from 3M [104].

4.3.2 Wind-Tunnel Setup

The setup of the wind tunnel was fairly simple. The setup started by fixing the model-positioning system to the wall of the test section. The sting balance was then attached to the model-positioning system. Both fixtures had to be securely fixed so that no rigid body motion was induced on the artificial wing during the aerodynamic loading.

A custom-made socket that fitted directly into the sting balance was designed to fix the artificial wing on the wind tunnel. The socket included two lateral extruded plates with a rectangular cavity where the clamped section of the wing was press-fitted. Figure 4.24 illustrates the custom-made socket mounted on the sting balance inside the wind tunnel. The custom-made socket was mounted on the sting balance. Next, the artificial wing was press-fitted into the

rectangular slot of the socket. The prepared wing sample fixed inside the wind tunnel is shown in Fig. 4.24.

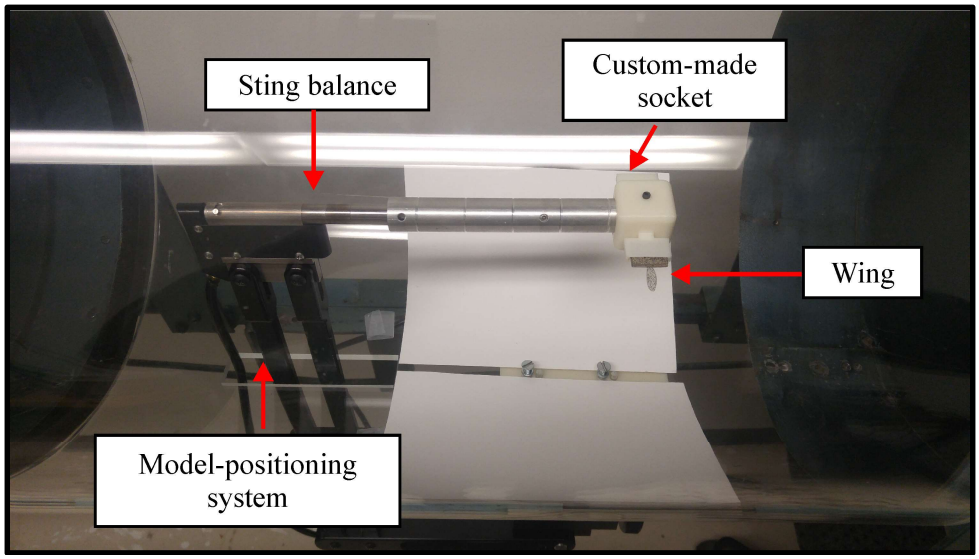

Figure 4.24 Wing sample prepared and fixed inside the wind tunnel. *The wing sample prepared with the required speckle pattern and fixed inside the wind tunnel using the custom-made socket for the conduction of the aerodynamic experiments.*

The freestream velocity inside the wind-tunnel was adjusted by controlling the rotational speed of the DC motor that drove the fan. The freestream velocity as a function of the rotational speed of the motor was measured using the air velocity transducer prior the conduction of any experiment with the artificial wing,

4.3.3 DIC System Setup and Calibration

The steps for setting up the DIC system for the aerodynamic experiments were essentially the same as those from the vibration experiments discussed in Section 4.2.3. At first, the 35 mm lenses were attached to the cameras. The cameras were then positioned just outside the test section of the wind tunnel at a stereo-angle of 20 deg with respect to the artificial wing sample.

The focus, aperture, and exposure time of the cameras were adjusted following the same guidelines described in Section 4.2.3 for the vibration experiments. The calibration was done in the same procedure, except that a different calibration target was used because the field of view was larger since the cameras were located farther away from the artificial wing. Specifically, the 1-inch calibration target (pitch: 1.340 mm, number of dots: 9 by 9, offset in X and Y:3, length in X:3, and length in Y:4) was used.

4.3.4 Sampling Acquisition Settings

The main factor that determined the DIC acquisition settings for the aerodynamic experiments was having enough recording time to capture the wing structural response to aerodynamic loading from the unloaded stage (no freestream velocity) to the loaded stage (steady freestream velocity). Therefore, a slower sampling rate than the one used for the vibration experiments was used. It was also desired to capture the images with the highest resolution possible for a better tracking of the subsets of the images during the correlation stage. The DIC acquisition settings for the aerodynamic experiments are summarized in Table 4.8.

Table 4.8 DIC acquisition settings for the conduction of the aerodynamic experiments

Parameter	Value
Sampling rate (Hz)	250
Resolution (pixels × pixels)	512 × 512
Recording time (s)	16.368
Number of samples per camera	4092

4.3.5 Results

The structural aerodynamic response of the artificial insect-sized wing was determined at different freestream velocities and angles of attack. The deformation response was acquired

using the VIC-snap software and postprocessed using the VIC-3D system. The dimensionless parameter of Reynolds number was used as the reference for establishing the aerodynamic conditions within the regimen of an insect flight.

The variation of the deformation distribution along the span of the composite material artificial wing for different Reynolds number at 5 deg angle of attack is shown in Fig. 4.25. The deformation changes nonlinearly from the root of the wing to the tip. Furthermore, as expected, the magnitude of the deformation increases with Reynolds number. This behavior was observed in the single material artificial wing as well.

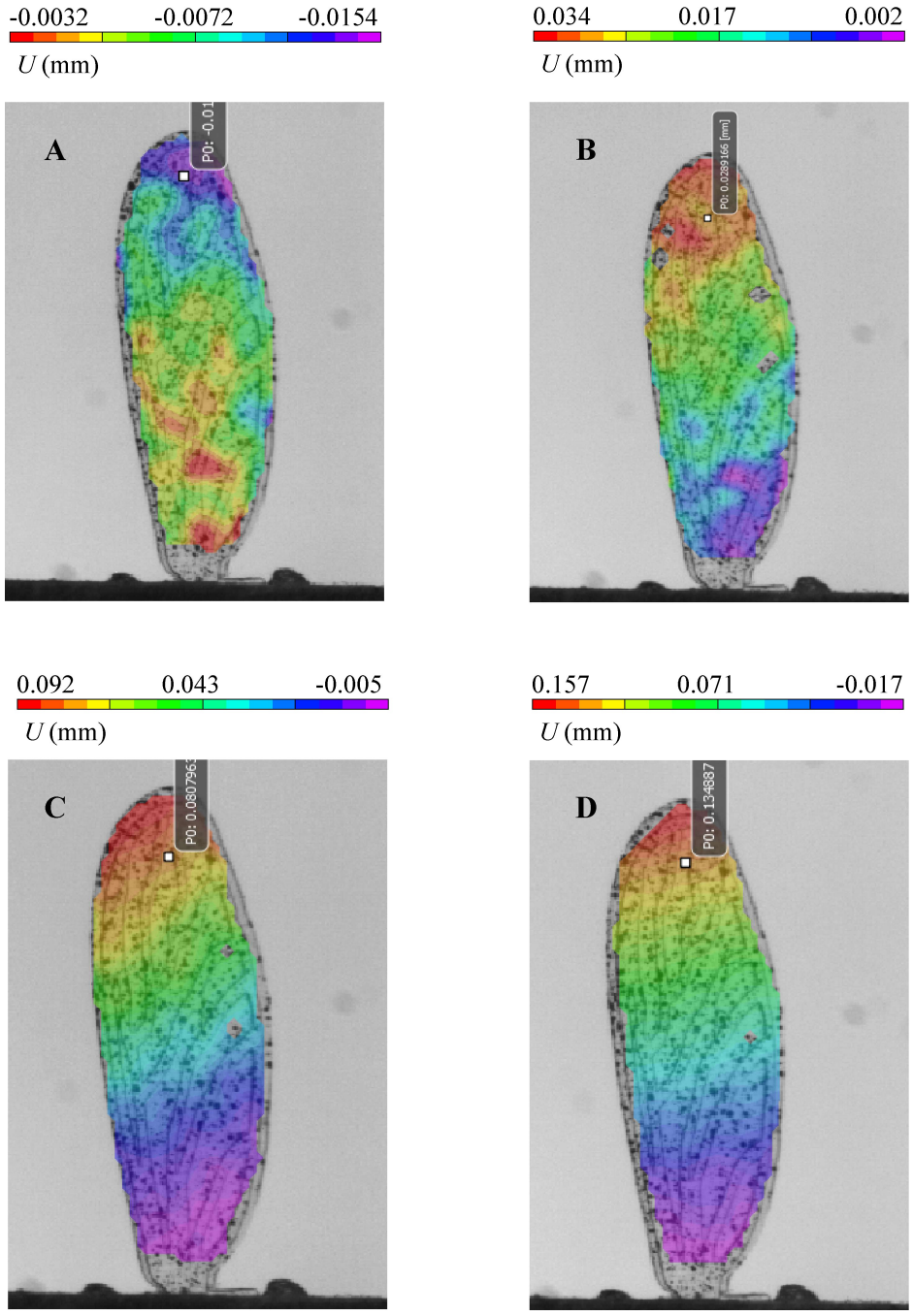

Figure 4.25 Experimental structural aerodynamic response of the artificial insect-sized wing. *Variation of the out-of-plane deformation of the composite material artificial wing sample number 3 for (a) Re=24, (b) Re=131, (C) Re=340, and (D) Re=552 at 30 deg angle of attack.*

4.4 Numerical Models

4.4.1 FE Model Validation

The FE model was validated by considering the benchmark cases of vibration of a rectangular plate, an elliptical membrane, and a tubular cantilever beam. These cases validated the selection of elements and the solution approach from the FE models of the artificial insect-sized wing and the crane fly forewing.

4.4.1.1 Shell Modeling Validation

A benchmark case of the vibrations of a rectangular flat shell was considered to validate the solution approach of the FE model of a shell. The natural frequencies of a FE model of a rectangular thin flat shell were calculated and compared with those from the analytical solution [93]. The FE rectangular shell model was developed as a thin shell with a thickness of 0.0125 mm, a width of 5.6 mm, and a length of 14 mm. These dimensions fairly agreed with the dimensions of the membrane of the composite material artificial wing. The material properties of the Kapton film, described in Table 2.4, were assigned to the FE model of the rectangular shell. The shell was clamped at one edge and free at the other three edges. The FE model of the rectangular shell was meshed using S4R (4-node general-purpose shell) type of elements. The natural frequencies of the rectangular shell were calculated with a converged mesh grid of 8037 nodes. The variation of the natural frequencies of the FE model and the analytical solution [93] was less than 1.0 % as shown in Table 4.9. Similarly, the first three mode shapes of the rectangular shell were determined and agreed with those from the analytical solution [93]. The mode shapes of the rectangular shell are shown in Fig. 4.26.

Table 4.9 Comparison between the natural frequencies of the FE model of the rectangular shell and the analytical solution [93]

Mode	Natural frequency (Hz)		
	Analytical solution [93]	FE model	Percent error (%)
First	15.32	15.20	0.78
Second	79.75	79.62	0.16
Third	95.60	94.87	0.76

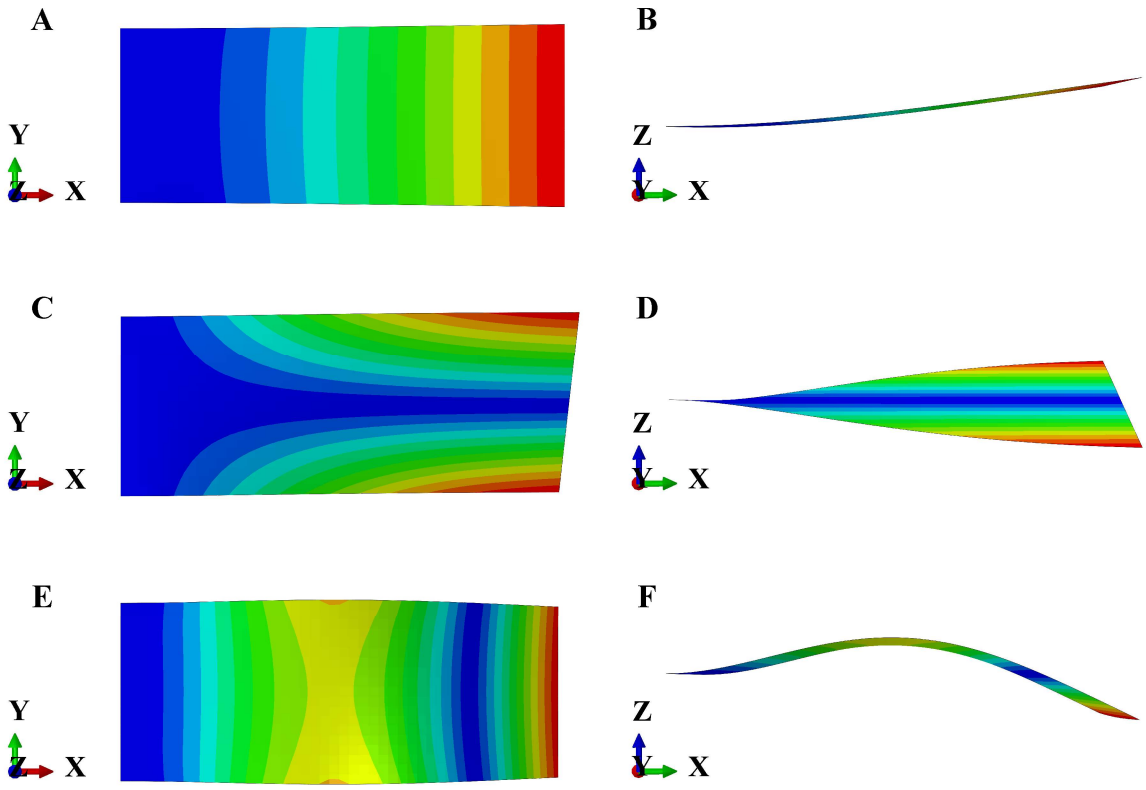

Figure 4.26 Mode shapes of the rectangular shell with one fixed end and three free ends. *(A and B) First at 15.20 Hz, (C and D) second at 79.62 Hz, and (E and F) third at 94.87 Hz mode shapes of the rectangular flat shell.*

4.4.1.2 Membrane Modeling Validation

A benchmark case of the vibrations of an elliptical membrane was considered to validate the solution approach of the FE model of a membrane. The natural frequencies of a FE model of

an elliptical membrane were calculated and compared with those from the analytical solution from Mathieu functions [106]. The FE elliptical membrane model was developed considering a thickness of 0.009 mm, a major radius of 6.93 mm, a minor radius of 1.6 mm, and a uniform pretension of 1000 Pa. These dimensions fairly agreed with those from the artificial insect-sized wing. The material properties of the Kapton film, described in Table 2.4, were assigned to the FE model of the elliptical membrane. The FE model of the elliptical membrane was meshed using M3D6 (6-node quadratic triangular membrane) type of elements. The natural frequencies of the elliptical membrane were calculated with a converged mesh grid of 4485 nodes. The variation of the natural frequencies of the FE model of the elliptical membrane and the analytical solution [106] was less than 1.0 % as shown in Table 4.10. Similarly, the first three mode shapes of the elliptical membrane were determined and agreed with those from the analytical solution [93]. The mode shapes of the elliptical membrane are shown in Fig. 4.27.

Table 4.10 Comparison between the natural frequencies of the FE model of the elliptical membrane and the analytical solution [106]

Mode	Natural frequency (Hz)		
	Analytical solution [106]	**FE model**	**Percent error (%)**
First	163.20	163.54	0.21
Second	185.62	186.25	0.34
Third	209.55	210.20	0.31

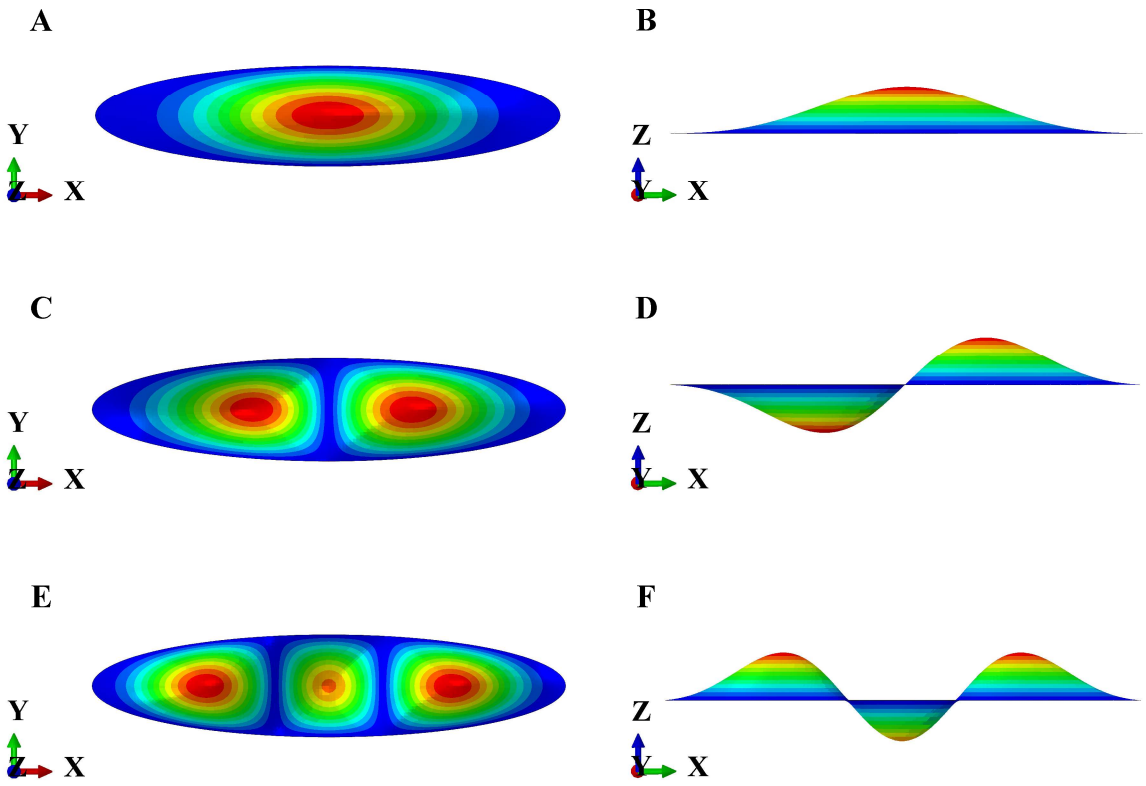

Figure 4.27 Mode shapes of the elliptical membrane with a clamped edge. *(A and B) First at 163.54 Hz, (C and D) second at 186.25 Hz, and (E and F) third at 210.20 Hz mode shapes of the elliptical membrane.*

4.4.1.3 Beam Modeling Validation

A benchmark case of the vibrations of a cantilever beam was considered to validate the solution approach of a FE model of a beam. The natural frequencies of a FE model of a

cantilever beam with a tubular cross-section were calculated and compared with those from the analytical solution using the Euler-Bernoulli beam theory [6]. The FE beam model was developed considering a length of 14 mm and a tubular cross-section with an outer diameter of 0.126 mm and an inner diameter of 0.045 mm. These dimensions were comparable to those from the thick veins of the artificial wing. The material properties of the SU-8, described in Table 2.4, were assigned to the FE model of the beam. The FE model of the cantilever beam was meshed using B32 (3-node quadratic beam) type of elements. The natural frequencies of the cantilever beam were calculated with a converged mesh grid of 121 nodes. The variation of the natural frequencies of the FE model of the cantilever beam and the analytical solution [6] was less than 1.0 % as shown in Table 4.11. Similarly, the first three mode shapes of the cantilever beam were determined and agreed with those from the analytical solution [6]. The mode shapes of the cantilever beam are shown in Fig. 4.28.

Table 4.11 Comparison between the natural frequencies of the FE model of cantilever beam with tubular cross-section and the analytical solution [6]

Mode	Natural frequency (Hz)		
	Analytical solution [6]	**FE model**	**Percent error (%)**
First	174.35	174.34	0.00
Second	1092.66	1092.10	0.05
Third	3059.48	3055.09	0.14

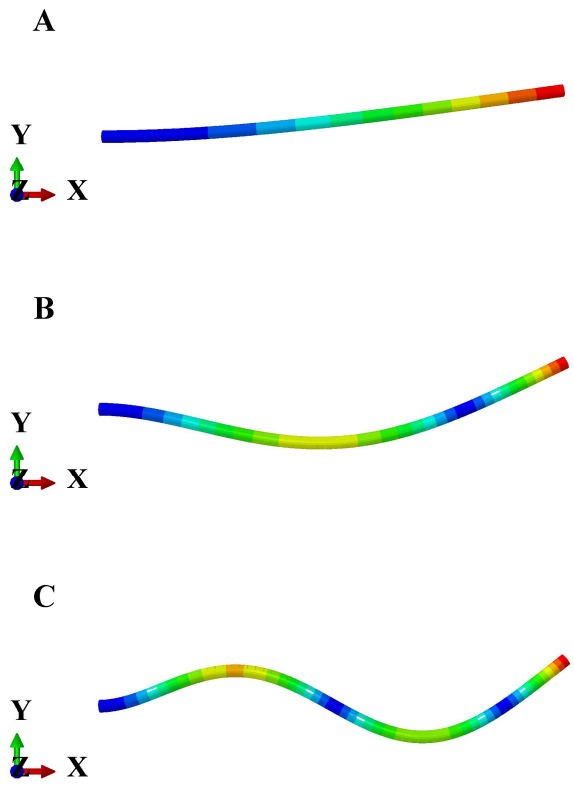

Figure 4.28 Mode shapes of the cantilever beam with tubular cross-section. *(A) First at 171.11 Hz, (B) second at 1096.91 Hz, and (C) third at 3069.30 Hz mode shapes of the cantilever beam with tubular cross-section.*

4.4.2 CFD Model Validation

A benchmark case of the boundary layer development for steady incompressible flow over a flat plate was investigated and compared with that from the Blasius solution [103] to

validate the CFD model. The boundary layer thickness δ is defined as the locus point where the velocity parallel to the plate reaches 99 % of the freestream velocity. Mathematically, the boundary layer thickness δ can be calculated from Eq. 4.2 [103]

$$\delta_x \approx \frac{5x}{\mathrm{Re}_x^{1/2}} \approx \frac{5x}{\sqrt{\frac{\rho V_\infty x}{\mu}}} \approx 5\sqrt{\frac{\mu x}{\rho V_\infty}} \tag{4.2}$$

where x represents the local distance along a flat plate of length L, Re_x is the local Reynolds number, ρ is the density of the fluid, μ is the absolute viscosity of the fluid, and V_∞ is the freestream velocity.

A CFD model of the flow over a flat plate was developed and sized based on a Reynolds number of 290 and a freestream velocity of 1.0 m/s, which are conditions typically encountered in the crane fly flight regime. The length of the plate was determined from the Reynolds number expression in Eq. 4.2. The working fluid considered was laminar incompressible air at standard atmospheric conditions. An inlet velocity, outlet pressure, symmetry velocity, and far-field velocity boundary conditions were specified on the CFD domain as described in Section 2.7.2. The CFD model was meshed using FC3D8 (8-node linear fluid hexahedral) type of elements. The mesh was structured and refined near the plate surface to accurately capture the boundary layer thickness and the velocity gradients. The calculations for the CFD model were conducted on a converged mesh grid with 8282 nodes.

The Blasius solution is expressed in terms of two nondimensional variables η and f'. These variables are defined in Eqs. 4.3 and 4.4 respectively [103],

$$\eta = y\sqrt{\frac{V_\infty}{\nu x}} \tag{4.3}$$

$$f'(\eta) = \frac{v_x}{V_\infty} \tag{4.4}$$

where y represents the normal distance or height from the surface of the plate, V_∞ is the freestream velocity, v is the dynamic viscosity, x is the local distance along the flat plate, and v_x is the x-component of the velocity profile.

The nondimensional variables predicted by the numerical solution agreed with those from the Blasius solution as shown in Fig. 4.29. Furthermore, a fair agreement with percent errors less than 14 % was found between the two solutions when calculating and comparing the boundary layer thickness at different locations along the flat plate as observed in Table 4.12. Discrepancies were expected given that the Blasius solution is a numerical solution for the boundary layer equations, a simplified version of the Navier-Stokes equations, which assumptions are more suitable for high Reynolds numbers [103]. Furthermore, the imposition of a far-field velocity boundary condition on the CFD model forced the entire mass flow to exit through the outlet face. This condition did not accurately represent the physical conditions from the Blasius solution; however, it was required to represent a well-posed mathematical formulation. Nonetheless, both solutions accurately predicted that the boundary layer thickness increased along the length of the flat plate.

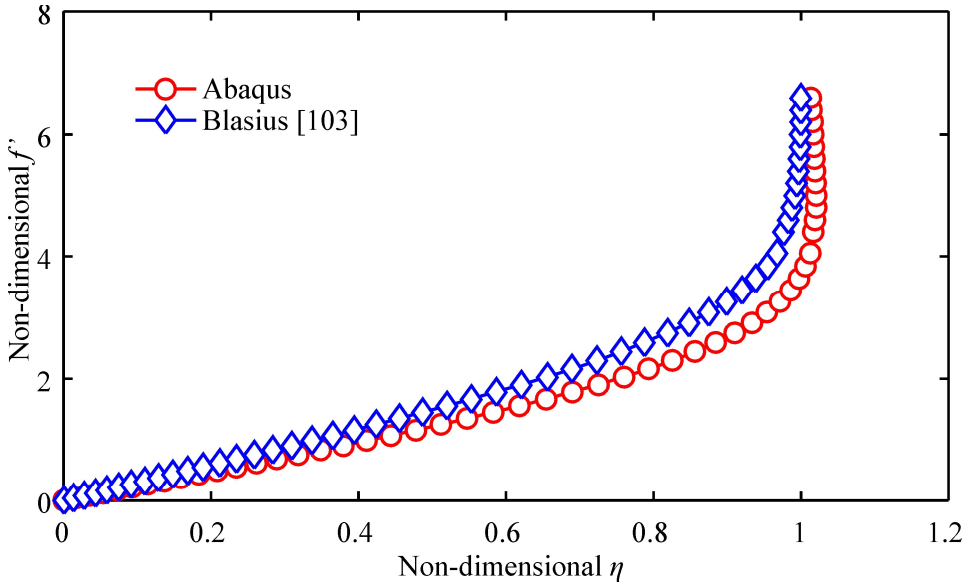

Figure 4.29 CFD validation. *Comparison between the CFD model and the Blasius solution [103] for the x-component of velocity profile along the trailing edge of the flat plate.*

Table 4.12 Comparison between the boundary layer of the CFD model solution and the Blasius solution

Location along flat plate (m)	**Boundary layer thickness, δ (mm)**		**Percent difference (%)**
	Blasius solution [103]	**FSI solution**	
0.2L	0.61641	0.63173	2.45
0.5L	0.97463	0.94910	2.65
L	1.37834	1.19870	13.94

4.4.3 FSI Validation

A benchmark case of the oscillations of a flexible plate due to an applied pressure on a resting fluid [108] was considered for the validation of the FE-CFD coupling. The FE model of the flexible plate was developed considering a length of 1.0 m, a width of 0.4 m, and a thickness of 0.06 m. A Young's modulus of 2.5 MPa, a Poisson's ratio of 0.35, and a density of 2550 kg/m^3 were assigned for the material properties of the FE model of the flexible plate. A clamped boundary condition was defined at the bottom face of the plate. The FE model was meshed using

S4R (4-node general-purpose shell) type of element. The mesh of the FE model was structured with a converged grid of 441 nodes. The CFD model was developed considering a length of 50 m, a height of 6.0 m, and a width of 0.4 m. The CFD model included a seamed partition inside the domain with the exact dimensions of the flexible plate. The partition was located at a distance of 100. m from the inlet of the CFD domain. The working fluid was assigned a density of 1 kg/m^3 and a dynamic viscosity of 0.2 N·s/m^2. The CFD model was meshed using FC3D8 (8-node linear fluid hexahedral) type of elements. The converged mesh of the CFD model was structured and refined near the seamed partition with 19,085 nodes. The boundary conditions of the CFD model were assigned as specified in Section 2.7.2. Co-simulation interfaces were specified for both the FE and CFD domain to conduct the FSI simulation. A good correlation was found between the predictions of the Abaqus FSI and the literature results [108] as observed in Fig. 4.30.

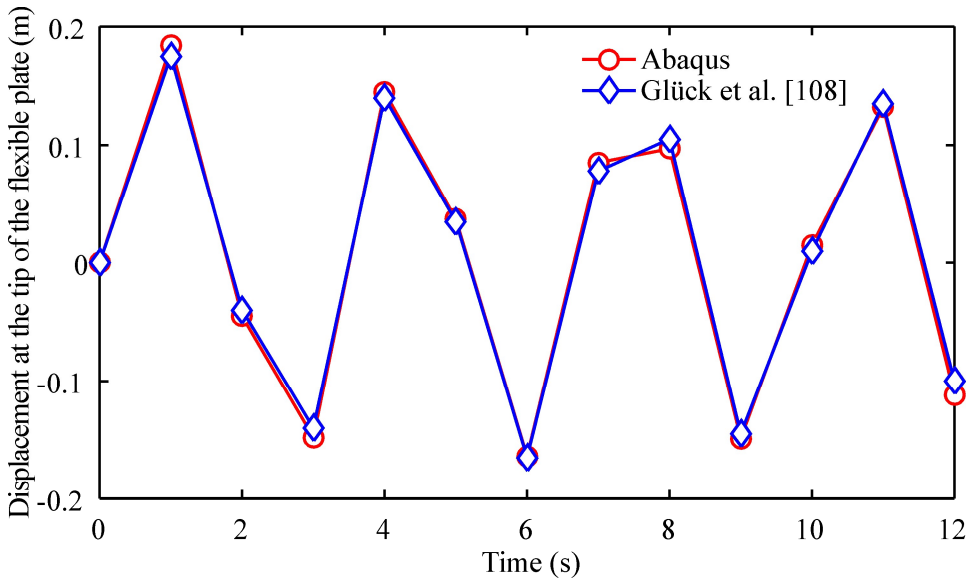

Figure 4.30 FSI validation. *Comparison between the FSI model and the results from Glück [108] for the oscillations at the tip of a flexible plate due to an applied pressure.*

4.4.4 Vibrations Analysis of the Artificial Insect-Sized Wing

4.4.4.1 Mesh Independence Study

The natural frequencies of the artificial wing were calculated over a range of significantly different mesh resolutions to demonstrate grid-independent results. The node-to-surface tie constrained required the master membrane surface to have more nodes than the slave vein surfaces. The natural frequencies of the artificial insect-sized wing were mesh independent for a mesh with 3000 nodes or higher as observed in Fig. 4.31. This resolution was achieved with an element size of 0.25 mm for the membrane mesh and 0.5 mm for the vein mesh. The mesh was sufficiently refined with this resolution given that a further increment of the number of nodes (attained by decreasing the element size) produced a negligible change in the results. The different mesh resolutions tested for the FE model are shown in Table A.1 from Appendix I.

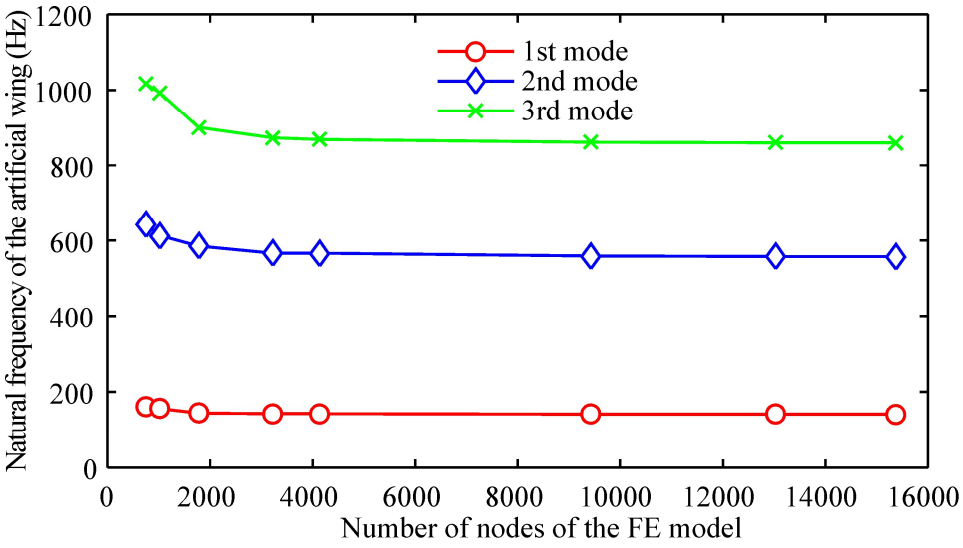

Figure 4.31 Mesh independence study for the FE model of the artificial insect-sized wing. *Variation of the natural frequencies of the composite material artificial wing with respect to mesh resolution of the FE model.*

4.4.4.2 Modal Characterization of the Artificial Insect-Sized Wing

For the modal analysis, the artificial wing was considered as a distributed-parameter system where its mass and stiffness was distributed throughout its structure as a series of infinitely small elements. This arrangement entails an infinite number of degrees of freedom; hence, it is also said that the wing structure has an infinite number of natural frequencies. For this investigation, the first three natural frequencies with their respective mode shapes were examined for the modal characterization of the artificial insect-sized wing.

The natural frequencies of both the composite material and the single material wing artificial wing were computed using a converged mesh grid with 9428 nodes. This grid was generated with elements sizes of 0.1 mm for the membrane mesh and 0.3 mm for the vein mesh. As expected, the magnitude of each natural frequency increased with the corresponding mode as observed in Table 4.13.

The single material presented higher natural frequencies because of the higher Young's modulus of the SU-8 membrane compared to that of the Kapton film. The previous statement is supported by the classical vibration theory which states that the natural frequencies of a distributed-parameter system are a function of both the Young's modulus and the cross-sectional area moment of inertia of the structure [6].

The first three mode shapes of the artificial wing are shown in Fig. 4.32. The mode shapes showed a bending and torsional deformation response as observed on the results from the experimental modal analysis presented in Section 4.3.5. Such response confirmed the relative flexibility of both the leading edge and the tip of the artificial insect-sized wing.

Table 4.13 Natural frequencies of the artificial insect-sized wing calculated from the FE model

Mode	Natural frequency (Hz)	
	Composite material	Single material
First	143.94	169.94
Second	561.38	647.69
Third	870.35	1050.70

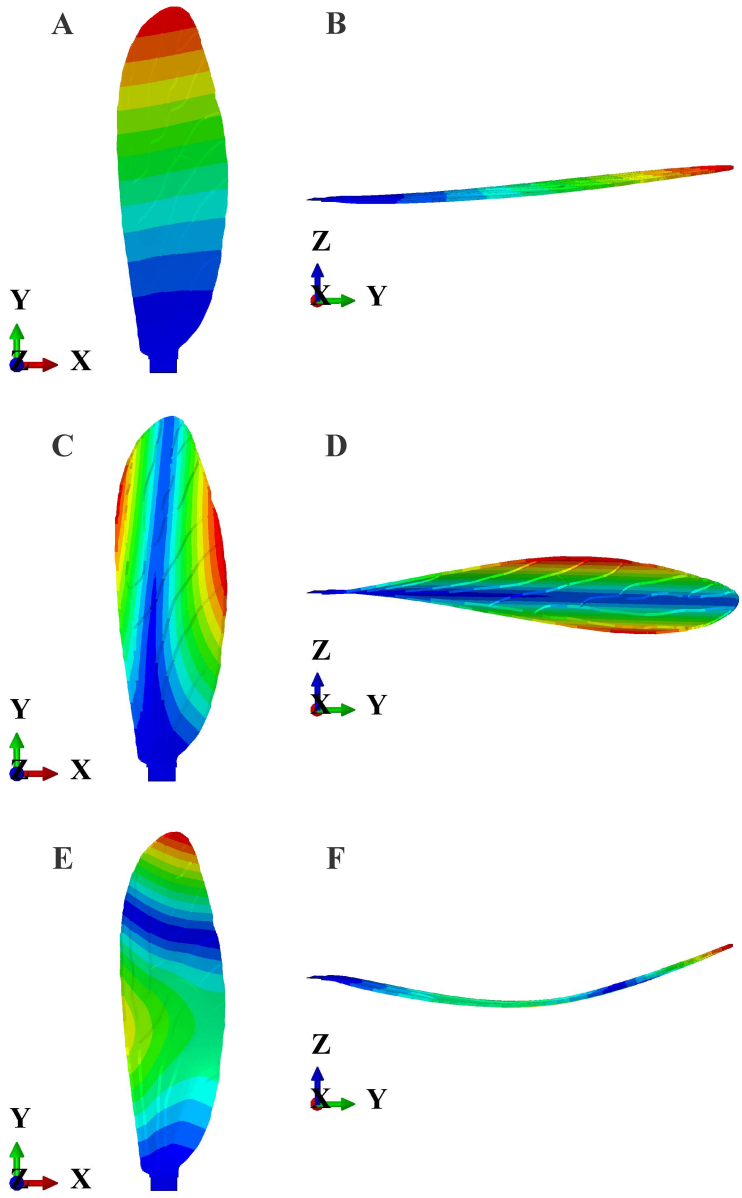

Figure 4.32 Mode shapes of the artificial insect-sized wing. *(A and B) Front and side view of first mode shape (C and D) front and side view of second mode shape, and (E and F) front and side view of third mode shape of the artificial insect-sized wing.*

4.4.5 Aerodynamic Response of the Artificial Insect-Sized Wing

4.4.5.1 Mesh Independence Study

The mesh independence of the results from the FSI simulations was investigated by considering a case with steady airflow for a Reynolds number of 2.9 at 10 deg angle of attack. The deformation magnitude at node *A* (located as shown in Fig. 4.33) and the coefficients of drag and lift of the FSI surface were calculated over a range of different mesh resolutions to demonstrate grid-independent results. The calculations from the FSI simulations were mesh independent for a mesh with 240,000 nodes or higher in the CFD model as shown in Fig. 4.34. This resolution was achieved with a global element size of 2 mm, a local element size at the FSI wing edge of 0.15 mm, and a structured layered mesh consisting of 20 layers distributed along the positive and the negative out-of-plane directions of the FSI surface with a bias of 30. The different mesh resolutions tested for the FSI simulation are shown in Table A.2 from Appendix II.

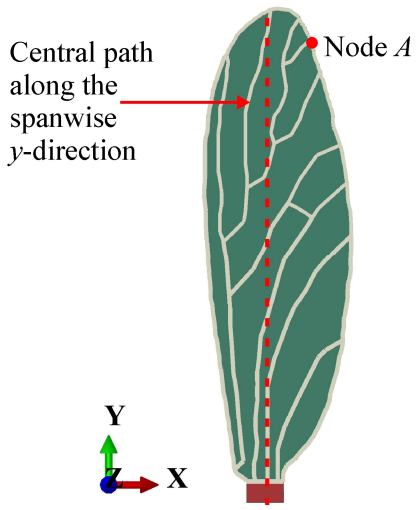

Figure 4.33 Location of the node A and central path along the spanwise y-direction. *The node A was defined to monitor the convergence of the FSI results. A central path along the spanwise y-direction of the artificial wing was defined for the analysis of the FSI results.*

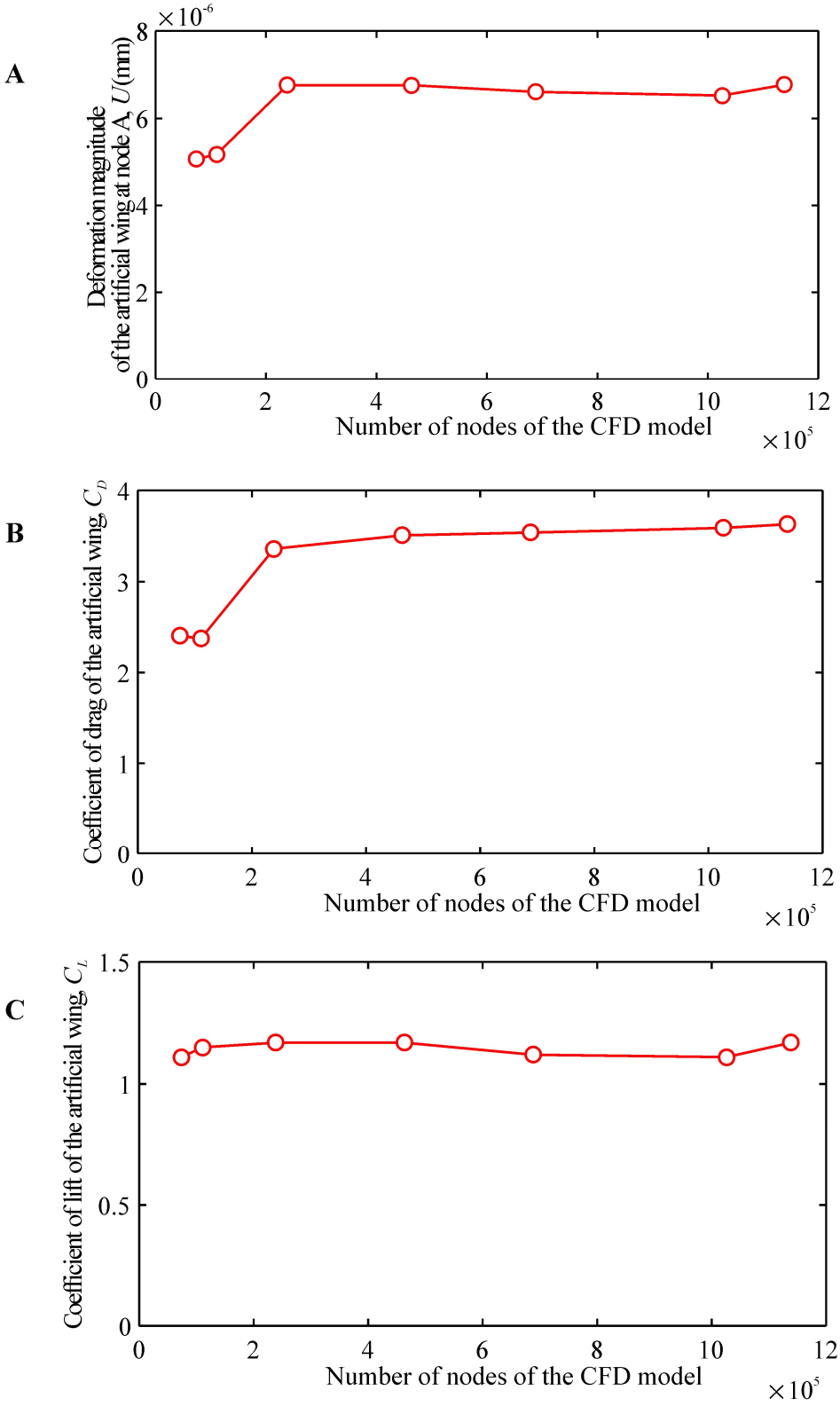

Figure 4.34 Mesh independence study for the FSI simulation. *The variation of (A) the deformation at node A, (B) the coefficient of drag, and (C) the coefficient of lift of the artificial wing with respect to a change of the number of nodes in the CFD mesh only was monitored for the mesh independence study.*

4.4.5.2 Structural Aerodynamic Response of the Artificial Insect-Sized Wing

The deformation and stress distributions of the artificial insect-sized wing under steady airflow at different Reynolds number and angles of attack were calculated from the FSI simulation. The considered Reynolds numbers were within the ranges at which the nature counterpart, namely the crane fly, typically maneuvers and hovers. The results from the FSI simulation for the artificial insect-sized wing were computed using a mesh grid with 350,000 nodes. This grid was generated with a global element size of 2.8 mm, a local element size at the FSI wing edge of 0.18 mm, and a structured layered mesh consisting of 50 layers distributed along the positive and the negative out-of-plane directions of the FSI surface with a bias of 100.

The steady state solution converged through an iterative process that computed an approximate solution to the system of algebraic equations derived from the discretization of the governing differential equations. The solution was considered converged when the calculated residuals for each cell fell below a specified convergence limit. For this investigation, the convergence criteria were set to 1×10^{-10}.

The deformation and stress responses of the artificial wing to aerodynamic loading for different Reynolds number at 10 deg angle of attack are shown in Figs. 4.35 and 4.36. In general, the stress and deformation distributions were similar for all Reynolds numbers and differed only in their magnitudes. The deformation increased nonlinearly along the spanwise *y*-direction of the artificial wing as observed in Figs. 4.35A, 4.35C, 4.35E, 4.35G, 4.36A, 4.36C, 4.36E, and 4.36G. The deformation at the base of the wing and its near surroundings was almost negligible due to the clamped condition assigned to the FE model and the stiffness provided in this area by the thicker veins. Contrarily, the maximum deformation was estimated near the tip of the wing where the stiffness was significantly lower compared to the stiffness at the root, mainly due to

the presence of thinner structural veins. A similar behavior was observed on the static bending tests performed by Combes and Daniel [22] and Mengesha et al. [75] on different insect species. The results from the stress analysis in Fig. 4.35B, 4.35D, 4.35F, 4.36B, 4.36D, and 4.36F showed higher stress concentrations at the root of the wing near the leading edge. It was expected for this region to experience high localized stress because it initially received and absorbed the incoming flow momentum.

From a mechanical point of view, the veins provided the dominating contribution to the structural dynamic response of the wing due to their higher stiffness and greater load-bearing capacity inherent to its cross-sectional structure. In essence, the veins were a network of beams that held together the wing and provided the main bending and torsional resistance to inertial and aerodynamic loadings. Nonetheless, the membrane, which was modelled as a shell, had a minor yet important contribution as a reinforcement layer capable of carrying membrane and bending forces.

The aerodynamic efficiency of the artificial wing was investigated by calculating the coefficients of drag and lift for different Reynolds numbers as shown in Figs. 4.37A and 4.37B, respectively.

The coefficient of drag decreased nonlinearly with Reynolds number and increased with angle of attack. The decrease of the coefficient of drag with Reynolds number could be explained by the viscous effects accentuated at the low Reynolds number and the development of the viscous boundary layer [103]. The increment of the coefficient of drag with angle of attack was accounted by the effects of flow separation that generated the so-called pressure drag at high angles of attack.

The coefficient of lift increased with Reynolds number and angle of attack up to approximately an angle of 15 deg. This phenomenon was expected given that with high freestream velocity and angle of attack a greater pressure difference between the upper and lower surfaces of the artificial wing was developed. The rate started to decrease at the 15 deg angle of attack especially for high Reynolds numbers. At this angle, the adverse pressure differences started to develop due to flow separation.

The aerodynamic efficiency of the artificial wing, defined as the ratio of the coefficient of lift to the coefficient of drag, increased with both Reynolds number and angle of attack up to the critical angle of attack of approximately 15 deg as shown in Fig. 4.37C. At this angle, the generation of lift increased slightly with angle of attack; however, the generation of pressure drag became predominant due to flow separation and reversed flow effects. These effects started to be accentuated at 30 deg, 20 deg, and 15 deg for a Reynolds number of 29, 150, and 290, respectively, as observed in Figs. 4.38–4.40. The consequences of these effects were that the aerodynamic efficiency started to decrease dramatically after the critical angle of attack. Nonetheless, the aerodynamic efficiency of the artificial wing shows that the lift force exceeded the drag force even beyond the critical angle of attack for high Reynolds number flow. This behavior supports the evidence that the effects of the passive deformation mechanisms on the aerodynamic performance of flexible wings will be significant at high Reynolds number flow and wingbeat conditions as studied by different researchers [2, 19, 20, 33, 110, 111].

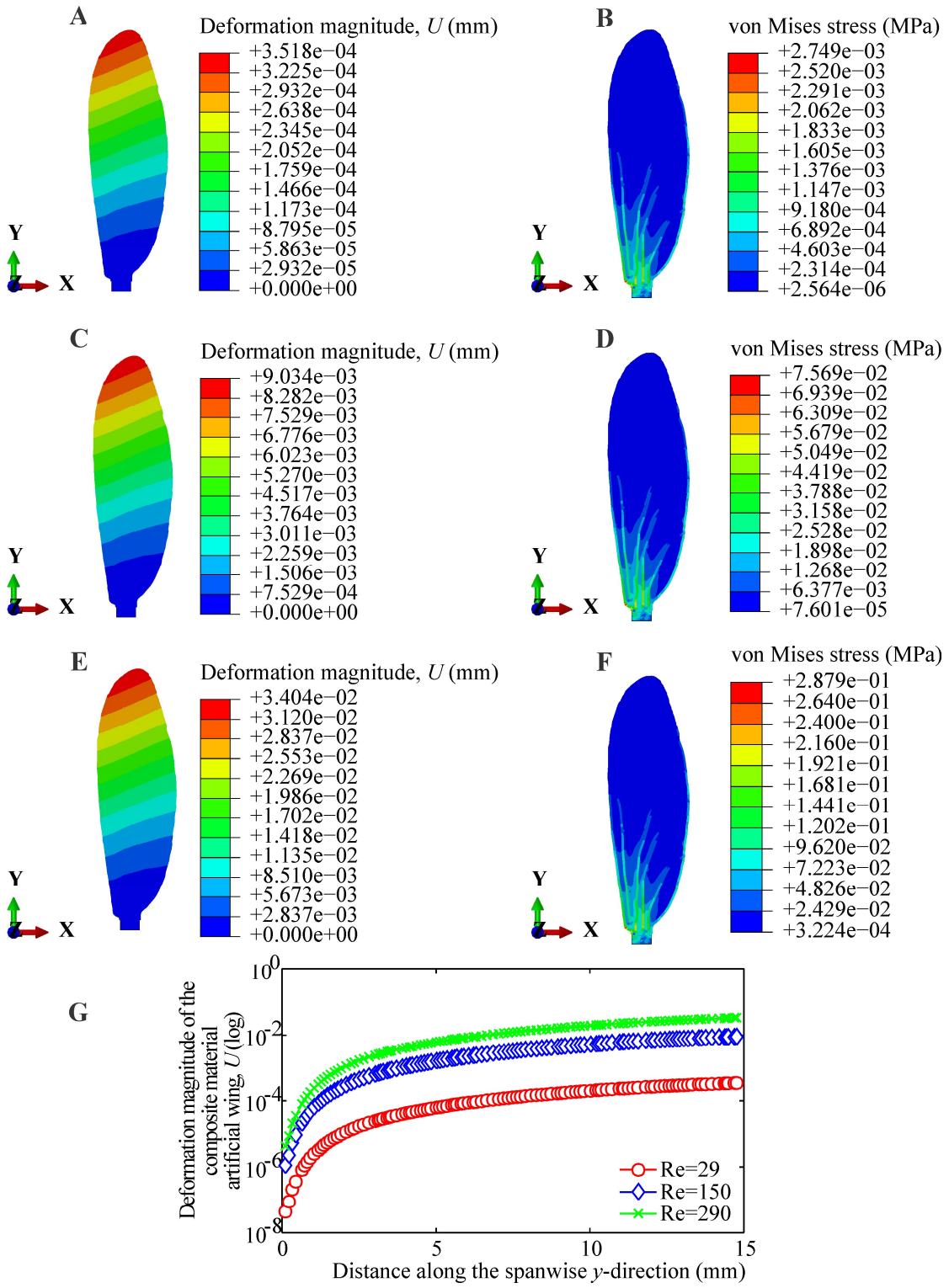

Figure 4.35 Structural deformation response of the composite material artificial insect-sized wing. *Deformation and von Mises stress of the artificial insect-sized wing under steady airflow for (A and B) Re=29, (C and D) Re=150, and (E and F) Re=290 and 10 deg angle of attack; and (G) deformation magnitude along a central path in the spanwise y-direction under steady airflow for different Reynolds number.*

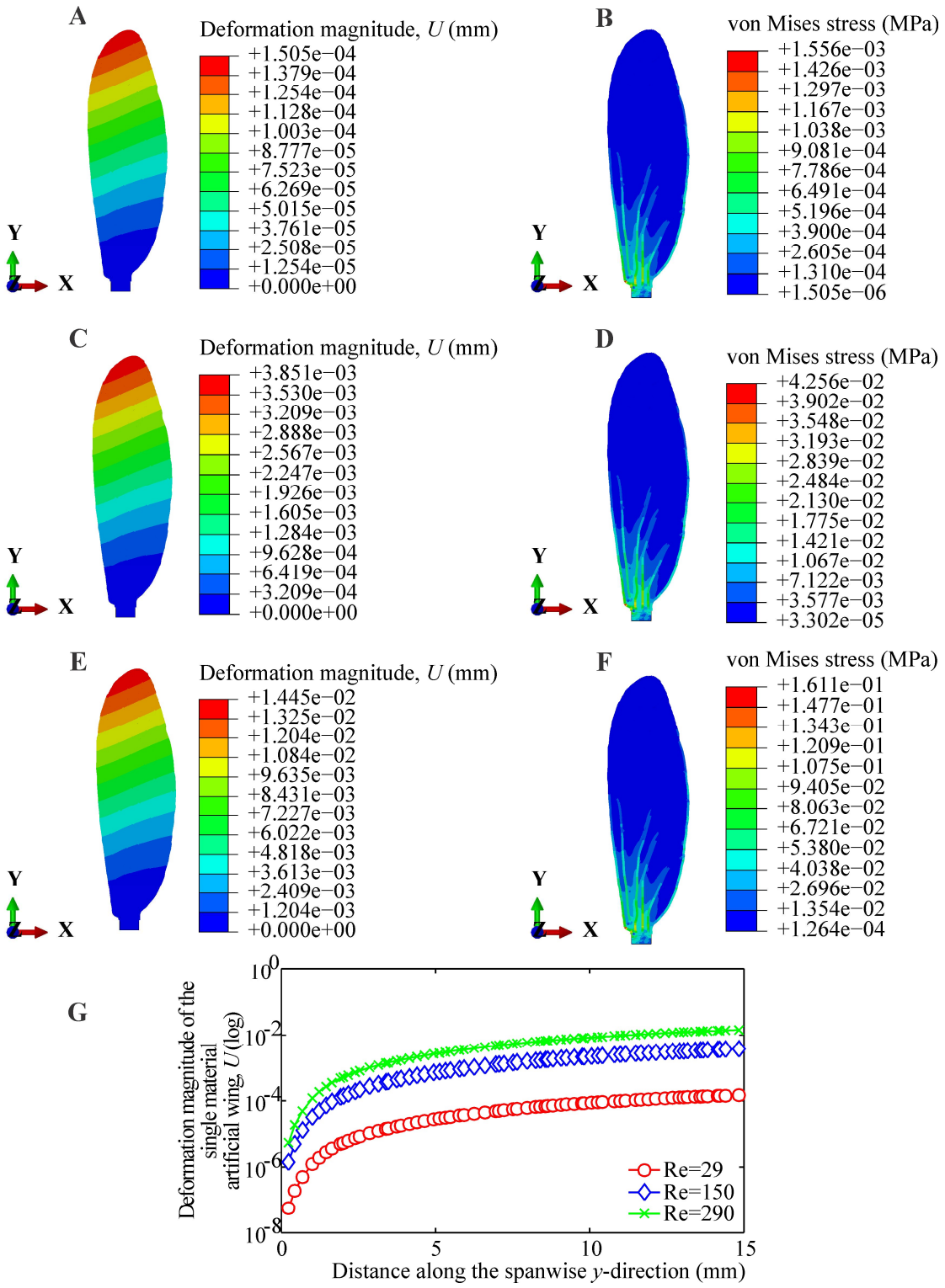

Figure 4.36 Structural deformation response of the single material artificial insect-sized wing. *Deformation and von Mises stress of the artificial insect-sized wing under steady airflow for (A and B) Re=29, (C and D) Re=150, and (E and F) Re=290 and 10 deg angle of attack; and (G) deformation magnitude along a central path in the spanwise y-direction under steady airflow for different Reynolds number.*

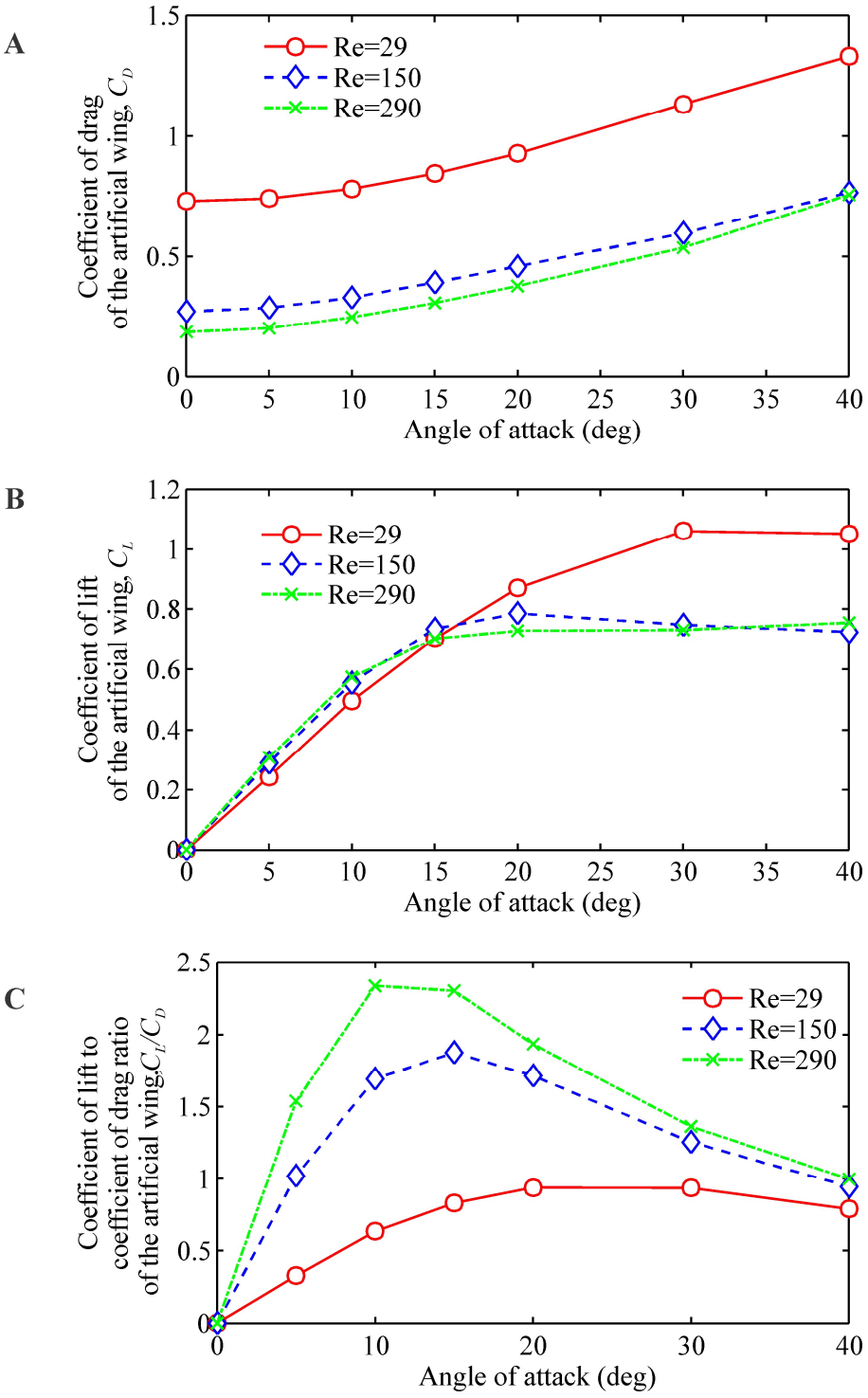

Figure 4.37 Aerodynamic performance of the artificial insect-sized wing. *(A) Coefficient of drag variation with respect to angle of attack and Reynolds number, (B) coefficient of lift variation with respect to angle of attack and Reynolds number, and (C) aerodynamic efficiency of the artificial insect-sized wing.*

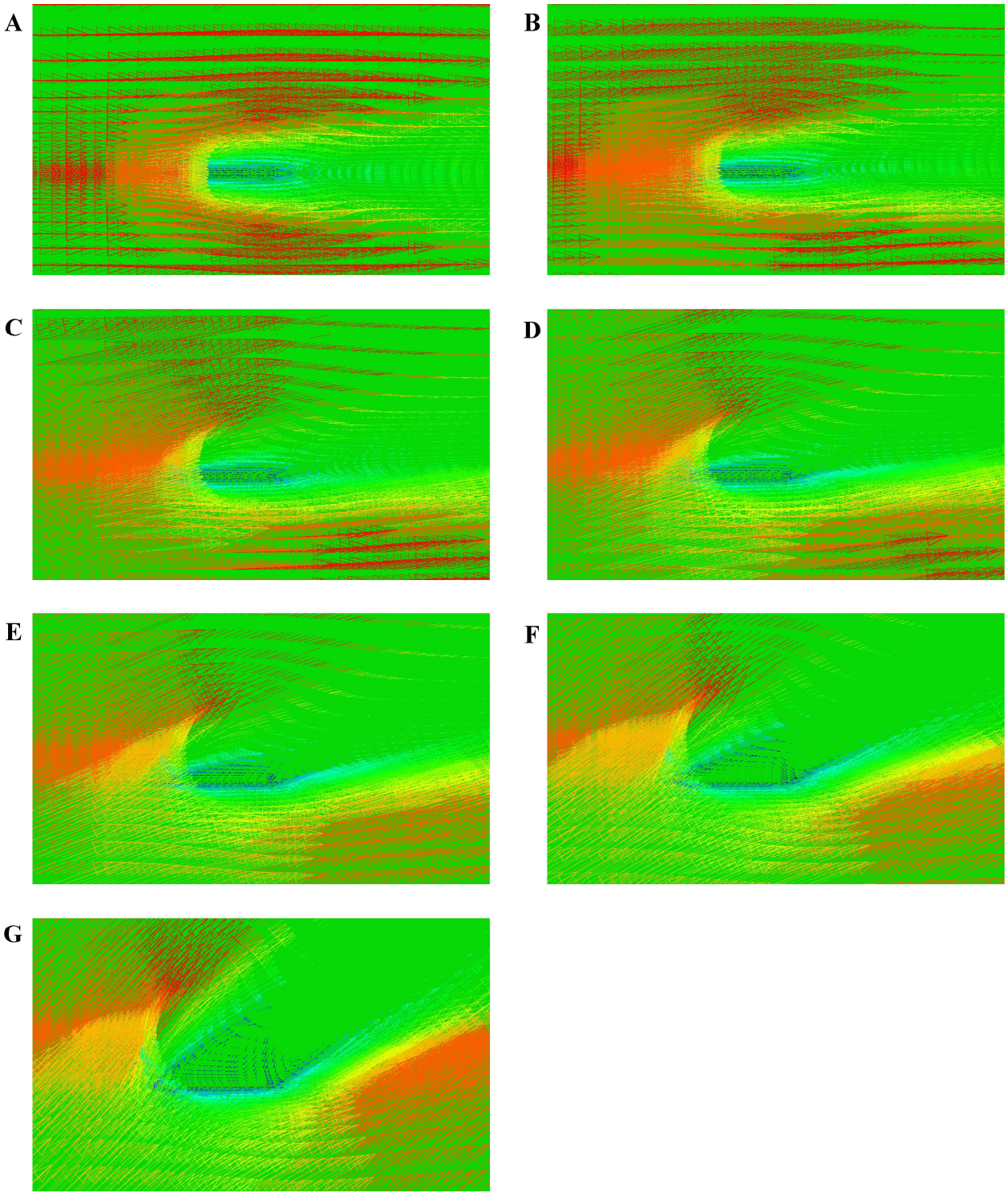

Figure 4.38 Velocity vectors for a Reynolds number of 29. *Velocity vectors of the flow over the artificial wing for (a) 0 deg, (b) 10 deg, (c) 15 deg, (d) 20 deg, (e) 25 deg, (f) 30 deg, and (g) 40 deg angles of attack for a Reynolds number of 29.*

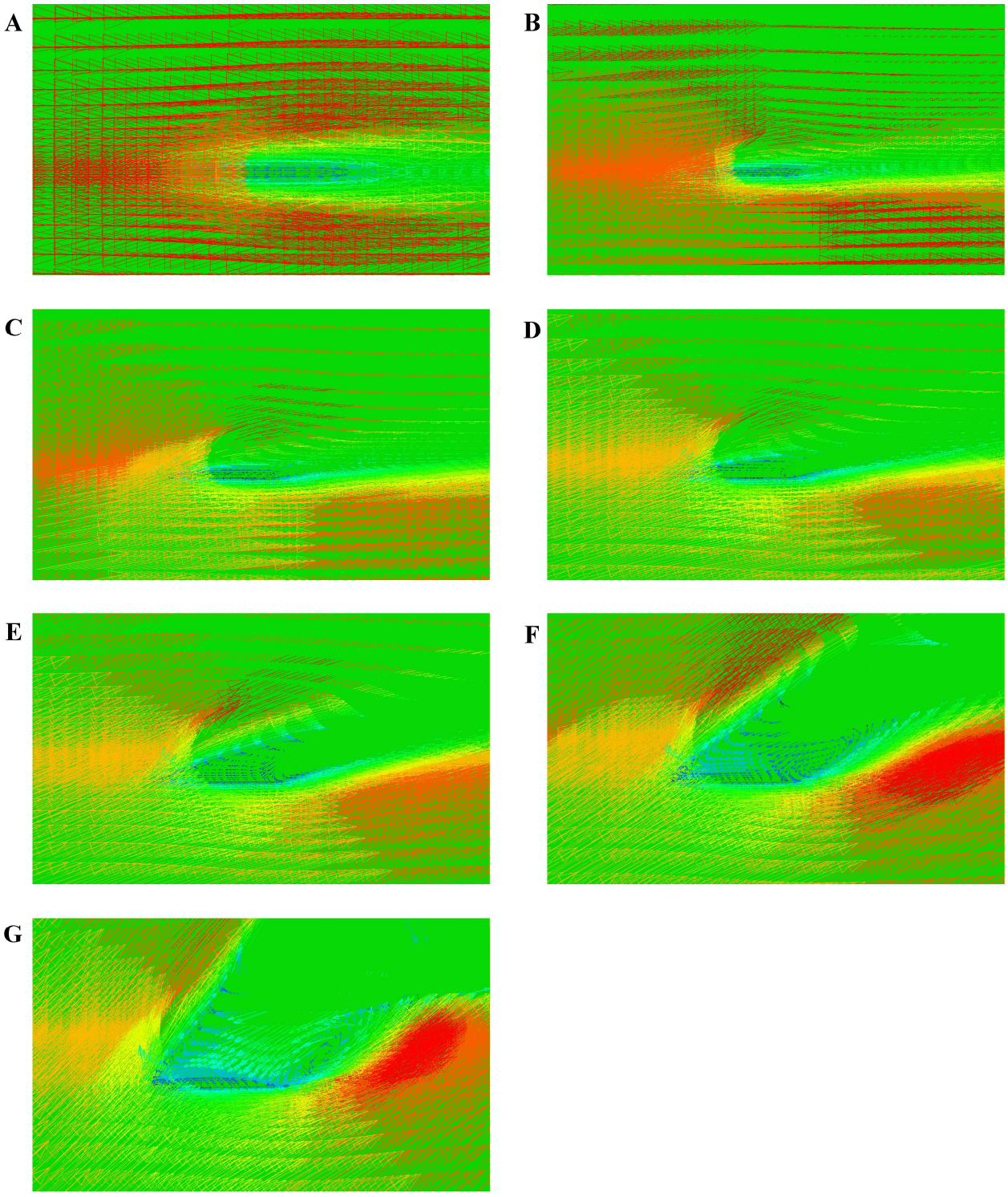

Figure 4.39 Velocity vectors for a Reynolds number of 150. *Velocity vectors of the flow over the artificial wing for (a) 0 deg, (b) 10 deg, (c) 15 deg, (d) 20 deg, (e) 25 deg, (f) 30 deg, and (g) 40 deg angles of attack for a Reynolds number of 150.*

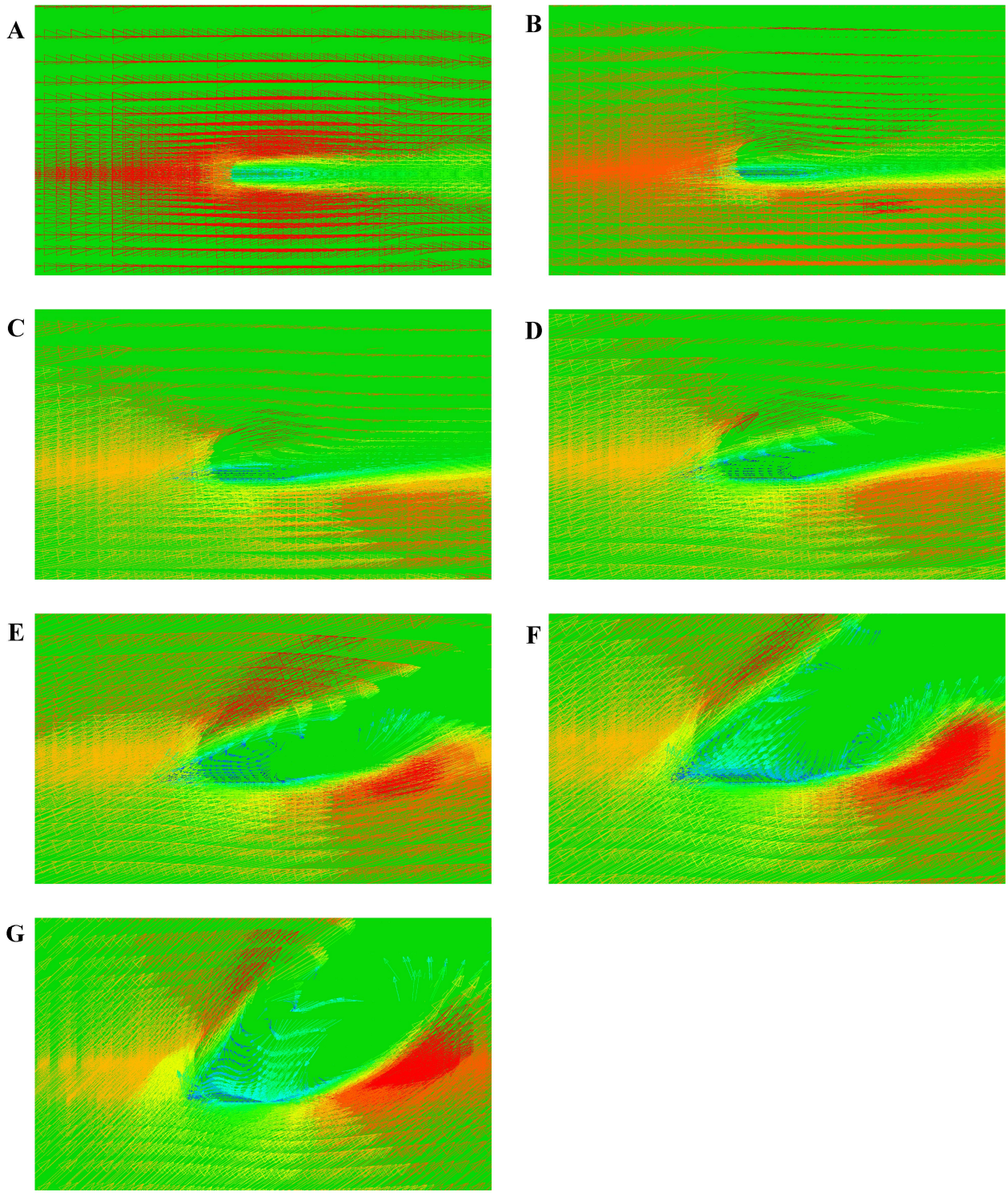

Figure 4.40 Velocity vectors for a Reynolds number of 290. *Velocity vectors of the flow over the artificial wing for (a) 0 deg, (b) 10 deg, (c) 15 deg, (d) 20 deg, (e) 25 deg, (f) 30 deg, and (g) 40 deg angles of attack for a Reynolds number of 290.*

CHAPTER 5 CONCLUSIONS

The remarkable maneuverability and aerodynamic efficiency of insects have created an intrinsic interest on learning the mechanisms that govern insect flight and consequently consider their further applications in engineered devices, namely micro air vehicles. The wings of biologically inspired micro air vehicles must be flexible structures that biomimic the morphological characteristics and the structural dynamic response of airborne insects.

This investigation describes a method for manufacturing a biologically-inspired artificial insect-sized wing and characterizing through experimental and numerical methods its vibrations and structural aerodynamic response. The internal and external morphologies of the crane fly forewing were captured and studied using a micro-computed tomography scan for the identification of key structural design parameters to be implemented in the biomimetic artificial wing. The artificial insect-sized wing structure was manufactured using the photolithography technique with materials that had comparable mechanical properties to those of the insect. A single material and a composite material artificial insect-sized wing were manufactured. Both designs included a thin membrane layer attached to a network of structural veins with varying widths for an asymmetric stiffness distribution along the span of the wing. The modal characteristics of the artificial structure were determined from the Fourier analysis of the out-of-plane displacement data captured using a shaker and a digital correlation image system. The structural aerodynamic deformation of the biomimetic wing was obtained using a wind-tunnel setup together with a digital image correlation system. A finite element model was developed from the reconstructed model of the micro-computed tomography scan for the calculations of the natural frequencies and mode shapes of the artificial wing. Furthermore, a fluid-structure interaction model was developed by coupling the finite element model of the artificial wing with

a computational fluid dynamics model to investigate the deformations of the wing under different aerodynamic conditions and the respective coefficients of drag and lift. The following conclusions are drawn from this investigation:

1) The morphology of the crane fly forewing is characterized by a uniform thickness membrane attached to a venation system consisting of veins of two different thicknesses that took into account the stiffness variation along the span of the wing. These morphologies can be accurately captured using a micro-computed tomography scan.
2) The photolithography process is an accurate method to manufacture an artificial insect-sized wing that can replicate the morphology and the structural behavior of their nature counterpart. An accurate biomimic of the membrane and the vein network of the crane fly is achieved using a composite wing structure and a single material wing structure.
3) The mode shapes of the artificial insect-sized wing and the crane fly forewing are dominated by bending and torsional deformation responses. This behavior provided an insight of the stiffness distribution of the insect wing with slightly more flexible regions at the tip of the wing and at the middle-section of the leading and trailing edges.
4) An asymmetric stiffness distribution along the span of the wing is achieved through a vein network composed of veins with different widths. The varying vein width distribution alters the resistance to inertia and external loads along the chordwise and spanwise axis of the artificial wing. Specifically, it allows a pliant deformation

response of the artificial wing as manifested through the bending and torsional characteristics of the mode shapes.

5) The displacement distributions of the artificial wing are dominated by the out-of-plane deformation which increased nonlinearly from the root to the tip of the wing with freestream velocity. Such behavior is due to the stiffness provided at the root of the wing by the fixed constraint and the thick veins. This stiffness distribution gradually decreases along the span of the wing and confirms that the veins are indeed more than a circulatory medium for the insect wing but also an important structural feature. The presence of a nonlinear deformation distribution suggests that the stiffness variation along the span of the wing has an important role when generating the desired elastic deformations that are well known to enhance the lift capability of insects. In other words, the stiffness variation, accounted by the different vein widths within the venation pattern, serves as the passive regulatory mechanism for the deformation experienced by insects during flight.
6) The random base excitation signal provides a time effective method to identify the natural frequencies of the artificial insect-sized wing using Fourier analysis. The leakage is minimized and sharp peaks on the frequency spectrum are identified using this type of broadband base excitation signal. The noise of the frequency spectrum can be effectively minimized by implementing a linear averaging technique.
7) At low Reynolds numbers, the artificial wing experiences effects of viscous drag due to the development of a boundary layer. Contrarily, as the wing translates to a higher angle of attack, the effects of pressure drag caused by flow separation and reversed flow become predominant.

8) The coefficient of lift of the artificial wing increases with Reynolds number and angle of attack. These two trends are sustained up to the critical angle of attack at which the rate of lift generation decreases due to the adverse pressure difference in the surfaces of the artificial wing caused by the separation of the flow from the surface of the wing.
9) The aerodynamic efficiency of the artificial wing increases with angle of attack and Reynolds number up to the critical angle of attack. At high Reynolds number, the lift force exceeds the drag force at angles above the critical angle of attack. This behavior suggests that the effects of the passive deformation mechanisms on the aerodynamic performance of flexible wings will be significant at high Reynolds number flow and wingbeat conditions.
10) The composite material and the single material wing are promising structures to be implemented as a wing for a micro air vehicle. Both artificial structures biomimic the morphology and flexible structural deformation response expected of an insect wing. The composite material artificial exhibits a higher pliancy; nonetheless, the single material wing provides a better dimensional accuracy to biomimic the morphology of the insect wing.

FUTURE WORK AND RECOMMENDATIONS

This work is intended to serve as the starting point for the design of a biologically inspired insect-sized MAV. The design and manufacturing of a flexible biomimetic wing structure is one of the most critical aspects of the design process of an insect-sized flapping MAV. However, this work can be further extended to investigate the structural dynamic response of the biomimetic wing under loading scenarios proper to the flapping flight. The following recommendations are made for this study:

1) Design a flapping mechanism to investigate experimentally the structural dynamic response of the artificial wing under flapping motion at different aerodynamic conditions inside the wind tunnel.
2) Design and manufacture a force measurement experimental setup to measure the low magnitude aerodynamic forces generated by the insect-sized artificial wing; thus, to be able to determine experimentally the respective aerodynamic coefficients.
3) Develop a fluid-structure interaction model of the artificial wing undergoing oscillatory flapping motion to predict and analyze the full-field time-varying deformations, aerodynamic coefficients, and the flow characteristics.
4) Quantify the asymmetric stiffness distribution along the surface of the wing to determine how the variation of the venation pattern could modify the deformation response and the production of the aerodynamic forces in steady and flapping flight.
5) Implement a micro-beam mask to improve the resolution of the photolithography procedure. This technique does not require the use of any mask so the pattern is directly written into the photoresist coated wafer. Furthermore, the correct type of wavelength can be delivered using this procedure.

REFERENCES

[1] Anderson, J. D., 2016, Fundamentals of Aerodynamics, sixth ed., McGraw-Hill Education, New York, New York, USA.

[2] Sane, S., 2003, "The aerodynamics of insect flight," *J. Exp. Biol.*, **206**, pp. 4191–4208, doi: 10.1242/jeb.00663.

[3] Klowden, M. J., 2013, Physiological Systems in Insects, third ed., Elsevier, London, England.

[4] Miller, L. A., and Peskin, C. S., 2004, "A computational fluid dynamics of 'clap and fling' in the smallest insects," *J. Exp. Biol.*, **208**, pp. 195–212, doi: 10.1242/jeb.01376.

[5] Rao, S., 2011, Mechanical Vibrations, fifth ed., Pearson Education Inc., Upper Saddle River, New Jersey, USA.

[6] Inman, D. J., 2007, Engineering Vibration, third ed., Pearson Education Inc., Upper Saddle River, New Jersey, USA.

[7] McMichael, J. M., and Francis, M. S., 1997, "Micro air vehicles-towards a new dimension in flight," *Unmanned Systems*, **15**, pp. 10–15.

[8] Pines, D., and Bohorquez, F., 2006, "Challenges facing future micro-air-vehicle development," *J. Aircraft*, **23**, pp. 290–304, doi: 10.2514/1.4922.

[9] Wootton, R. J.,1990, "The mechanical design of insect wings," *Sci. Am.*, **203**, pp. 114–120, doi: 10.1146/annurev.en.37.010192.000553.

[10] Ellington, C. P., 1984, "The aerodynamics of hovering insect flight. IV. Aerodynamic mechanisms," *Philos. Trans. R. Soc. Lond. B, Biol. Sci.*, **305**, pp. 79–113, doi: 10.1098/rstb.1984.0052.

[11] Miller, L. A., and Peskin, C. S., 2009, "Flexible clap and fling in tiny insect flight," *J. Exp. Bio.*, **212**, pp. 3076–3090, doi: 10.1242/jeb.028662.

[12] Santhanakrishnan, A., Robinson, A. K., Jones, S., Lowe, A., Gadi, S., Hedrick, T. L., and Miller, L. A., 2014, "Clap and fling mechanism with interacting porous wings in tiny insect flight," *J. Exp. Bio.*, **217**, pp. 3898–3909, doi:10.1242/jeb.084897.

[13] Ellington, C. P., van den Berg, C., Willmont, A. P., and Thomas, A. R., 1996, "Leading edge vortices in insect flight," *Nature*, **348**, pp. 626–630, doi: 10.1038/384626a0.

[14] Birch, J. M., Dickson, W. B., and Dickinson, M. H., 2004, "Force production and flow structure of the leading edge vortex of flapping wings at high and low Reynolds number," *J. Exp. Biol.*, **207**, pp. 1063–1072, doi: 10.1242/jeb.00848.

[15] Harbig, R., Sheridan, J., and Thompson, M., 2013, "Reynolds number and aspect ratio effects on the leading-edge vortex for rotating insect wing planforms," *J. Fluid Mech.*, **717**, pp. 166–192, doi: 10.1017/jfm.2012.565.

[16] Wang, Z. J., 2000, "Two dimensional mechanism for insect hovering," *Phys. Rev. Lett.*, **85**, pp. 2216–2219, doi: 10.1103/PhysRevLett.85.2216.

[17] Rees, C. J., 1975, "Form and function in corrugated insect wings," Nature, 256, pp. 200–203, doi: 10.1038/256200a0.

[18] Ennos, A. R., and Wootton, R. J., 1989, "Functional wing morphology and aerodynamics of Panorpa Germanica (Insecta Mecoptera)," *J. Exp. Biol.*, **143**, pp. 267–284.

[19] Wootton, R. J., 1992, "Functional morphology of insect wings," *Annu. Rev. Entomol.*, **37**, pp. 113–140, doi: 10.1146/annurev.en.37.010192.000553.

[20] Wootton, R. J., 1993, "Leading edge section and asymmetric twisting in the wings of flying butterflies (Insecta Papilionoidea)", *J. Exp. Biol.*, **40**, pp. 105–117.

[21] Combes, S. A., and Daniel, T. L., 2003, "Flexural stiffness in insect wings I. Scaling and the influence of wing venation," *J. Exp. Biol.*, **206**, pp. 2979–2987, doi: 10.1242/jeb.00523.
[22] Combes, S. A., and Daniel, T. L., 2003, "Flexural stiffness in insect wings II. Spatial distribution and dynamic bending," *J. Exp. Biol.*, **206**, pp. 2989–2997, doi: 10.1242/jeb.00524.
[23] Zhao, L., Huang, Q., Deng, X., and Sane, S. P., 2010, "Aerodynamic effects of flexibility in flapping wings," *J. R. Soc. Interface*, **7**, pp. 485–497, doi: 10.1098/rsif.2009.0200.
[24] Mountcastle, A. M., and Combes, S. A., 2013, "Wing flexibility enhances load-lifting capacity in bumblebees," *P. Roy. Soc. B-Biol. Sci.*, **280**, pp. 1–8, doi: 10.1098/rspb.2013.0531/.
[25] Kang, C. K., and Shyy, W., 2013, "Scaling law and enhancement of lift generation of an insect-size hovering flexible wing," *J. R. Soc. Interface*, **10**, pp. 1–11, doi: 10.1098/rsif.2013.0361.
[26] Xiao, Q., Hu, J., and Liu, H., 2014, "Effect of torsional stiffness and inertia on the dynamics of low aspect ratio flapping wings," *Bioinspir. Biomim.*, **9**, pp. 1–15, doi: 10.1088/1748-3182/9/1/016008.
[27] Wang, X., Li, Y., and Shi, Y., 2008, "Effects of sandwich microstructures on mechanical behaviors of dragonfly wing vein," *Compos. Sci. Technol.*, **68**, pp. 186–192, doi: 10.1016/j.compscitech.2007.05.023.
[28] Li, Y., and Wang, X., 2008, "Investigation on characteristics of structure and simulation analysis for dragonfly wing vein," *Adv. Mat. Res.*, **33**, pp. 785–788, doi: 10.4028/www.scientific.net/AMR.33-37.785.
[29] Jongerius, S., and Lentink, D., 2010, "Structural analysis of a dragonfly wing," *Exp. Mech.,* **50**, pp. 1323–1334, doi: 10.1007/s11340-010-9411-x.
[30] Sims, T., Palazotto, A., and Norris, A., 2010, "A structural dynamic analysis of a Manduca Sexta forewing," *Int. J. Micro Air Veh.*, **2**, pp. 119–140, doi: 10.1260/1756-8293.2.3.119.
[31] Ishihara, D., Horie, T., and Denda, M., 2009, "A two-dimensional computational study on the fluid-structure interaction cause of wing pitch change in Dipteran flapping flight," *J. Exp. Biol.*, **212**, pp. 1–10, doi: 10.1242/jeb.020404.
[32] Yin, B., and Luo, H., 2010, "Effect of wing inertia on hovering performance of flexible flapping wings," *Phys. Fluids*, **22**, pp. 111902-1–111902-10, doi: 10.1063/1.3499739.
[33] Young, J., Walker, S., Bomphrey, R., Taylor, G., and Thomas, A., 2009, "Details of insect wing design and deformation enhance aerodynamic function and flight efficiency," *Science*, **325**, pp. 1549–1552, doi: 10.1126/science.1175928.
[34] Dai, H., Luo, H., and Doyle, J., 2012, "Dynamic pitching of an elastic rectangular wing in hovering motion," *J. Fluid Mech.*, **693**, pp. 473–499, doi: 10.1017/jfm.2011.543.
[35] De Rosis, A., 2014, "On the dynamics of a tandem of asynchronous flapping wings: lattice Boltzmann-immersed boundary simulations," *Physica A*, **410**, pp. 276–286, doi: 10.1016/j.physa.2014.05.041.
[36] De Rosis, A., Falcucci, G., Ubertini, S., and Ubertini, F., 2014, "Aeroelastic study of flexible flapping wings by a coupled lattice Boltzmann-finite element approach with immersed boundary method," *J. Fluids Struct.*, **49**, pp. 516–533, doi: 10.1016/j.jfluidstructs.2014.05.010.

[37] Su, X., Cao, Y., Zhao, Y., 2016, "An unstructured mesh arbitrary Lagrangian-Eulerian unsteady incompressible flow solver and its applications to insect flight aerodynamics," *Phys. Fluids*, **28**, pp. 1–25, doi: 10.1063/1.4949547.
[38] Pornsin-sirirak, T. N., Tai, Y. C., Nassef, H., and Ho, C. M., 2001, "Titanium-alloy MEMS wing technology for a micro air vehicle application," *Sensor Actuat. A-Phys.*, **89**, pp. 95–103, doi: 10.1016/s0924-4247(00)00527-6.
[39] Tanaka, H., Matsumoto, K., and Shimoyama, I., 2007, "Fabrication of a three-dimensional insect-wing model by micromolding of thermosetting resin with a thin elastmeric mold," *J. Micromech. Microeng.*, **17**, pp. 2485–2490, doi: 10.1088/0960-1317/17/12/014.
[40] Tanaka, H., Matsumoto, K., and Shimoyama, I., 2008, "Design and performance of micromolded plastic butterfly wings on butterfly ornithopter," *Proceedings of the IEEE Int. Conf. Intell.*; Nice, France: September 22–26, 2008, doi: 10.1109/iros.2008.4651065.
[41] Tanaka, H., and Wood, R. J., 2010, "Fabrication of corrugated artificial insect wings using laser micromachined molds," *J. Micromech. Microeng.*, **20**, pp.1–8, doi: 10.1088/0960-1317/20/7/075008.
[42] Shang, J. K., Combes, S. A., Finio, B. M., and Wood, R. J., 2009, "Artificial insect wings of diverse morphology for flapping-wing micro air vehicles," *Bioinsp. Biomim.*, **4**, pp. 1–6, doi: 10.1088/1748-3182/4/3/036002.
[43] Harvard Microrobotics Laboratory, Cambridge, Massachusetts, USA.
[44] Xie, L., Wu, P., and Ifju, P., 2010, "Advanced flapping wing structure fabrication for biologically inspired hovering flight," *Proceedings of the 51st AIAA/ASME/ASCE/AHS/ASC Structures, Structural Dynamics, and Materials Conference*, AIAA Paper No. 2010–2789; Orlando, FL 32819, USA: April 12–15, 2010, doi: 10.2514/6.2010-2789.
[45] Bao, X., Bontemps, A., Grondel, S., and Cattan, E., 2011, "Design and fabrication of insect-inspired composite wings for MAV application using MEMS technology," *J. Micromech. Microeng.*, **21**, pp. 1–16, doi: 10.1088/0960-1317/21/12/125020.
[46] Albertani, R., Stanford, B., Hubner, J. P., and Ifju, P. G., 2007, "Aerodynamic coefficients and deformation measurements on flexible micro air vehicle wings," *Exp. Mech.*, **47**, pp. 625–635, doi: 10.1007/s11340-006-9025-5.
[47] Chakravarty, U. K., 2011, "Modal analysis of a composite wing of a micro air vehicle," *J. Aircraft*, **48**, pp. 2175–2178, doi 10.2514/1.C031488.
[48] Chakravarty, U. K., and Albertani, R., 2011, "Modal analysis of a flexible membrane wing of micro air vehicles," *J. Aircraft*, **48**, pp. 1960–1967, doi: 10.2514/1.c031393.
[49] Wu, P., Stanford, B. K., Sallstrom, E., Ukeiley, L., and Ifju, P. G., 2011, "Structural dynamics and aerodynamics measurements of biologically inspired flexible flapping wings," *Bioinsp. Biomim.*, **6**, pp. 1–20, doi: 10.1088/1748-3182/6/1/016009.
[50] Carpenter, T. J., and Albertani, R., 2015, "Aerodynamic load estimation from virtual strain sensors for a pliant membrane wing," *AIAA J.*, **53**, pp. 2069–2079, doi: 10.2514/1.j053291.
[51] Banks, J., Giovannetti, L. M., Soubeyran, X., Wright, A. M., Turnock, S. R., and Boyd, S. W., 2015, "Assessment of digital image correlation as a method of obtaining deformations of a structure under fluid load," *J. Fluid Struct.*, **58**, pp. 173–187, doi: 10.1016/j.jfluidstructs.2015.08.007.

[52] Alioli, M., Masarati, P., Morandini, M., Carpenter, T., Osterberg, N., and Albertani, R., 2017, "Membrane shape and load reconstruction from measurements using inverse finite element analysis," *AIAA J.*, **55**, pp. 297–308, doi: 10.2514/1.J055123.
[53] Coe, R., Freeman, P., and Mattingly, P., 1950, "Handbooks for the identification of British insects. Nematocera: families Tipulidae to Chironomidae (Tipulidae)," *R. Entomol Soc. Lond.*, **9**, pp. 1–66.
[54] Ellington, C. P., 1984, "The aerodynamics of hovering insect flight. II. Morphological parameters," *Philos. Trans. R. Soc. Lond. B, Biol. Sci.*, **305**, pp. 17–40, doi: 10.1098/rstb.1984.0050.
[55] Ketcham, R. A., and Carlson, W. D., 2001, "Acquisition, optimization, and interpretation of X-ray computed tomographic imagery: applications to the geosciences," *Comput. Geosci.*, **27**, pp. 381–400, doi: 10.1016/s0098-3004(00)00116-3.
[56] Microphotonics, Allentown, Pennsylvania, USA.
[57] Chapman, R. F., Simpson, S. J., and Douglas, A. E., 2013, The Insects: Structure and Function, fifth ed., Cambridge University Press, New York, New Jersey, USA.
[58] Bruker MicroCT, Kontich, Belgium.
[59] Rubio, J., Schilling, P., and Chakravarty, U. K., 2014, "A structural dynamic analysis of a crane fly forewing," *Proceedings of 55th AIAA/ASME/ASCE/AHS/SC Structures, Structural Dynamics, and Materials Conference*, AIAA Paper No. 2014–1517; National Harbor, MD 20745: January 13–17, 2014, doi: 10.2514/6.2014-1517.
[60] Dassault Systemes, Solidworks, Software Package, Version 2013, Waltham, Massachusetts, USA.
[61] Dassault Systemes, Abaqus, Software Package, Version 6.12, Providence, Rhode Island, USA.
[62] Wainwright, S., Biggs, W., Currey, J., and Gosline, J., 1986, Mechanical Design in Organisms, first ed., Princeton University Press, Princeton, New Jersey, USA.
[63] Smith, C. W., Hebert, R., Wootton, R. J., and Evans, K. E., 2000, "The hind wing of the desert locus (Schistocerca gregaria Forskal) II. Mechanical properties and functioning of the membrane," *J. Exp. Biol.*, **203**, pp. 2933–2943.
[64] Song, F., and Lee, K. L., 2004, "Experimental studies of the material properties of the forewing of cicada (Homoptera, Cicadidae)," *J. Exp. Bio.*, **207**, pp. 3035–3042, doi: 10.1242/jeb.01122.
[65] Jin, T., Goo, N. S., Woo, S., and Park, H. C., 2009, "Use of a digital image correlation technique for measuring the material properties of beetle wing," *J. Bionic Eng.*, **6**, pp. 224–231, doi: 10.1016/s1672-6529(08)60105-5.
[66] Wootton, R. J., Evans, K. E., Herbert, R., and Smith, C. W., 2000, "The hind wing of the desert locus (Schistocerca gregaria Forskal) I. Functional morphology and mode of operation," *J. Exp. Biol.*, **203**, pp. 2921–2931.
[67] Agrawal, A., and Agrawal, S., 2009, "Design of bio-inspired flexible wings for flapping-wing micro-sized air vehicle applications," *Adv. Robotics*, **23**, pp. 979–1002, doi: 10.1163/156855309X443133.
[68] Dassault Systemes, Abaqus 6.12 Analysis User Manual, Providence, Rhode Island, USA.
[69] Tannehill, J., Anderson, D., and Pletcher, R., 1997, Computational Fluid Mechanics and Heat Transfer, second ed., Taylor and Francis, Philadelphia, Pennsylvania, USA.
[70] DuPont, Wilmington, Delaware, USA.
[71] MicroChem, Westborough, Massachusetts, USA.

[72] Lorenz, H., Despont, M., Fahrni, N., LaBianca, N., Renaud, P., and Vettiger, P., 1997, "SU-8: A low-cost negative resist for MEMS," *J. Micromech. Microeng.*, **7**, pp. 121–124, doi: 10.1088/0960-1317/7/3/010.
[73] Shell Chemical Company, The Hague, Netherlands.
[74] Martinez-Duarte, R., and Madou, M., 2010, "SU-8 Photolithography and its impact on microfluidics," *Microfluidics and Nanofluidics Handbook*, **8**, pp. 231–268, doi: 10.1201/b11188-11.
[75] Madou, M., 2011, Fundamentals of Microfabrication and Nanotechnology: Volume III. Manufacturing Techniques for Microfabrication and Nanotechnology, third ed., Taylor & Francis Group, Boca Raton, Florida, USA.
[76] CAD/ART Services Inc., Bandon, Oregon, USA.
[77] Brewer Science Inc., Rolla, Missouri, USA.
[78] Newport Corporation, Irvine, California, USA.
[79] International Light Technologies, Peabody, Massachusetts, USA.
[80] Orteu, J., 2009, "3-D compute vision in experimental mechanics," *Opt. Lasers Eng.*, **47**, pp. 282–291.
[81] Sutton, M. A., Orteu, J., and Schreier, H., 2009, Image Correlation for Shape, Motion, and Deformation Measurements: Basic Concepts, Theory and Applications, first ed., Springer Science + Business Media LLC, New York, New York, USA.
[82] Correlated Solutions, Inc., 2009, Digital Image Correlation: Overview of Principles and Software [PowerPoint slides], SEM 2009 Workshop. Retrieved from www.researchgate.net
[83] Correlated Solutions, Inc., VIC 3-D V7 Testing Guide, Irmo, South Carolina, USA.
[84] Albertani, R., Stanford, B., Hubner, J. P., and Ifju, P. G., 2007, "Aerodynamic coefficients and deformation measurements on flexible micro air vehicle wings," *Exp. Mech.*, **47**, pp. 625–635, doi: 10.1007/s11340-006-9025-5.
[85] Stanford, B., Albertani, R., and Ifju, P. G., 2007, "Static finite element validation of a flexible micro air vehicle," *Exp. Mech.*, **47**, pp. 283–294, doi: 10.1007/s11340-006-9003-y.
[86] Sutton, M. A., Yan, J., Deng, X., Cheng, C., and Zavattieri, P., 2007, "Three-dimensional digital image correlation to quantify deformation and crack-opening displacement in ductile aluminum under mixed-mode I/III loading," *Opt. Eng.*, **46**, pp. 1–17 , doi: 10.1117/1.2741279.
[87] Lecompte, D., Vantomme, J., and Sol, H., 2006 "Crack detection in a concrete beam using two different camera techniques," *Struct. Health Monit.*, **5**, pp. 59–68, doi:10.1177/1475921706057982.
[88] Florando, J. N., LeBlanc, M. M., and Lassila, D. H., 2007, "Multiple slip in copper single crystals deformed in compression under uniaxial stress," *Scripta Mater.*, **57** , pp. 537–540, doi: 10.1016/j.scriptamat.2007.05.014
[89] Florando, J. N., Rhee, M., Arsenlis, A., LeBlanc, M. M., and Lassila, D. H., 2006, "Calculation of the slip system activity in deformed zinc single crystals using digital 3-D image correlation data," *Phil. Mag. Lett.*, **86**, pp. 795–805, doi: 10.1080/09500830601047695.
[90] Sutton, M. A., Ke, X., Lessner, S. M., Goldbach, M., Yost, M., Zhao, F., and Schreier, H., 2008, "Strain field measurements on mouse carotid arteries using microscopic three

dimensional digital image correlation," *J. Biomed. Mater. Res. A.*, **84**, pp. 178–190, doi: 10.1002/jbm.a.31268.
[91] Moser, R., and Lightner III, J. G., 2007, "Using three-dimensional digital imaging correlation techniques to validate tire finite-element model," *Exp. Techniques*, **31**, pp. 29–36, doi: 10.1111/j.1747-1567.2007.00157.x.
[92] Owolabi, G. M., and Singh. M. N. K., 2007, Erratum to "A comparison between two analytical models that approximate notch-root elastic-plastic strain-stress components in two-phase, particle-reinforced, metal matrix composites under multiaxial cyclic loading: Experiments [Int. J. Fatigue 28 (2009) 918-925]," *Int. J., Fatigue*, **29**, pp. 792, doi:10.1016/j.ijfatigue.2006.07.001.
[93] Bracewell, R. N., 1986, The Fourier Transform and Its Applications, first ed., McGraw-Hill Education, New York, New York, USA.
[94] Leissa, A., 1973, "The free vibration of rectangular plates," *J. Sound Vib.*, **31**, pp. 257–293, doi: 10.1016/s0022-460x(73)80371-2.
[95] Data Physics Corporation, San Jose, California, USA.
[96] Dytran Instruments INC., Chatsworth, California, USA.
[97] Photron, San Diego, California, USA.
[98] Correlated Solutions, Inc., Irmo, South Carolina, USA.
[99] Correlated Solutions, Inc., VIC-Snap, Software Package, Version 7.8, Irmo, South Carolina, USA.
[100] Correlated Solutions, Inc., VIC-3D, Software Package, Version 7.2.4, Irmo, South Carolina, USA.
[101] TSI Inc., Shoreview, Minnesota, USA.
[102] Aerolab LLC, Jessup, Maryland, USA.
[103] White, F., 1991, Viscous Fluid Flow, second ed., McGraw-Hill Education, New York, New York, USA.
[104] 3M Company, Maplewood, Minnessota, USA.
[105] Avery Dennison, Glendale, California, USA.
[106] Gutierrez, J., Meneses, M., and Chavez, C., 2003, "Mathieu Functions, A Visual Approach," *Am. J. Phys.*, **71**, pp. 233–242, doi: 10.1119/1.1522698.
[107] Schneider Kreuznach, Rhineland-Palatinate, Germany.
[108] Glück, M., Breuer, M., Durst, F., Halfmann, A., and Rank, E., 2001, "Computation of fluid-structure interaction on lightweight structures," *J. Wind Eng. Ind. Aerod.*, **89**, pp. 1351–1368, doi: 10.1016/s0167-6105(01)00150-7.
[109] Mengesha, T. E., Vallance, R. R., Barraja, M., and Mittal, M., 2009, "Parametric structural modeling of insect wings," *Bioinspir. Biomi.*, **4**, pp. 1–15, doi: 10.1088/1748–3182/4/3/036004.
[110] Mountcastle, A., and Daniel, T., 2009, "Aerodynamic and functional consequences of wing compliance," *Exp. Fluids*, **46**, pp. 873–882, doi: doi: 10.1007/s00348-008-0607-0
[111] Nakata, T., and Liu, H., 2012, "Aerodynamic performance of a hovering hawkmoth with flexible wings: a computational approach," *Proc. R. Soc. B.*, **279**, pp. 722–731, doi: 10.1098/rspb.2011.1023.

APPENDICES

Appendix I—Mesh Independence Study for the FE Model of the Artificial Wing

The different mesh grids considered for the mesh independence study of the FE model of the artificial wing are presented in Table A.1. The mesh grid highlighted in yellow and presented in bold font was used for the calculations of the natural frequencies of the FE model of the artificial wing as described in Section 4.4.4. The results of this mesh grid were compared with those from the other mesh grids that were tested.

Table A.1 Mesh independence study for the FE model of the artificial wing

Global size (mm)	FE model membrane			FE model veins			FE model total		Natural frequency (Hz)			% Diff		
	Size (mm)	No. of nodes	No. of elements	Size (mm)	No. of nodes	No. of elements	No. of nodes	No. of elements	1st	2nd	3rd	1st	2nd	3rd
0.1	1.50	431	382	2.00	316	163	747	545	161.68	642.47	1016.17	13%	14%	16%
0.1	1.00	664	604	1.50	352	181	1016	785	156.37	613.10	992.47	10%	9%	14%
0.1	0.50	1333	1246	1.00	442	226	1775	1472	145.19	585.56	900.14	2%	5%	4%
0.1	0.25	2630	2509	0.50	594	302	3224	2811	142.75	567.24	872.52	1%	2%	1%
0.1	0.20	3401	3266	0.35	732	371	4133	3637	142.92	566.11	868.86	1%	1%	1%
0.1	**0.10**	**8622**	**8424**	**0.30**	**806**	**408**	**9428**	**8832**	**141.74**	**558.70**	**861.74**	**0%**	**0%**	**0%**
0.1	0.08	12171	11938	0.75	854	432	13025	12370	141.62	557.79	860.37	0%	0%	0%
0.1	0.07	14437	14182	0.25	934	472	15371	14654	141.47	557.29	859.71	0%	0%	0%

Appendix II—Mesh Independence Study for the FSI Model of the Artificial Wing

The different mesh grids considered for the mesh independence study of the FSI model of the artificial wing are presented in Table A.2. The mesh grid highlighted in yellow and presented in bold font was used for the calculations of the deformations and the aerodynamic coefficients of the artificial wing from the FSI simulations as described in Section 4.4.5. The results of this mesh grid were compared with those from the other mesh grids that were tested.

Table A.2 Mesh independence for the FSI model of the artificial wing

CFD model global size (mm)	CFD model No. of Layers	CFD model FSI edge local number of elements	CFD model No. of nodes	CFD model No. of elements	Coefficient of drag	% Diff	Coefficient of lift	% Diff	Deformation node A (mm)	% Diff
2	50 (Bias 30)	200	1138423	1116200	3.63	1%	1.17	5%	6.774E-06	4%
2	**45 (Bias 30)**	**200**	**1025943**	**1004580**	**3.59**	**0%**	**1.11**	**0%**	**6.523E-06**	**0%**
2	30 (Bias 30)	200	688503	669720	3.54	1%	1.12	2%	6.612E-06	1%
2	20 (Bias 30)	200	463543	446480	3.51	2%	1.17	5%	6.757E-06	4%
2	10 (Bias 30)	200	238583	223240	3.36	7%	1.17	5%	6.765E-06	4%
2	10 (Bias 0)	80	110537	103080	2.38	40%	1.15	4%	5.180E-06	23%
2	No layer	No local seed	74090	68684	2.41	39%	1.11	1%	5.072E-06	25%

VITA

José Enrique Rubio Reyes was born in Tegucigalpa, Honduras. Mr. Rubio Reyes completed his B.Sc. in Mechanical Engineering in December 2012, his M.Sc. in Mechanical Engineering in December 2014, and his Ph.D. in Engineering and Applied Sciences in December 2017, all of them at the University of New Orleans. Mr. Rubio Reyes conducts research in the areas of structural dynamics, fluid-structure interaction, and design of biologically inspired structures.